Measurement of the W Boson Production Charge Asymmetry in $\mathrm{p\bar{p}}$ Collisions

by

Bo-Young Han

Submitted in Partial Fulfillment

of the

Requirements for the Degree

Doctor of Philosophy

Supervised by

Professor Kevin McFarland

Department of Physics and Astronomy

The College

Arts and Sciences

University of Rochester

Rochester, New York

2008

Curriculum Vitae

The author was born in Seoul, Republic of Korea in September 1972. He graduated from Korea University at Seoul, Republic of Korea, with a Bachelor of Science in 1999 and with a Master of Science degree in 2001. He came to the University of Rochester in the summer of 2002 to continue his studies in the field of elementary particle physics. He joined the CDF experiment at Fermi National Accelerator Laboratory, where he first worked on the development and validation of filtering code for Level3 Trigger group. He was awarded a Master of Arts degree from the University of Rochester in 2004 and conducted the research for his Ph.D. thesis on the W boson production charge asymmetry under the supervision of Prof. Kevin McFarland.

Acknowledgments

I would like to thank my family first. Father and mother, you have provided me with all of the love, support, and encouragement and always trust me without any reasons and the elder sister and brother-in-law always helped me to acclimate myself to a new environment. the second oldest sister, she has done a lot of things I should have done for my parents. Frankly, I owe you more than I can repay. Thank you, and I love you.

I thank my advisor Kevin McFarland for his support, teaching, and his insightful questioning of all my steps during the completion of this analysis. Most of all, his enthusiasm for high energy physics and philosophy for education make a deep impression on my mind. He helped me mature not only as a scientist but also as human being.

I would also like to thank my advisor Eva Halkiadakis for all of the help on this analysis and on CDF life. I was always allowed to discuss about this analysis and she encouraged me whenever I faced with some difficulties.

To KwangZoo Chung, who was always willing to devote his time to listen to my questions and frustrations of analyzing this data when I needed to talk. Thank you for being a friend through all of our long hours together.

Many more have worked directly in helping me untangle technical issues and shared part of the work load this research demanded. I especially wish to thank members of the ElectroWeak Group with whom I collaborated closely to produce this result, and YeonSei Chung, Veronique Boisvert, Jedong Lee, my colleagues from the University of Rochester.

Of course, friends played an essential role in assuring the success of this enterprise. I thank all my good an old playmates, SungHwan Suk, EunSang Park, HeungJun Park, SungJu Lee, HoHeyoung Lee, JuYoung Choi and their family members who shared either at long distance the good, bad and beautiful moments of these past years. Without

their supports I believe the last page of this analysis could not be shown.

Bo-Young

Abstract

We present a measurement of the W boson production charge asymmetry using the $W \to e\nu$ decay channel. We use data collected the Collider Detector at Fermilab (CDF) from $p\bar{p}$ collisions at $\sqrt{s}$ = 1.96 TeV. The data were collected up to February 2006 (Run II) and represent an integrated luminosity of 1 fb^{-1}. The experimental measurement of W production charge asymmetry is compared to higher order QCD predictions generated using MRST2006 and CTEQ6 parton distribution functions (PDF). The asymmetry provides new input on the momentum fraction dependence of the u and d quark parton distribution functions (PDF) within the proton over the fraction of proton's momentum range from $0.002 < x < 0.8$ corresponding to $-3.0 < y_W < 3.0$ at $Q^2 \approx M_W^2$.

Contents

List of Figures

List of Tables

Chapter 1

Introduction

In 1911, Ernest Rutherford and his associates bombarded thin gold foils with α-particles and found that some of them were deflected by huge angles, indicating the presence of a small yet massive kernel inside the atom. He thus suggested that the hydrogen nucleus was an elementary particle. The nucleus of the lightest atom (hydrogen) was given the name $proton$ (Greek $\pi\rho\dot{\omega}\tau o\nu$ = first) by Rutherford. In 1914, Niels Bohr proposed a model for hydrogen consisting of a single electron circling the proton held in orbit by the mutual attraction of opposite charges. In 1932 Chadwick found the $neutron$, which is an electrically neutral twin to the proton. Physicists realized that every element in the periodic table could be constructed of a single atomic nucleus with a distinct number of protons and neutrons, surrounded by a cloud of electrons.

The notion that protons and neutrons are fundamental particles was shattered in the late 1950's and 1960's by a population explosion of newly observed particles. With the construction of large particle accelerators, experiments produced hundreds of "elementary" particles, called $hadrons$, with properties very similar to the nucleons. In 1963, Murray Gell-Mann [1] and George Zweig independently proposed a scheme in which hadrons are composed of smaller particles, dubbed $quarks$. The quarks interact with

each other via the $strong\ force$. Some hadrons, like the proton(uud) and neutron(udd), consist of three quarks. These are the $baryons$. Others, called $mesons$, are comprised of quark-antiquark pairs. Experimental evidence for the proton's substructure was eventually established in 1968 by a team at the Stanford Linear Accelerator Center (SLAC) [2]. In an experiment not so different from Rutherford's, a high energy beam of electrons was aimed at a small vat of liquid hydrogen. The resulting scattering pattern revealed that the proton was actually a composite system. The mediators of the strong force, called $gluons$, were proposed as elementary particles that cause quarks to interact, and are transmitted between quarks to bind them into composite particles known collectively as $hadrons$. The first direct experimental evidence of gluons was found in 1979 when "three-jet" events were observed at the Positron-Electron Tandem Ring Accelerator (PETRA) at DESY in Hamburg [3]. The interactions between quarks and gluons are explained by Quantum Chromodynamics (QCD).

1.1 Quantum Chromodynamics (QCD)

Quantum chromodynamics, a part of the Standard Model of particle physics, is a non-Abelian gauge theory based on a local (gauge) symmetry group called SU(3). All the particles in this theory interact with each other through the strong force. The strength of the interaction is parametrized by the "strong coupling constant". This strength is, as usual, modified by the gauge "color charge" of the particle*. Quarks and gluons are the only fundamental particles which carry non-vanishing color charge, and hence participate in strong interactions. The color charge of a quark has three possible values: red, blue, or green. Antiquarks carry anticolor which has the opposite color charge of quarks so that for example, a red quark and an anti-red anti-quark together carry no net

*This really refers to a group theoretical property whose meaning has nothing to do with color.

color charge. The gluons are postulated to belong to an octet (8) representation of SU(3) which means, in effect, that a gluon carries both a color and an anti-color charge. One combination of color and anti-color, known as the color singlet, does not contribute to strong interactions since it does not carry a net color and is unable to mediate forces between color charges.

In QCD, since the gluon is a massless boson, a good model for the QCD potential is

$$V_{QCD} = -\frac{4}{3}\frac{\alpha_s}{r} + kr, \tag{1.1}$$

where the separation between the two color charged particles is given by r and where α_s is the strong coupling constant. At small r (≤ 0.1 fm), the interaction is assumed to be of the Coulomb type, in analogy with electromagnetism (QED), while at lager r (≥ 0.1 fm), the potential must increase indefinitely, so as to confine the quarks inside a hadron. When two quarks become separated by a large enough distance, it is energetically more favorable that a quark-antiquark pair be produced from the vacuum than to maintain the strong interaction field between them. These newly produced quarks will then form colorless hadrons with the original quark pair. This quark confinement offers an explanation of why no free quarks or gluons have ever been observed in nature.

The internal structure of the proton, e.g., its quarks and gluons, must be considered to be able to theoretically calculate the cross section of all physical processes involving the proton. The quarks and gluons inside a proton are referred to as partons, and the parton distribution function (PDF) for the proton is discussed in the next section.

1.2 Parton Distribution Functions (PDF)

Experimentally, high energy electrons serve as a natural probe of the proton's internal structure, since they interact with quarks via the electromagnetic force. In electron-

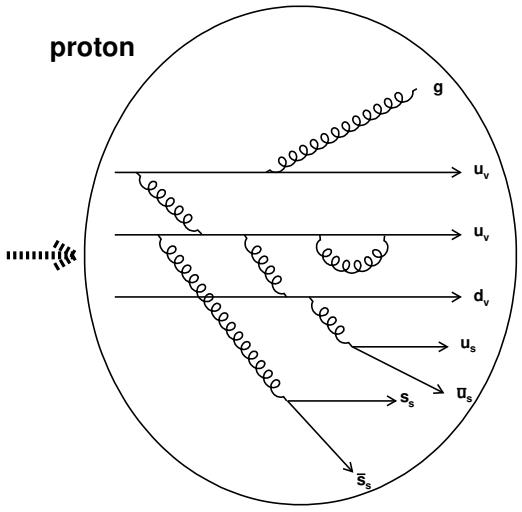

Figure 1.1: A model of a proton made up of valence quarks, gluons, and quark-antiquark pairs.

proton collisions, approximately half of the proton's momentum is carried by quarks, while the other half consists of electrically-neutral objects, such as gluons, that do not interact with electrons. This discovery led to a more complete picture of the proton's substructure and the fact that various types of partons made up the proton.

The partons can each carry a different fraction x of the parent proton's momentum and energy. The partons are often categorized as the valence quarks, gluons and sea quarks. The valence quarks are the bound-state quarks that define the quantum numbers of the proton, while sea quarks are virtual quark-antiquark pairs produced from the splitting of a gluon. As shown in Figure 1.1, the proton is described as three-valence quarks $u_v u_v d_v$ accompanied by many quark-antiquark pairs $u_s\bar{u}_s$, $d_s\bar{d}_s$, $s_s\bar{s}_s$, and so on.

In the parton model, the structure of the proton is specified by a set of "parton distribution functions" (PDFs) that give the probability for a particular parton to carry a

fraction x of the proton's total momentum. By summing over all contributing partons, the quantum numbers of the proton must be recovered.

$$\begin{aligned} \int_0^1 [u_v(x) + u_s(x) - \bar{u}_s(x)]dx &= 2 \\ \int_0^1 [d_v(x) + d_s(x) - \bar{d}_s(x)]dx &= 1 \\ \int_0^1 [s_s(x) - \bar{s}_s(x)]dx &= 0 \end{aligned} \tag{1.2}$$

where the subscripts v and s denote valence and sea quarks, respectively. The momentum density functions, given by $xu(x)$, $xd(x)$, and $xs(x)$, can be integrated over the possible values of x to find the overall fraction of the proton momentum carried by each of the quark flavors. Experimental measurements find that the fraction of the proton's momentum of the valence and sea quarks is about 45%. This implies that the remaining fraction of the momentum is carried by gluons. The structure of the proton is dependent on the energy regime (Q) of the probe. In the low energy regime ($Q < 1\mathrm{GeV}$), the proton interacts predominantly as a single particle. At medium energy ($1 < Q < 100\mathrm{GeV}$), the composite nature of the proton is apparent, and the valence quarks make the largest contribution to the interaction probed. At higher energy, the probability distribution function is dominated by gluons and sea quarks. The electroweak interactions measured in this thesis require a significant momentum be carried by each of the interaction partons in order to create the massive W boson ($\approx 80\ \mathrm{GeV/c^2}$) and therefore will usually involve at least one valence quarks. The proton PDF is shown in Figure 1.2.

PDFs have been extracted from the measurements of the structure function for deep-inelastic scattering data collected in lepton-proton collisions, and the measurement of the asymmetry in Drell-Yan production in hadron-hadron collisions. Since any particular experiment covers a limited range of x and Q^2, fixed by the center of mass energy, measurements from a variety of experiments are combined into "global QCD analyses"

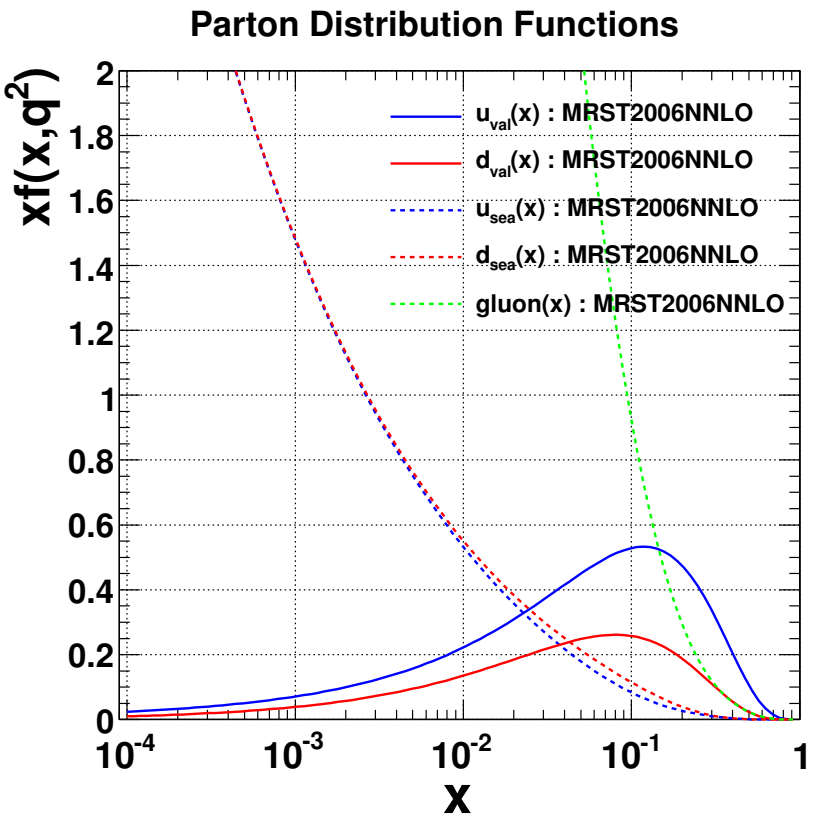

Figure 1.2: The parton distribution for the proton [5]. The contribution from valence and sea quarks are shown along with the gluon contribution. For x values above $\approx$ 0.15, valence quarks dominate the distribution and are the largest contribution to hard interactions involving the proton.

that attempt to extract the distributions for all partons in a particular hadron simultaneously. In this thesis, experimental measurements are compared to recent parton distribution functions from both of CTEQ [4] and MRST [5] which perform global fits to world data.

1.3 W Events at Tevatron

W bosons in $p\bar{p}$ colliders are produced by hard scatters between the quarks which are inside the protons and anti-protons. Protons and anti-protons are bound states of constituent partons, which are quarks and gluons as discussed in previous section. A schematic diagram of the W production process is shown in Figure 1.3. In the diagram, the constituent partons of the protons and anti-protons are shown as the horizontal lines, and the ovals that surround the lines represent protons and anti-protons. A hard scatter between a quark from proton and a anti-quark from the anti-proton is shown. These two quarks form a W, and the W is shown subsequently decaying into a lepton and a neutrino. The other partons in the proton and anti-proton are specters to the event, and they form the "underlying event." In our experiment, the protons and anti-protons travel in opposite directions, although this is not indicated in the diagram.

The inclusive rapidity distribution for production of a W^+ boson in $p\bar{p}$ collisions is expressed as

$$\begin{aligned}\frac{d\sigma}{dy_W}(W^+) &= K(y_W)\frac{2\pi G_F}{3\sqrt{2}}x_p x_{\bar{p}}\ \{\ cos^2\theta_c(u(x_p)\bar{d}(x_{\bar{p}}) + \bar{d}(x_p)u(x_{\bar{p}})) \\ &\quad + sin^2\theta_c(u(x_p)\bar{s}(x_{\bar{p}}) + \bar{s}(x_p)u(x_{\bar{p}}))\ \}, \qquad (1.3)\end{aligned}$$

where y_W is the rapidity of the W, $y_W = ln\frac{E+P_z}{E-P_z}$, θ_c is the Cabibbo mixing angle, G_F is the weak coupling constant, and the partons from the proton(anti-proton) carry momentum fraction $x_p(x_{\bar{p}})$. In Eq. 1.3 the $u(x)$, $d(x)$ and $s(x)$ PDF's are all evaluated

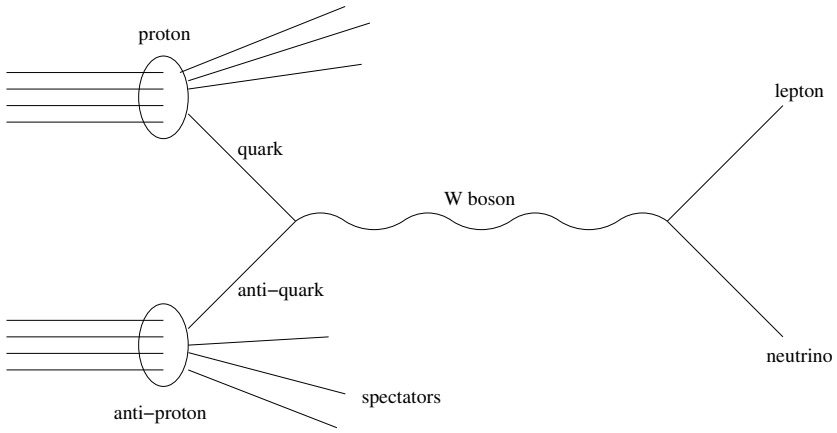

Figure 1.3: Schematic diagram of W production at $p\bar{p}$ collisions.

at $Q^2 = M_W^2$, where M_W is the W boson mass, and the factor $K(y_W)$ contains higher-order QCD radiative corrections which are discussed in Section 5.2. Furthermore, we can derive the x value related to the rapidity of the W boson from momentum and energy conservation in Eq. 1.4. The relationship is shown in Figure 1.4.

$$x_p = \frac{M_W}{\sqrt{s}} e^{y_W}, \quad x_{\bar{p}} = \frac{M_W}{\sqrt{s}} e^{-y_W}, \tag{1.4}$$

In a $p\bar{p}$ collider, W bosons are reconstructed primarily from $W \rightarrow \mu\nu$ or $e\nu$ leptonic decays. This is done because $W \rightarrow q\bar{q}$ hadronic decay is usually buried inside a large QCD background ($p\bar{p} \rightarrow jets$), as are the τ's from the $W \rightarrow \tau\nu$ process. In approximately 10% of the W events, the W decays into an electron[†] and a neutrino. These are the events which we use in this thesis to measure the W production charge asymmetry. The neutrino passes through the detector without interacting. The electron, on the other hand, leaves a track in the tracking chamber, and also deposits its energy in

[†]we will often use the word electron to refer generically to both the electron and its anti-particle, the positron.

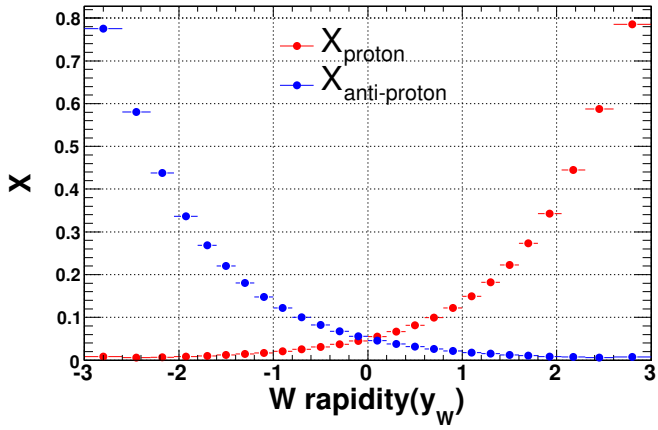

Figure 1.4: The x values of quark production W boson at the Tevatron.

the calorimeters that surround the interaction region.

The leading order W boson production mechanism results in the W boson being polarized in the $\bar{p}$ direction by means of the $V-A$ structure of the weak interaction as shown in Figure 1.5.

The $V-A$ structure means that the weak current couples only to left-handed u and d quarks (or to right-handed $\bar{u}$ and $\bar{d}$ quarks). For ultra-relativistic quarks, where helicity, which is the projection of the spin onto the direction of momentum, and chirality (handedness) are approximately equivalent, this results in full polarization of the produced W bosons in the direction of the beam. The W leptonic decay process also couples only to left-handed e^- and right-handed $\bar{\nu}$ (or right-handed e^+ and left-handed ν). The conservation of angular momentum favors a decay with the final state lepton (neutrino or electron) at a small angle with respect to the initial state quark direction (and a similar small angle between the initial state anti-quark and final anti-lepton). The systematic shift in lepton pseudo-rapidity with respect to y_W depending on the charge of the final state lepton is illustrated in Fig. 1.6, which shows the lepton pseudo-rapidity vs. W

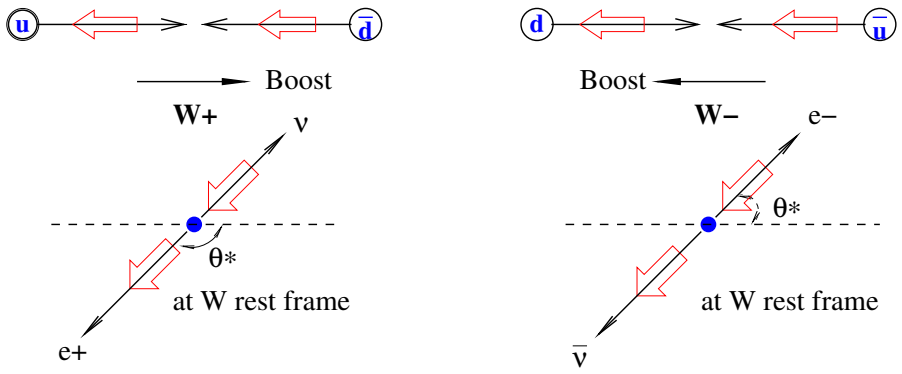

Figure 1.5: The momenta and helicities in $p\bar{p} \rightarrow W^{\pm}$ production and $W^{\pm}$ leptonic decay.

rapidity for the different charges.

1.4 W Charge Asymmetries

$W^+(W^-)$ bosons are produced in $p\bar{p}$ collisions primarily by the annihilation of $u(d)$ quarks in the proton and $\bar{d}(\bar{u})$ quarks in the anti-proton. Since $u(x_p) = \bar{u}(x_{\bar{p}})$ and $d(x_p) = \bar{d}(x_{\bar{p}})$ by CPT symmetry, the differential cross sections for $W^{\pm}$ are approximately

$$\frac{d\sigma^+}{dy_W} \approx \frac{2\pi}{3}\frac{G_F}{\sqrt{2}}\left[u(x_p)\bar{d}(x_{\bar{p}})\right], \tag{1.5}$$

$$\frac{d\sigma^-}{dy_W} \approx \frac{2\pi}{3}\frac{G_F}{\sqrt{2}}\left[d(x_p)\bar{u}(x_{\bar{p}})\right]. \tag{1.6}$$

Since the u quark tends to carry a larger fraction of the proton's momentum than the d quark on average, the $W^+(W^-)$ is boosted in the proton (anti-proton) direction as shown in Fig. 1.7(a). The W production charge asymmetry, $A(y_W)$, in the leading-order

parton model is therefore

$$\begin{aligned} A(y_W) &= \frac{d\sigma^+/dy_W - d\sigma^-/dy_W}{d\sigma^+/dy_W + d\sigma^-/dy_W} \\ &\approx \frac{u(x_p)\bar{d}(x_{\bar{p}}) - d(x_p)\bar{u}(x_{\bar{p}})}{u(x_p)\bar{d}(x_{\bar{p}}) + d(x_p)\bar{u}(x_{\bar{p}})} \\ &= \frac{R_{du}(x_{\bar{p}}) - R_{du}(x_p)}{R_{du}(x_{\bar{p}}) + R_{du}(x_p)}, \end{aligned} \tag{1.7}$$

where we use Eq. 1.5 and Eq. 1.6 and introduce the ratio $R_{du} = \frac{d(x)}{u(x)}$. As we see in Eq. 1.7, there is a direct correlation between the W production charge asymmetry and the d/u ratio. A precise measurement of the W production charge asymmetry therefore serves as a constraint on the u and d quark momentum distributions [6].

Since the W leptonic decay involves a neutrino whose longitudinal momentum is experimentally undetermined, the charge asymmetry previously has reported as a measured charge asymmetry of the decay leptons as a function of the lepton pseudo-rapidity. The lepton charge asymmetry is defined as:

$$A(y_l) = \frac{d\sigma^+/dy_l - d\sigma^-/dy_l}{d\sigma^+/dy_l + d\sigma^-/dy_l}, \tag{1.8}$$

Previous measurements [7, 8, 9] are described in the end of this section.

However, as shown in Fig. 1.7(b), there is a "turn-over" in the lepton charge asymmetry due to a convolution of the W production charge asymmetry and the W $V-A$ decay. This "turn-over" depends on the lepton kinematics, while the W production charge asymmetry is free from this effect. This convolution means leptons from a single pseudo-rapidity come from a range of W rapidity and thus a range of parton x values. Thus, the measured lepton asymmetry is more complicated to interpret in terms of quark distributions, and we expect the direct measurement of the asymmetry of the $W^{\pm}$ rapidity distribution to be a more sensitive probe of the ratio of $d(x)$ and $u(x)$.

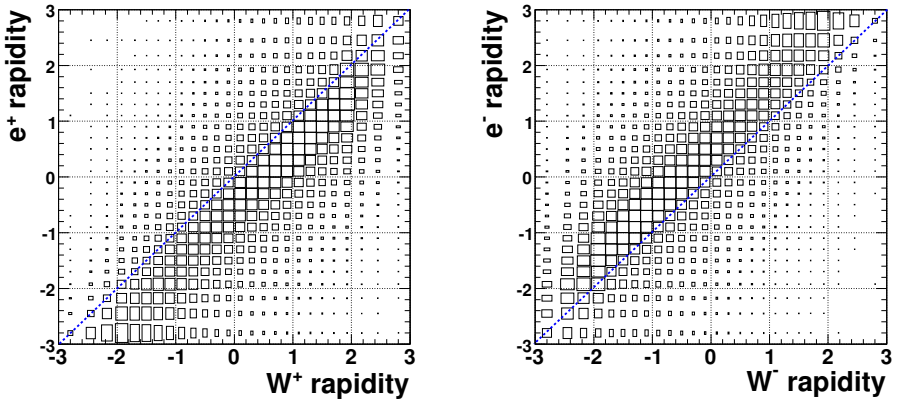

(a) (b)

Figure 1.6: (a) The positively charged W boson and lepton rapidity distribution. (b) The negatively charged W boson and lepton rapidity distribution.

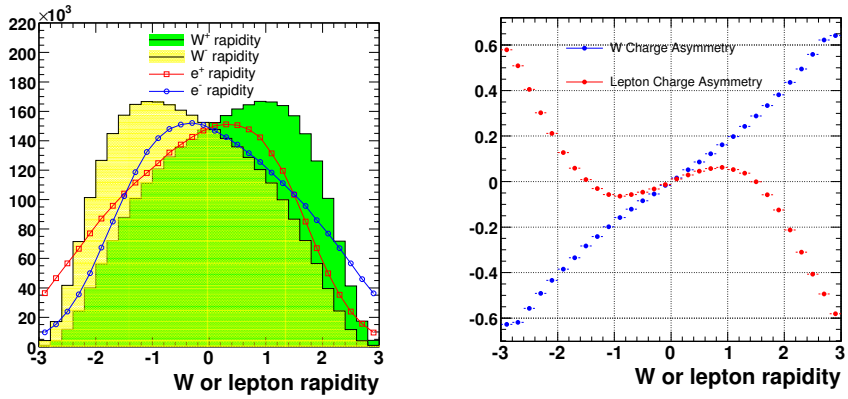

(a) (b)

Figure 1.7: (a) The W boson and lepton rapidity distributions in $p\bar{p}$ collisions. (b) The charge asymmetry for W production and the decay lepton.

Measurement of the $d(x)/u(x)$ ratio

Experimental information on $d(x)/u(x)$ has usually come from measurements of the F_2^n/F_2^p structure function ratio, with the neutron structure function F_2^n extracted from F_2^p and the deuteron F_2^D structure functions [10, 11, 12], and the deuterium data are sensitive to nuclear corrections. Consequently, the determination of the $d(x)$ valence quark distribution depends on the modeling of nuclear effects in the deuteron [13, 14]. Previous constraints on the $d(x)/u(x)$ ratio also come from the lepton charge asymmetry in W boson decays in $p\bar{p}$ collisions mentioned above. The W charge asymmetry data in $p\bar{p}$ collisions has an advantage over the determination from proton and deutron structure functions as it is and is free from the kind of uncertainties in nuclear effects that affect the DIS data. The results at Tevatron are shown in Figure 1.8(a) [7], Figure 1.8(b) [8], and Figure 1.8(c) [9].

1.5 Thesis Outline

The Tevatron accelerator complex and the detectors used to collect the collision data are described in Chapter 2. In Chapter 3 the datasets used in the analyses presented here, and the trigger and reconstruction requirements to identify the electron and to select our $W \to e\nu$ events are shown. Chapter 4 discusses the measurement of backgrounds. Our analysis technique for the W production charge asymmetry is introduced in Chapter 5. The corrections required to remove any bias are described in Chapter 6. Finally, the measurement of W production charge asymmetry and the uncertainties of this measurement are presented and discussed in Chapter 7.

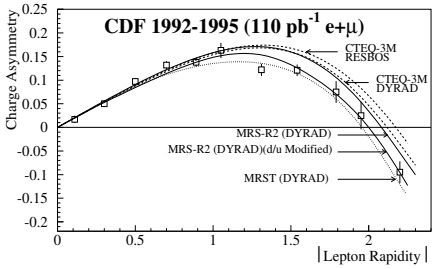

(a) CDF Run I data (110 pb^{-1})

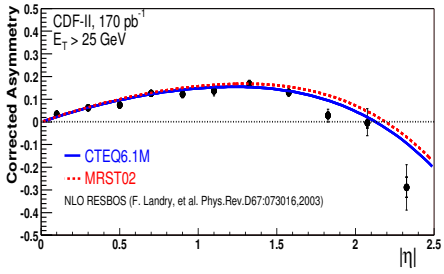

(b) CDF Run II data (170 pb^{-1})

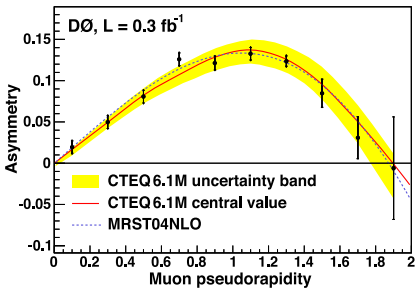

(c) DØ Run II data (300 pb^{-1})

Figure 1.8: The charge asymmetry for W decay lepton in $p\bar{p}$ collisions.

Chapter 2

Experimental Apparatus

The experimental apparatus is located at the Fermi National Accelerator Laboratory (Fermilab) in Batavia, Illinois. The detector used in this analysis is the Collider Detector at Fermilab (CDF), a multi-purpose experiment that records proton-antiproton collisions in the Tevatron accelerator. In this chapter I describe the accelerator and CDF detector, with an emphasis on the components which are used in the W charge asymmetry measurement with electrons. The trigger systems are discussed in Section 2.3

2.1 The Fermilab Tevatron

The accelerator complex [15] is shown schematically in Figure 2.1. We can use this diagram to follow the protons and antiprotons from their production to their final collision in the center of the CDF detector.

The Pre-Accelerator, Linac and Booster

Everything starts at a Cockroft-Walton pre-accelerator that generates H^- ions with 750 keV of kinetic energy. These ions are fed into the linear accelerator (Linac) in bunches

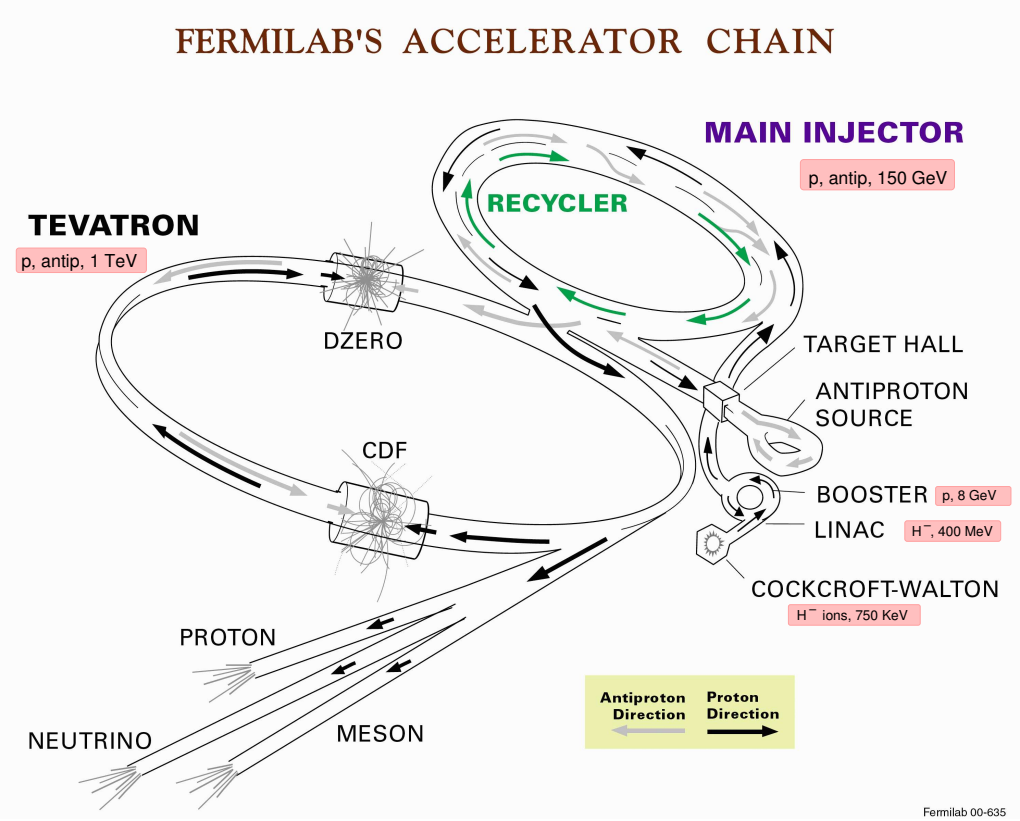

Figure 2.1: The Fermilab accelerator complex.

at a rate of 201.24 MHz.

The Linac accelerates the H^- ions to 400 MeV using the electric field in radio frequency cavities that extend for 150 m. These bunches of accelerated H^- ions are then injected into the Booster.

The Booster is a circular synchrotron 151 m in diameter. At injection, the H^- ions are stripped of their electrons by passing them through a thin carbon foil. The remaining protons are then accelerated to 8 GeV by multiple passes around the ring through electromagnetic fields in cavities and passed to the Main Injector.

The Main Injector is also a circular synchrotron with a diameter of 1 km, where protons from the Booster are accelerated from 8 GeV to 150 GeV. Antiprotons, produced by 120 GeV protons at the Antiproton Source (see below) are focused, re-tuned and accelerated from 8 GeV to 150 GeV in the Main Injector. (The Main Injector also provides the 120 GeV protons to the Antiproton Source, which is used to produce and collect 8 GeV antiprotons.)

The Antiproton Source

The 120 GeV protons from the Main Injector impact a nickel target at the Antiproton Source. The produced particles include antiprotons, with an efficiency of one antiproton of 8 GeV per $\approx$ 50,000 incident protons (after focusing and filtering). To provide good bunches for collisions in the Tevatron, the antiproton beam has to be reduced in its transverse-momentum phase space in a process called stochastic “cooling”. After this, bunches of well focused antiprotons are transfered to the Main Injector to be accelerated to 150 GeV.

Tevatron

The Tevatron is the final stage of acceleration. This synchrotron accelerator ring has a diameter of ≈2 km, and uses superconducting magnets of up to ≈4 Tesla to bend and contain the beam. The 150 GeV protons and antiprotons are accelerated to 980 GeV in opposite directions, leading to 1.96 TeV collision energy in the center of mass. A total of 36 bunches of protons and 36 bunches of antiprotons share the same pipe and travel in opposite directions. Each proton bunch carries roughly 3×10^{11} protons, and the antiproton bunches carry $\approx 3 \times 10^{10}$ antiprotons. These bunches collide at two points of the ring (DØ and CDF) with a design frequency of one bunch crossing at the interaction regions every 396 ns.

2.2 The Collider Detector at Fermilab (CDF)

The Collider Detector at Fermilab (CDF II) is a general purpose detector designed to study the physics of $p\bar{p}$ collisions at the Tevatron accelerator at Fermilab. Like most detectors used in high energy collider experiments it has a cylindrical geometry with axial and forward-backward symmetry. The innermost part of the detector contains an integrated tracking system with a silicon detector, and an open cell drift chamber in a 1.4 T solenoidal magnetic field. The integrated tracking system is surrounded by calorimeters. Outside of the calorimeters is a muon system. A more detailed elevation view labeling the different components is shown in Figure 2.2.

2.2.1 CDF Coordinate System

CDF uses a spherical system of coordinates, with the $z-$axis oriented along the beam direction, where positive z is defined as the direction in which the protons are traveling. The origin is at the center of the detector. The polar angle θ is the angle measured from

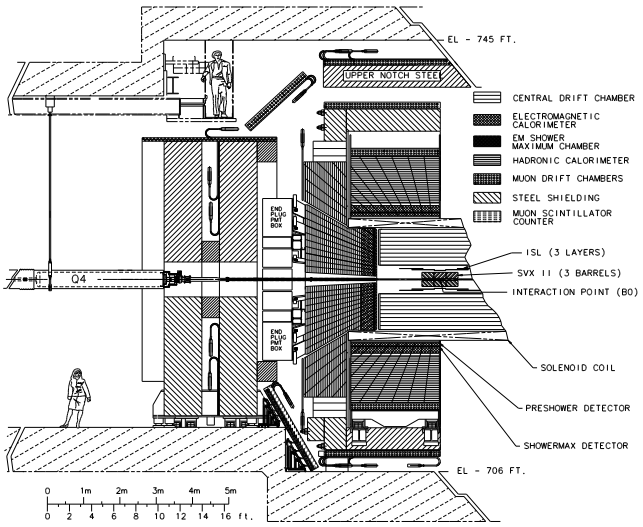

Figure 2.2: An elevation view of the CDF Run II detector.

the positive $z-$axis. The angle ϕ is the angle measured from the vector lying in the plane of the accelerator pointing away from the center (shown in Figure 2.3). Since in hadron colliders the center of mass frame of the interacting partons may be boosted along the z axis, it is useful to define quantities that are perpendicular to the z axis. The transverse (or $r-\phi$) plane is defined as the plane perpendicular to the z axis. Transverse quantities (such as E_T, p_T, etc) are the projections of those quantities onto the transverse plane.

The pseudorapidity η, indicated in Figure 2.4 is defined as

$$\eta = -\ln\tan\frac{\theta}{2}, \tag{2.1}$$

where the pseudorapidity is an approximation to rapidity $y = \frac{1}{2}\ln\left(\frac{E+p_z}{E-p_z}\right)$, and corresponds to y when particle masses can be neglected. Two forms of pseudorapidity are used in this analysis. The detector pseudorapidity, η_d, measures the pseudorapidity from the nominal interaction point at the center of the detector. It is frequently used to spec-

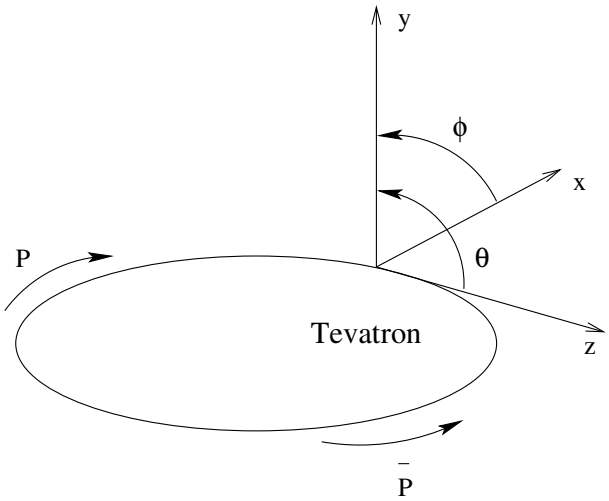

Figure 2.3: The coordinate system used by the CDF experiment.

ify the physical segmentation of the detector. The event pseudorapidity, η, measures the pseudorapidity of particles from a $p\bar{p}$ interaction with respect to the interaction vertex. Because the interaction region at CDF is long along the z direction, approximately 120cm, there is often a significant difference between the two quantities.

2.2.2 Luminosity Monitoring

The instantaneous luminosity, $\mathcal{L}$, is defined by

$$\mathcal{L} = f \frac{n_p n_{\bar{p}}}{4\pi\sigma_p\sigma_{\bar{p}}} \,. \tag{2.2}$$

where f is the frequency of crossing for bunches containing n_p protons and $n_{\bar{p}}$ antiprotons, and the Gaussian transverse beam profiles are given by σ_p and $\sigma_{\bar{p}}$. The conventional unit for luminosity is $cm^{-2}s^{-1}$.

However, at the Tevatron the factors in Eq. 2.2 cannot be measured with sufficient

precision to predict the collision luminosity. Since measuring the integrated luminosity is necessary to predict event yields and monitoring the instantaneous luminosity critical to detector operation, a custom detector must be used to determine the luminosity from the production of particles in the collisions themselves. For Run II, CDF uses a Cherenkov Luminosity Counter (CLC) to measure the instantaneous luminosity [16]. The CLC has two modules, each located in the small 3° conical hole in the high η region of the forward calorimeter. The luminosity monitor is constructed of an array of segmented counters, with each counter being 2 m long and several cm in diameter. The counters are constructed of aluminized mylar and filled with isobutane gas. A fast PhotoMultiplier Tube (PMT) at the end of each counter collects the Cherenkov light from charged particles radiating in the gas, and gives a timing resolution of better than 100 ps. This resolution is needed for coincidence measurement between the two CLC modules. The projective design of the counters means that they have reduced sensitivity to secondary particles produced in the detector or from beam pipe interactions. The CLC is also not sensitive to beam halo particles since they hit the CLC from behind generating Cherenkov light going away from the PMTs. Measuring the number of hits in the CLC allows calculation of the instantaneous $\mathcal{L}$ as defined by Eqn. 2.3.

$$\mathcal{L} = \frac{f_{BC} < N_H >_\alpha}{\sigma_{in}\epsilon_\alpha < N_H^1 >_\alpha} \,. \tag{2.3}$$

Here f_{BC} is the bunch crossing frequency, and σ_{in} the inelastic $p\bar{p}$ cross section. Given selection criteria denoted by α, ϵ_α is the CLC efficiency; $< N_H >_\alpha$ is the number of hits in the CLC for the bunch crossing, and $< N_H^1 >_\alpha$ is the number of hits in the CLC for a single $p\bar{p}$ collision. The measured error on the acceptance of the CLC is 4% , and in combination with the uncertainty on the measured inelastic $p\bar{p}$ cross section of 4%, gives an integrated luminosity error of 6% for Run II data collection [16].

2.2.3 Tracker

The ”integrated tracking system” at CDF, shown in Figure 2.4, involves a new open cell drift chamber, the Central Outer Tracker (COT), and the ”silicon inner tracker” system, which consists of 3 independent structures: the Layer00 detector (L00), the Silicon Vertex Detector (SVX), and the Intermediate Silicon Layer (ISL). Both the SVX and ISL employ double sided silicon, where one side makes measurements in the transverse plane, and the other side is used to make measurements in the z direction.

Silicon detectors(SVX, L00, ISL)

The silicon inner tracker consists of three concentric silicon detectors located at the very center of CDF [17]. The innermost one, L00, is a single-sided, radiation-hard silicon layer attached to the outside of the beam pipe at a diameter of 2.2 cm and a detailed view of the L00 mounting is shown in Figure 2.5. This provides complete ϕ coverage, and z coverage extending $\pm$ 78.4 mm from $z = 0$.

The Silicon Vertex Detector (SVX) consists of 5 layers of silicon with an inner radius of 2.4 cm and outer radius of 10.7 cm. It is composed of three barrels, each 29 cm long, as shown in Figure 2.5; all together they extend about 45 cm in the z direction on each side of the interaction point covering 2.5σ of the luminous region. Each barrel is divided in 12 wedges in ϕ , where each wedge supports the five layers double-sided silicon micro-strip detectors. The double sided design provides information about $r - \phi$ and z position while occupying the small footprint of a single sensor. The stereo side of layers 0,1, and 3 are perpendicular to the z axis, while the stereo angle of layers 2, and 4 are -1.2° and $+1.2^\circ$ respectively. Using the z position information, a 3D helix for each track can be reconstructed.

The Intermediate Silicon Layer (ISL) consists of three silicon layers placed at radii of 20, 22 and 28 cm, respectively, from the beam axis. The layer at 22 cm covers the central

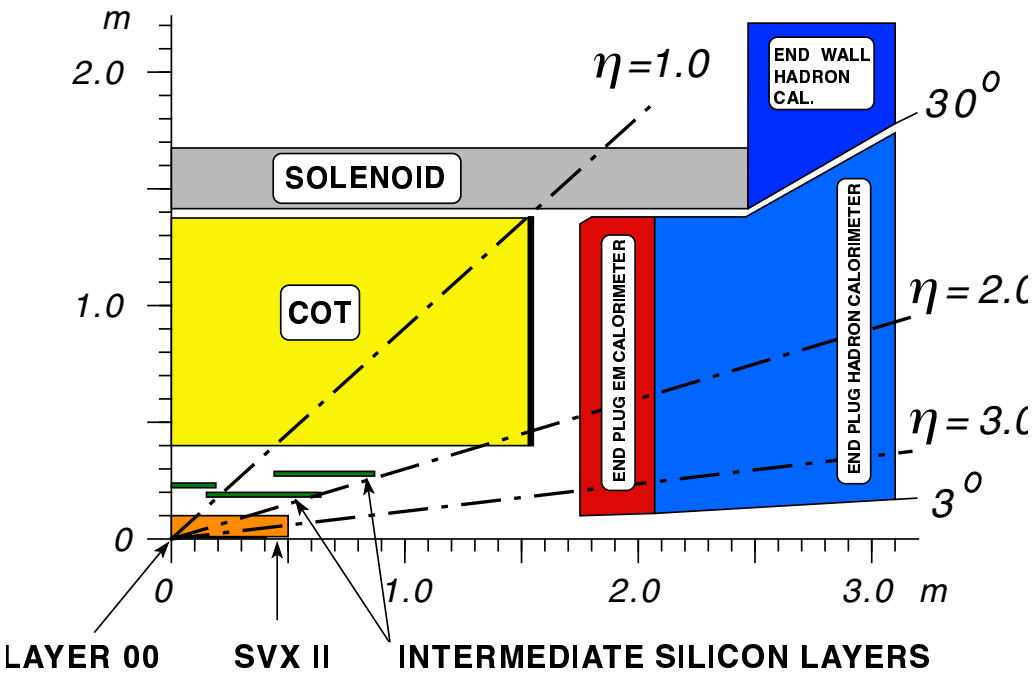

Figure 2.4: Longitudinal View of the CDF II Tracking System.

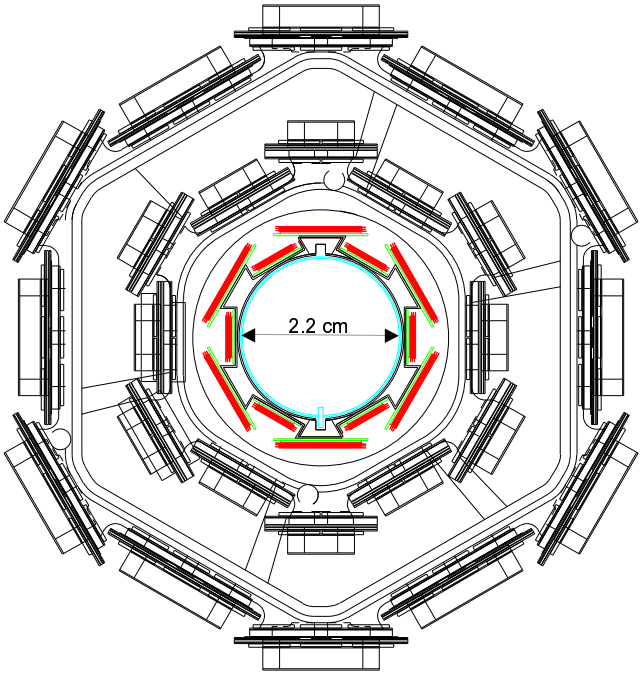

Figure 2.5: Detail of the Layer 00 Silicon along with the two innermost layers of the SVX Silicon.

region $|\eta| < 1$, while the two outer layers cover the forward region corresponding to $1 < |\eta| < 2$, where the coverage from the COT falls off. The "inner silicon tracker" when combined with the COT is designed to greatly improve the impact parameter resolution and also improve the momentum resolution. The side view shown in Figure 2.6 is a cross-section of one half of the silicon tracker, using a compressed z scale to illustrate coverage in η.

Central Outer Tracker

Tracking in the central region is provided by the Central Outer Tracker, an open cell drift chamber which consists of eight superlayers (Figure 2.7) of cells placed between the radii of 40 and 132 cm from the beam pipe [18]. The tracking volume is divided into 8 super layers (SL), 4 axial layers (for $r - \phi$ measurement) and 4 stereo layers (for z measurement) with the structure shown in Figure 2.7. The superlayers alternate between stereo and axial, with the innermost superlayer being stereo. The design of three cells from SL2 can be seen in Figure 2.7. Ar-Ethane gas (60:40 mixture) fills the active chamber volume and both provides a source of ionized electrons and defines the drift velocity of the gas. The COT (beam constrained) tracking momentum resolution, $\sigma(p_T)$ $\approx 0.15\% p_T^2 [\mathrm{GeV/c}]^{-1}$. The tracking system is a crucial element in the identification of the electrons in the central region, as electron candidates are formed by energy clusters in the electromagnetic calorimeter which match a track in the COT. The electron identification algorithms use the curvature information and the direction of the track.

2.2.4 Calorimeters

Surrounding the tracking volume and solenoid, the CDF calorimeter modules measure not only the energy of particles but also a coarse position. All of the calorimeters in CDF are based upon sandwiching scintillating material between layers of heavy material. As

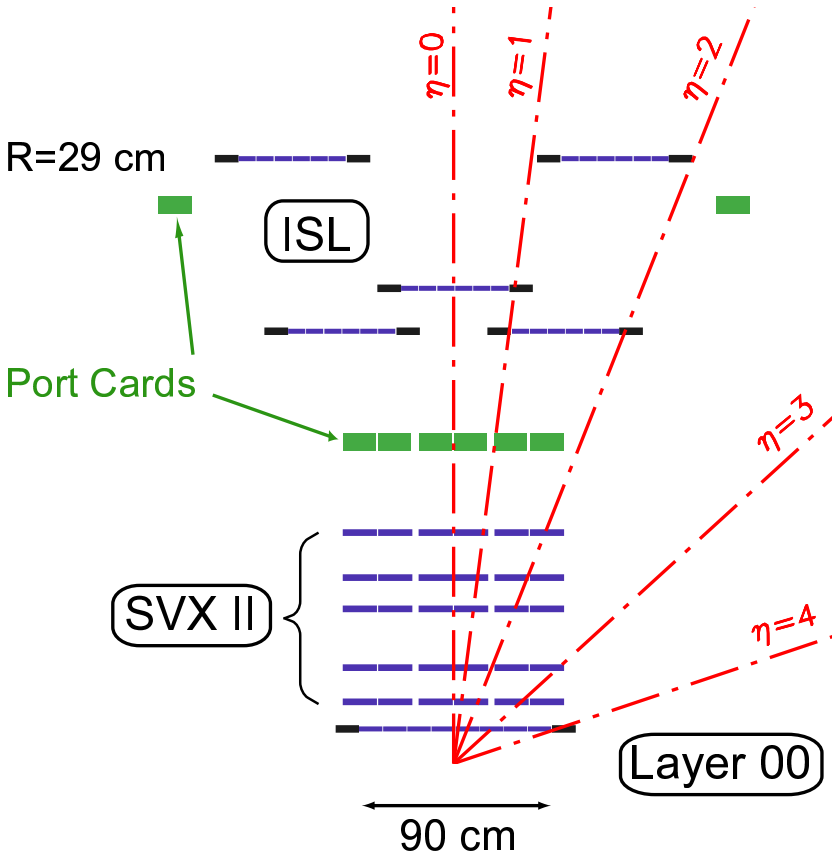

Figure 2.6: A side view of half of the CDF Run II silicon system.

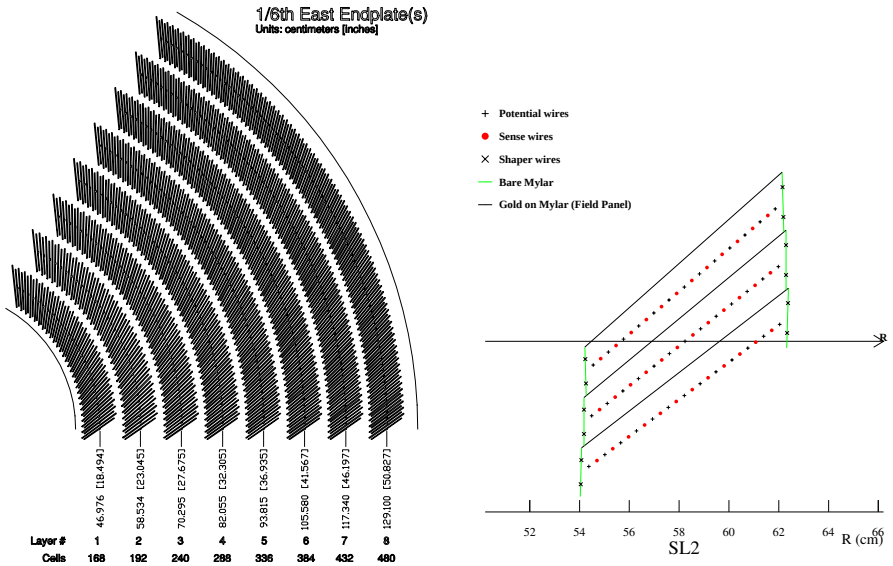

Figure 2.7: On the left, the endplate slots are shown; in this figure the odd layers are stereo and the even layers are axial superlayers, according to the definition in the text. On the right, a single cell layout is shown.

Sub Detector	CEM	CHA	WHA	PEM	PHA
Coverage	$\|\eta\| < 1.1$	$\|\eta\| < 0.9$	$0.7 < \|\eta\| < 1.3$	$1.1 < \|\eta\| < 3.6$	$1.1 < \|\eta\| < 3.6$
Modules	48	48	48	24	24
Layers	31	32	15	23	23
Absorber material	Lead	Steel	Steel	Lead	Iron
Depth	$18\chi_0$	$4.7\lambda_0$	$4.5\lambda_0$	$21\chi_0$	$7\lambda_0$
Energy Resolution	$1.7\% + \frac{13.5\%}{\sqrt{E}}$	$\frac{80\%}{\sqrt{E}}$	$\frac{80\%}{\sqrt{E}}$	$1\% + \frac{16\%}{\sqrt{E}}$	$5\% + \frac{80\%}{\sqrt{E}}$

Table 2.1: Summary of the CDF calorimeters.

charged particles progress through the calorimeters they interact and develop characteristic 'showers'. Whereas electrons and photons shower quickly and are largely contained in the electromagnetic calorimeter, hadron jets pass through and leave significant energy in the hadronic calorimeters. Specific showering materials allow sensitivity to either electromagnetic (high Z material) or hadronic (high A material) particles. In the CDF detector, the electromagnetic calorimeters are immediately followed by hadronic calorimeters. The calorimeter is divided into a central calorimeter covering $|\eta| < 1.1$, and a forward calorimeter providing coverage out to $|\eta| < 3.6$. A summary of the sub systems is given in Table 2.1.

Central Electromagnetic Calorimeter (CEM, CES, CPR)

The central electromagnetic calorimeter (CEM) is constructed in 15° wedges placed outside the solenoid and consists of 31 layers of polystyrene scintillator interleaved with layers of lead clad in aluminum. The sheets are stacked in a projective tower geometry, as shown in Figure 2.8(a), where each tower subtends 15° in ϕ and 0.1 in η. It can be seen that in each wedge 'tower 9' is truncated; this will be important later in defining electron fiduciality. At higher z some of the lead is replaced by plastic in order that the effective radiation depth be approximately independent of angle. Light is fed through

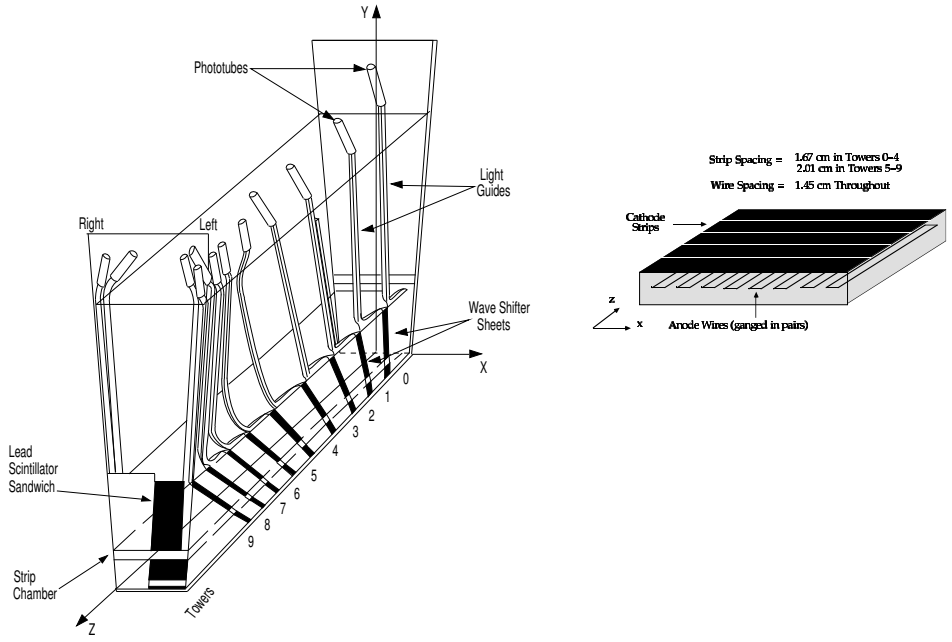

(a) CEM (b) CES

Figure 2.8: (a) A wedge of the central calorimeter, showing the projective tower geometry. (b) A central shower-max chamber shown schematically.

waveshifters and collected in phototubes as indicated in Figure 2.8(a). After the eighth layer of lead, corresponding to the depth at which showers typically reach their maximum transverse extent, is the central shower-maximum (CES) detector. This consists of proportional chambers as shown in Figure 2.8(b) that give good position resolution. A component of the central calorimeters is the central pre-radiator (CPR), a set of proportional chambers between the CEM and the magnet designed to help separate electrons and pions by identifying energy at the very start of the shower.

Central and Wall Hadronic Calorimeters (CHA, WHA)

The central hadronic calorimeter (CHA) surrounds the CEM and consists of steel layers sampled each 2.5 cm by scintillator. Filling a space between the CHA and the forward plug hadronic calorimeter (PHA) is the wall hadronic calorimeter (WHA), which continues the tower structure of the CHA but with reduced sampling each 5.0 cm. Like the electromagnetic calorimeters, the hadronic calorimeters are read out using waveshifting lightguides and phototubes.

Plug Electromagnetic Calorimeter (PEM, PES, PPR)

The plug electromagnetic calorimeter (PEM) was newly built for CDF Run II. Like the CEM, the PEM consists of a stack of lead and scintillator sheets read out by phototubes. At lower values of η the tower segmentation is 7.5° in ϕ, doubling to 15° at higher η as shown in Figure 2.9, which also gives the η segmentation. A 30 GeV electron shower will be largely contained in four of the towers at lower η. Approximately 6 radiation lengths into the PEM is a shower-maximum detector, the PES , designed to provide good position measurement. It consists of two layers of scintillator strips at 45° to each other, assembled in 45° sectors.

Finally, the first layer of the PEM is read out separately and referred to as the plug pre-radiator (PPR). The PPR can help to distinguish between electrons/photons and hadrons by indicating the extent to which the particle shower has already developed at the face of the calorimeter.

Plug Hadronic Calorimeter (PHA)

The plug hadronic calorimeter (PHA) consists of layers of iron and scintillator, extending back from and maintaining the same segmentation as in the PEM.

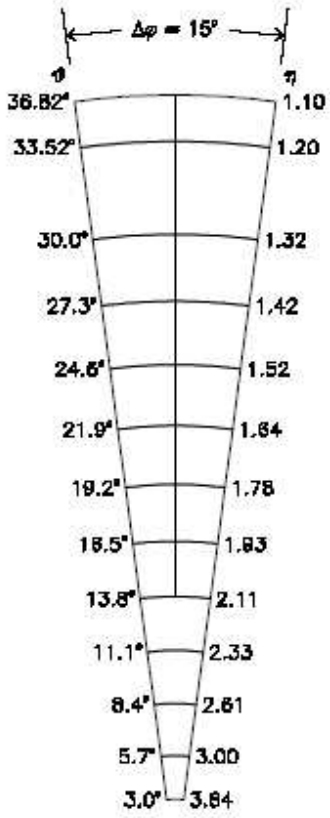

Figure 2.9: Forward detector segmentation.

2.2.5 Muon System

Outside of all other sub detectors is the CDF muon system. A high p_T muon will generally leave a track in the tracking volume but very little energy deposition in the calorimeter due to the $\frac{1}{M^2}$ suppression of EM Bremsstrahlung [19]. In order to distinguish muon tracks from electrons and pions that escaped the detector through cracks in the calorimeter, drift chambers and scintillators are constructed behind the calorimeter. Short track segments are reconstructed from the hits in these detectors and then matched to tracks in the tracking chamber. The muon systems are not used in these analyses.

2.3 Data Acquisition and Trigger Systems

CDF has a trigger system to select scientifically interesting events from all of the events that take place during $p\bar{p}$ collisions and to not exceed the current data acquisitions limitations. The CDF trigger system consists of three levels. Each level is successively more sophisticated and takes a longer time to reach a decision. If all three trigger levels are passed, the event is written out to tape. Each of the levels consists of a logical OR of a number of triggers which are designed to find many types of events. The trigger allows for the event storage rate to be reduced from the bunch crossing rate of 2.5 MHz, to a rate within the limits of the DAQ system, 100 Hz. The stucture of the trigger is shown in Figure 2.10 and the details of each level of the trigger will be discussed next.

Level 1

The goal of the Level-1 (L1) trigger is to process information on every beam crossing (2.5 MHz), and reduce the rate to less than 30 kHz. There are three parallel processing streams finding calorimeter objects, muons and tracks respectively, which may be combined with AND and OR to give 64 triggers. At L1, calorimeter objects consist of single

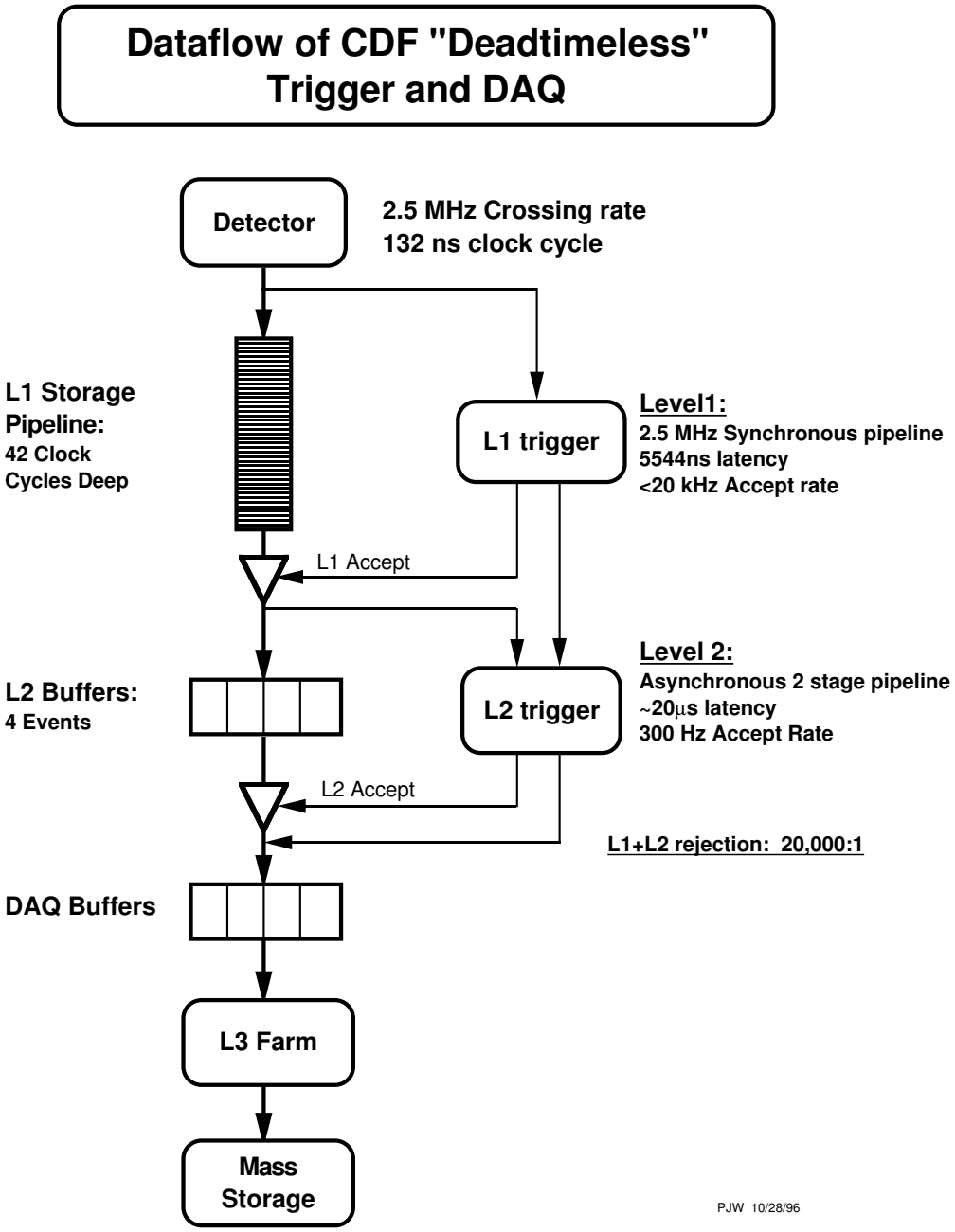

Figure 2.10: The three level deadtime-less trigger used to control the DAQ of the CDF detector.

tower energies, tracks are 2-dimentional as found by the eXtremely Fast Tracker (XFT) which compares COT hits to look-up tables; and muons consist of a 'stub' in the muon chambers matched to a track within 2.5° in ϕ.

Level 2

The goal of the Level-2 (L2) trigger is to reduce the rate from L1 ($< 30\mathrm{kHz}$) to 300 Hz. Events accepted by L1 are processed by the second level of trigger, which is composed by several asynchronous subsystems. L2 collects the information available at L1 and does some further reconstruction. It identifies displaced vertices seeded by the L1 tracks, collects nearby towers with energy depositions into calorimeter clusters, and measures the amount of energy deposited in the CES detector in each wedge. All of this information is sent to the programmable L2 processors in the Global Level-2 crate, which evaluate if any of the L2 triggers are satisfied.

Level 3

The Level-3 (L3) trigger consists of two components, the event builder and the L3 processing farm. The event builder consists of custom built hardware used to assemble and package all of the information from a single event. The L3 farm runs a version of the full offline reconstruction code. This means that for example fully reconstructed 3-dimentional tracks are available to the trigger decision. The L3 output rate is $\sim 75\mathrm{Hz}$ and accepted events are written to tape in eight separate 'streams', sorted by trigger, by the Consumer-Server Logger (CSL).

All events passing a L3 trigger are collected from the detector and processed with the CDF Offline reconstruction. The details of the analysis and selection of $W \rightarrow e\nu$ events are described in the Chapter 3.

Chapter 3

Data Reduction and Signal Extraction

This analysis focuses on the electron decay of the W, and uses a high transverse momentum (p_T) electron trigger that selects events containing electron candidates. W candidate events are selected from reconstructed events with one high p_T electron in the central or forward calorimeters and an imbalance of calorimeter energy due to the undetected neutrino. In this chapter, the details of the trigger, event reconstruction and the event selection are discussed and the requirements of the $W \rightarrow e\nu$ sample and the $Z \rightarrow e^+e^-$ sample are presented.

3.1 Data Samples

3.1.1 CDF data

Three data samples are employed in this analysis. These are obtained from the *inclusive high-p_T electron* data sample.

- **The $W \rightarrow e\nu$ sample** : Two samples of $W \rightarrow e\nu$ candidates, where electrons are in the central or forward region, are used to measure W charge asymmetry and to study the boson recoil energy scale.

- **The $Z \rightarrow e^+e^-$ sample** : A sample of dielectron candidates is used to calibrate the energy scale and resolution of the EM calorimeter, to study the efficiency of electron identification, and to check charge biases in measuring electrons

- **The dijet sample** : A sample of dijet events (events with at least one jet with $E_T > 15\text{GeV}$) is used to measure the rate at which a jet fakes an electron signature and to estimate the dijet background.

3.1.2 Monte Calro generation and simulation

The Monte Carlo (MC) generation and simulation are used to estimate the acceptance for the $W \rightarrow e\nu$ process, to determine the characteristics and amount of background in the data sample, and to understand the systematic uncertainties on the W charge asymmetry. PYTHIA [20] generator with the CTEQ5L PDFs [21] is used for all samples. PYTHIA generates processes at the leading order (LO) and incorporates initial and final state QCD and QED radiation via shower alogrithms. The sample is tuned so that the underlying event and p_T spectrum of Z bosons agree with the CDF data [23]. The detector simulation models the decay of generated particles and their interactions with the various elements of the CDF detector. The calorimeter energy scale and resolution in the simulation are tuned so that the mass distribution of the $Z \rightarrow e^+e^-$ event in the simulation match with those from the data (see Section 6.1). These are three Monte Carlo samples used in this analysis, which are briefly described below.

- **The $W \rightarrow e\nu$ sample** : A sample of 20 M events generated with PYTHIA is used to calculate the correction due to acceptance and recoil energy scale and to estimate the systematic uncertainties on the W charge asymmetry.

- **The $Z \rightarrow e^+e^-$ sample** : A sample of 10 M events generated with PYTHIA is used to calculate the corrections due to electron energy scale and resolution,

electron identification, and charge mis-identification.

- **The $W \rightarrow \tau\nu$ ($\tau \rightarrow e\nu$) sample** : A sample of 16 M events generated with PYTHIA is used to calculate the correction due to acceptance. The $W \rightarrow e\nu$ signature can be reproduced by $W \rightarrow \tau\nu$ events in which the τ lepton subsequently decays into an electron. This sample is part of the signal itself, since it has the same underlying charge asymmetry, and it is inclued when calculating in the signal acceptance.

For each sample, we use two different simulated samples, GEN5 and GEN6, according to CDF software offline version. GEN5 MC corresponds to the collected data up to February 2004 and GEN6 MC corresponds to the data from December 2004 to February 2006.

3.2 Trigger

The $W \rightarrow e\nu$ event is based upon the high energy electron or positron. The identification of electrons begins with the online trigger system, which selects events with electron characteristics. The charged lepton produces a signal in both the calorimeter and the tracker that can be matched in coincidence. For electrons in the central calorimeter, events are selected using only this single object selection. For W decays with electrons in the forward calorimeter, the tracking coverage dose not allow for coincidence between the calorimeter and tracking information. To overcome this, a trigger decision based on both the electron calorimeter information and missing transverse energy is used to select events. Using these two triggers, the data events were selected for analysis as W candidates. The detailed requirements of each trigger path are described in the next sections.

3.2.1 Central Electron Trigger : ELECTRON_CENTRAL_18 path

The central electron trigger selects electron candidates with a high-E_T electron in the central region ($|\eta| < 1.1$). In order to have calculable trigger efficiencies, for an event to be considered at L2, it must have passed the prerequisite L1 trigger, Similarly at L3, the event must have passed the prerequisite L2 trigger. The trigger efficiency is then the simple product of the individual trigger efficiencies. The following paragraphs describe the selection requirements at each of the three trigger levels.

- **Level 1 : L1_CEM8_PT8** This requires a central electromagnetic (EM) cluster with $E_T^{EM} > 8\mathrm{GeV}$ and $E^{HAD}/E^{EM} < 0.125$ for clusters with energy less than 14 GeV. An XFT track with $p_T > 8\mathrm{GeV/c}$ must be matched to the trigger tower containing the EM cluster.

- **Level 2 : L2_CEM16_PT8** This requires a central EM cluster with $E_T^{EM} > 16\mathrm{GeV}$ and the ratio $E^{HAD}/E^{EM} < 0.125$ for all clusters. An XFT track with $p_T > 8\mathrm{GeV/c}$ must be matched to the L2 cluster.

- **Level 3 : L3_CENTRAL_ELETRON_18** This requires a central EM cluster with $E_T^{EM} > 18\mathrm{GeV}$ and $E^{HAD}/E^{EM} < 0.125$. A fully reconstructed 3D track with $p_T > 9\mathrm{GeV/c}$ must be matched to the seed tower of the EM cluster.

When the trigger requirements of all three levels are combined, the efficiency for identifying a reconstructable central electron with $E_T > 25\mathrm{GeV}$ from $W \rightarrow e\nu$ decay is $\sim 98\%$. A detailed description of the trigger efficiencies is supplied in Appendix A.1.

3.2.2 Plug Electron Trigger : MET_PEM path

The plug electron trigger selects events with both a high-E_T electron candidate and missing transverse energy, $\not\!\!E_T$. The three trigger levels are described in the following paragraphs.

- **Level 1 : L1_EM8_MET15** This requires an EM cluster with $E_T^{EM} > 8$ GeV and $E^{HAD}/E^{EM} < 0.125$ for clusters with energy less than 14 GeV. The $\not\!\!E_T$ must be greater than 15 GeV with the z coordinate of the interaction assumed to be zero.

- **Level 2 : L2_PEM20_MET15** This requires an plug EM (PEM) cluster with $E_T^{EM} > 20$ GeV and the ratio $E^{HAD}/E^{EM} < 0.125$ for all clusters. There is an implicit cut on the $\not\!\!E_T$ since only events passing the L1_EM8_MET15 trigger are considered for L2.

- **Level 3 : L3_PEM20_MET15** This requires an plug EM (PEM) cluster with $E_T^{EM} > 20$ GeV and $E^{HAD}/E^{EM} < 0.125$. The $\not\!\!E_T$, which is offline $\not\!\!E_T$ calculated at $z = 0$, must be greater than 15 GeV.

The efficiency for identifying a reconstructable plug electron with $E_T > 25$ GeV and $\not\!\!E_T > 25$ GeV from $W \rightarrow e\nu$ decay is $\sim 96\%$. A detailed description of the trigger efficiencies is also supplied in Appendix A.2.

3.3 Electrons

The tracking and calorimetry of the CDF detector allow us to identify electrons and measure their energies with high precision. Using information from several detector subsystems, the trajectories of electrons from $p\bar{p}$ collisions can be traced from the interaction region, through the tracking subsystems, and into the electromagnetic calorimeters.

3.3.1 Calorimeter Clustering

Using the objects selected by the high-p_T central and forward trigger, the offline selection of electron candidates begins with the formation of EM clusters in the calorimeters. The initial step in the clustering is to apply tower-to-tower calibrations and to sort the

towers by E_T considering only towers with greater than 100 MeV of energy. At this stage the event vertex is assumed to be located at $z = 0$ for all transverse calculations. Starting with the highest E_T tower, a tower is considered for addition to the cluster. The neighboring towers are now considered for addition to the cluster. Since the geometry of the detectors is different, the clustering strategy varies between the two detectors and the candidate neighboring towers are different in the CEM and PEM.

In the CEM, only towers that neighbor the seed tower in η are considered for the cluster. Therefore a CEM cluster will be completely contained within a single wedge. If the neighbor tower has an E_T greater than 100 MeV it is added to the cluster. After considering all neighbor towers, a CEM cluster will have 1, 2, or 3 towers contained in the cluster.

In the PEM, all towers sharing a border or corner with the seed tower are considered as neighbor towers. There are then 8 possible neighboring towers that can be added to the seed tower. These 8 towers are sorted by EM E_T. If it has an E_T greater than 100 MeV, the highest E_T tower is selected as the seed tower's daughter. The clustering now searches for a pair of towers to combine with the seed and daughter towers to make a 2 $\times$ 2 tower cluster. It considers all 2 $\times$ 2 combinations, and selects the one with highest E_T. If the additional pair of towers has an E_T greater than 100 MeV, then the towers are added to the cluster. This alorithm most commonly produces 4 towers clusters in a 2 $\times$ 2 configuration.

3.3.2 Track Reconstruction

Tracks are a key component in the identification of particles. Having efficient and precise reconstruction is crucial for this analysis. Two tracking algorithms are used to identify charged particles traversing the detector in the offline reconstruction. For particles that cross the COT in $|\eta_d| < 1.6$, a hit-based tracking reconstruction is used. But for

particles that enter the forward calorimeter outside of $|\eta_d| = 1.6$, a silicon standalone (SISA) tracking in the only SVX detector is used because of the COT range. The details of the two alogrithms are discussed below.

COT tracking

The central track reconstruction algorithm uses several difference strategies to form 3-dimensional charged-particle tracks [24]. The resulting 3D tracks have a transverse momentum resolution of $\sigma(p_T)$ = 0.15%$p_T^2[\mathrm{GeV/c}]^{-1}$. The reconstruction begins with individual hits of the COT channels. After timing calibration, the initial segment-finding algorithm groups hits in the axial super layers (SLs) into segments based upon both the hit location within the cell and the timing of the hits. During the initial segment-building processing, hits in a SL may be shared by two different segments. But after the processing is finished within the SL, only the segment with the greater total hits retains the shared hit. After completing the construction of the axial segments, a histogramming algorithm is run to create additional segments that the initial segment finder may have missed. The second set of segments is then merged together into the initial segment link. Once segments have been formed in all of the axial SLs, these segments are linked together to form 2D tracks in the $r - \phi$ plane. The segment finding algorithm is then repeated in the stereo layers. These additional segments are now considered for addition to the 2D tracks in order to provide z information. If a 2D track does not have any stereo hits after the stereo segment linking, the individual hits in the stereo layers are considered for addition to the track. If enough stereo hits are successfully matched to the track, the hits are retained for track z information. After the addition of the stereo segments, the tracks now have full p_T and 3D orientation information. The efficiency of the COT tracking reconstruction was measured using central electron W events triggered without any track requirement. It was found to be 99.3% [25] for these high-p_T isolated tracks.

SISA tracking

The standard SVX II tracking at CDF starts with a COT track and searches for SVX II hits by extrapolating the COT track into the SVX II geometrical region. However, The silicon stardalone tracking (SISA) in forward region is a track finding procedure for electrons (or positrons) using only SVX II hits. The SISA tracker starts by collecting $r\phi$ hit combinations from 5 axial layers [26]. Track candidates with 4 or 5 hits are fitted with a curve to obtain the axial track parameters. Once an $r\phi$ fit is done, the corresponding rz hits are searched. SVX II has three 90° layers and two small-angle stereo (SAS) layers. The $r\phi$ hits and SAS hits, are used to reconstruct a silicon 3-D hits, and then a seed line of SISA track is reconstructed using 3-D hits and the primary vertex information. After making the seed line, the hits in the 90° layers are searched. Finally the candidate tracks are tested with a minimum χ^2 from all combinations. All tracks from the standalone program are refitted using a program which takes into account the energy loss and multiple scattering in the tracker material.

3.3.3 Identification Variables

The following electron identification variables are applied to the electron candidates to reject backgrounds and enhance the fraction of true electrons. Because the sub detectors are constructed differently, the identification variables are different for central and forward electrons. Figure 3.1 shows the distributions of central electron identification variables in $Z \rightarrow e^+e^-$ sample.

Central Electron

- $\mathbf{E_T}$: The transverse energy of the electron candidate is $E \times \sin\theta_e$. E is the energy of the two most energetic towers in the calorimeter cluster, and θ_e is the angle at the beam spot of the COT track matched to the seed tower of the CEM cluster.

- $\mathbf{Had/Em}$: The ratio of the total hadronic to total electromagnetic energy in the calorimeter cluster. For this quantity, all three towers in the CEM cluster are used to calculate the ratio.

- $\mathbf{E_T^{iso}}$: The electron isolation is sum of the total energy in a cone of 0.4 centered on the CEM cluster, with the three towers in the CEM cluster excluded from the sum.

- $\mathbf{P_T}$: The transverse momentum of the electron comes from the COT, beam constrained track that is matched to the CEM cluster.

- $\mathbf{E/P}$: The ratio of the cluster energy and the momentum of the COT track associated with the energy cluster is required to be consistent with that of a single charged particle. On average this is 1.0 for electrons, but because of the possibility for an electron to radiate a photon, there is a long tail in the distribution.

- $\mathbf{L_{shr}}$: A comparison between the lateral profile of the calorimeter cluster and that expected from testbeam. The energies in towers adjacent to the cluster seed tower are summed in the following way:

$$L_{shr} = 0.14 \sum_{\text{adjacent towers } i} \frac{E_i - E_i^{expected}}{\sqrt{(0.14\sqrt{E_i})^2 + (\Delta E_i^{expected})^2}}, \tag{3.1}$$

  where $E_T^{expected}$ is parameterized from the testbeam data and $\Delta E_i^{expected}$ is its error, and $0.14\sqrt{E_i}$ is the uncertainty on the energy measurement [27].

- $\mathbf{Track\ Quality\ Cuts}$: The requirements are applied on the number of segments used to construct the track. This ensures that the track has well constructed 3D information and accurate momentum resolution.

- **CES Strip χ^2** : The CES shower profile is compared with testbeam templates for the CES cluster matched to the CEM cluster. The shower profile is only compared in the z direction since bremsstrahlung commonly distorts the ϕ profile (in the direction that charged particles bend in the solenoid). The χ^2 is scaled with an energy dependent factor since the shower profile is known to change with electron $E_T(\mathrm{GeV})$ while the template is based upon single 50 GeV electrons.

- **qΔx and Δz** : The separation between the track and cluster at CES. The CES has good position resolution and can be used to determine how well a track points towards its associated cluster. The track is extrapolated to the plane of the CES and the separation between it and the CES cluster found in the $r-z$ plane, Δz, and in the $r-\phi$ plane, Δx. The magnetic field in the $r-\phi$ plane gives an asymmetry in bremsstrahlung for electrons and positrons, so an asymmetric cut is made on $q\Delta x$ rather than just on Δx.

- **Fiduciality** : In order to assure that the particle traverses an active and instrumented region of the detector, fiduciality requirements are applied. The ϕ location of the CES cluster must be within 21 cm of the center of the wedge, and the $|z|$ location must be between 9 and 230 cm. As well, the seed tower of the cluster must not be located in the highest η tower or in the region containing the solenoid cooling access.

Forward Electron

- **E_T** : The transverse energy of the electron candidate is $E \times \sin\theta_e$. E is the energy of the 2×2 tower cluster in the calorimeter.

- **Had/Em** : The ratio of the total hadronic to total electromagnetic energy in the 2×2 PEM cluster.

- $\mathbf{E_T^{iso}}$: The electron isolation is the sum of the total energy in a cone of 0.4 centered on the PEM cluster, with the four towers in the PEM cluster excluded from the sum.

- $\mathbf{PEM\ 3\times3\chi^2\ Fit}$: To ensure that the PEM cluster is consistent with an electron, the energy deposition in the 9 towers centered on the PEM cluster seed tower is fit to electron testbeam data. The χ^2 of this fit is used to measure the agreement. The fit is also required to contain at least 1 tower to avoid possible fit divergence and failures.

- $\mathbf{PES\ 5\times9\ Ratio}$: The ratio of the energy measured in the central 5 channels to the energy in the full 9 channels of the PES cluster associated with the PEM cluster. For an electron, the energy should be deposited in the center of the PES cluster, and this removes the multi-particle final states.

- $\mathbf{Track\ Quality\ Cuts}$: The PEM cluster is required to have a matched track that has been reconstructed from the COT hits or only SVX II hits. The good quality of the matched track is required to reduce the charge mis-identification of track. The quality includes E/P, the number of hits on the track, the residual between PES cluster and the extrapolated track position, and track χ^2.

3.4 The Missing Transverse Energy ($\not\!\!E_T$)

Unlike the electrons, neutrinos pass through the detector without leaving any measurable signal. Although neutrinos can not be detected directly, their presence in W events can be inferred from an imbalance of transverse energy in the calorimeter. This imbalance is termed the *missing transverse energy* and is denoted by "$\not\!\!E_T$." The $\not\!\!E_T$ for an event is calculated from all of the calorimeter towers within the region $|\eta| < 3.6$, both central

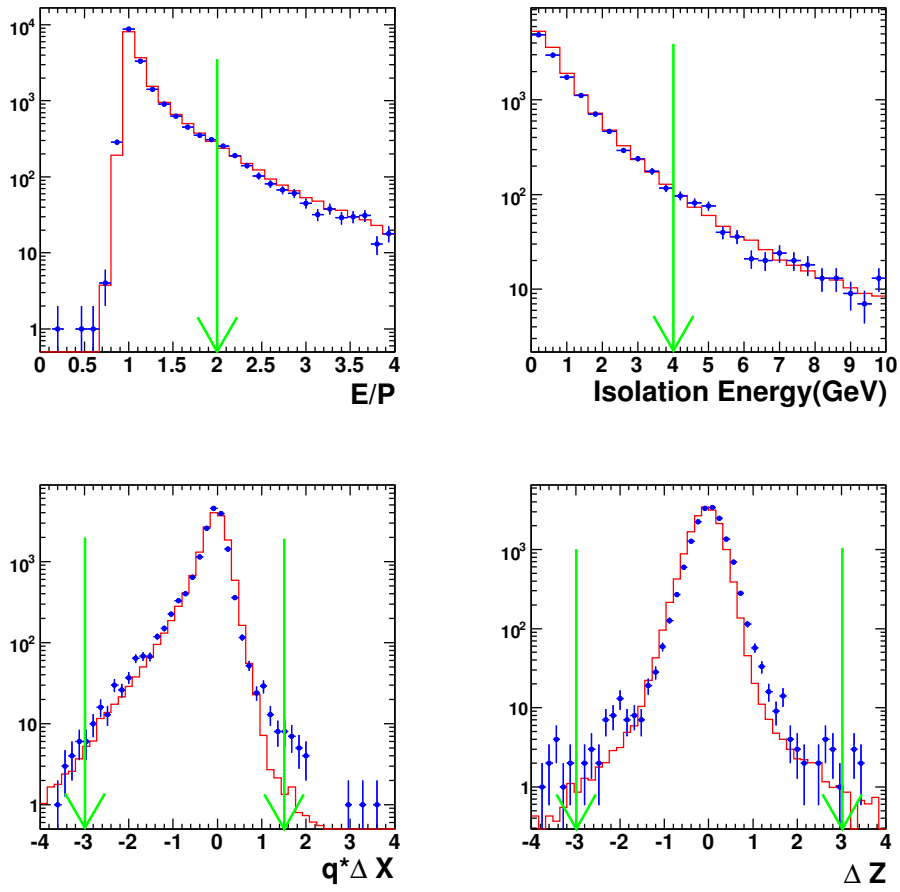

Figure 3.1: Distributions of the central electron identification variables in $Z \rightarrow e^+e^-$ sample. The points show the variables in data and the histograms show the variables in simulation. The arrows indicate the cuts used to identify electron.

and forward calorimeters. The towers are required to have greater than 100 MeV of energy to contribute to the calculation. Both the hadronic and electromagnetic energies are used in calculating $\not\!\!E_T$. As with the other basic clustering algorithms, the event vertex is initially assumed to be at $z = 0$ in the trigger and offline, and is later corrected for the measured event vertex from the electron or muon from the W decay. For events containing reconstructed muons, the calorimeter response from the muon is removed, and the $\not\!\!E_T$ corrected with the p_T of muon track. But in this analysis the correction of the muon is not issued. The last correction to the $\not\!\!E_T$ is applied after correcting the measured energy of jets in the event.

For example, the missing transverse energy in $W \rightarrow e\nu$ events is calculated from the energy deposited by the electron, the jets, and the unclustered energy using the Eqn. 3.2 :

$$\vec{\not\!\!E_T} = -\left(\vec{E}_T^{e} + \sum \vec{E}_T^{jet} + \vec{E}_T^{unc}\right), \tag{3.2}$$

For an event with a single electromagnetic cluster, $\vec{E}_T^{e}$ is simply the vector E_T associated with the cluster and the unclustered energy $\vec{E}_T^{unc}$ is determined by computing the vector sum of all calorimeter towers not part of a jet with a minimum E_T of 100 MeV as described in Section 3.3.1.

Energy that is part of a high energy jet is treated with a more sophisticated calibration than "unclustered" energy. When a jet is created in the jet clustering algorithm, a large region of the detector is spanned in order to collect all of the energy. But when covering such a large area (a cone of 0.4), the jet cone crosses several cracks within the calorimeter and also areas that may contain low-energy particles not originally from the final state parton that created the jet. In order to correct for these problems, the variation in the calorimeter tower response is corrected by applying offline calibrations and relative jet-energy corrections apply the jet response to be flat in η_d. Also the energy from

multiple interactions is removed from the jet cone using the number of reconstructed vertices in the event and the absolute energy scale of jets corrects the E_T of the jet to match the E_T of the partons within the jet cone. The absolute energy scale is measured using photon + jet balancing, measuring the hadronic calorimeter response to muons, and finally tuning the simulation response from parton showers to jets [28].

The definition of $\not\!\!E_T$ for this analysis is often called the *corrected* $\not\!\!E_T$ because it is calculated using the corrected E_T of electrons and jets. The corrected E_T of electrons and the corrected $\not\!\!E_T$ used to reconstruct W events from $W \rightarrow e\nu$ decay are shown in Figure 3.2(a) and Figure 3.2(b), respectively.

3.5 $W \rightarrow e\nu$ Selection Requirements

In the previous sections of this chapter, we described the electrons and the missing transverse energy of our W event sample. Using the objects selected by the high-E_T central and forward trigger, an electron candidate is selected within either the central calorimeter or the forward calorimeter, along with being matched to a reconstructed charged particle track. The detailed requirements and cuts used to identify electron candidates are in the CEM listed in Table 3.1. The corresponding requirements and cuts for electron candidates in the PEM are listed in Table 3.2.

The forward electrons are required to have a "good" matching CDF default track (DefTrk) to identify the charge of the electron. We refer to forward electrons with COT tracks ($1.2 < |\eta| < 1.6$) and with silicon standalone tracks (SISA) ($1.6 < |\eta| < 2.8$) as shown in the following cuts.

In order to optimize the requirements used to select the default tracks for the forward region, each of the cuts is optimized with $Z \rightarrow e^+e^-$ events in both the Run II data and Monte Carlo simulation, for both COT and silicon tracks. Using maximum value of ϵD^2 , where ϵ is the tracking efficiency and D is dilution factor, $D =$

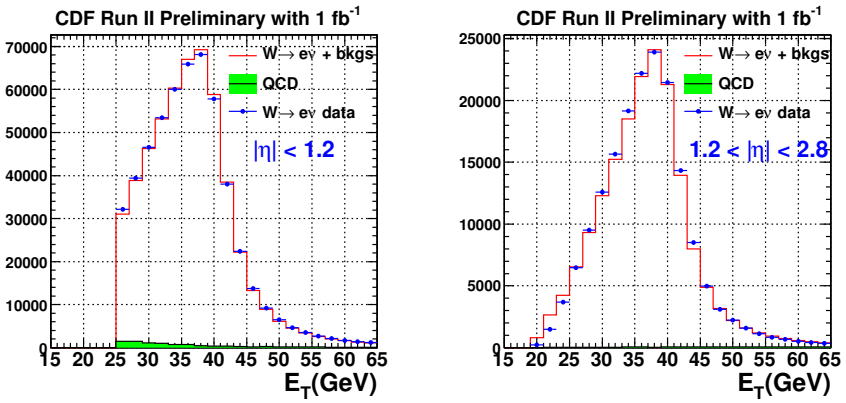

(a) Electron Transverse Energy

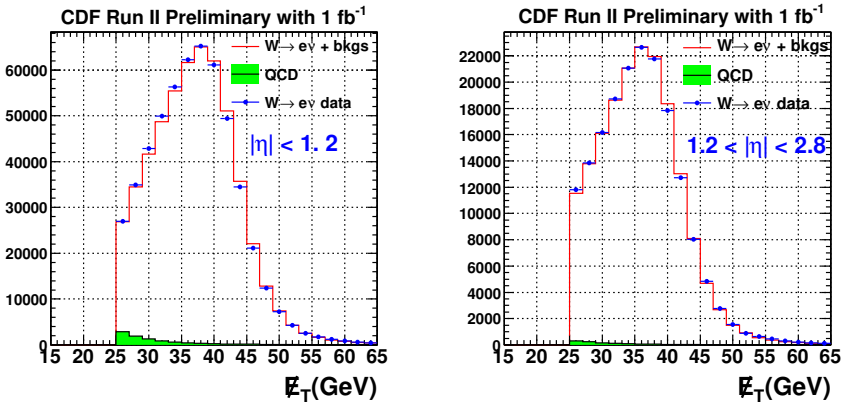

(b) Missing Transverse Energy

Figure 3.2: The electron transverse energy and missing transverse energy in $W \rightarrow e\nu$ sample for the central electron(left) and the forward electron(right).

Variable	Central Electron
Fiducial	TRUE
E_T	$\geq$ 25 GeV
Track $\lvert Z_0 \rvert$	$\leq$ 60 cm
Track p_T	$\geq$ 10 GeV/c
COT Ax. Seg.	$\geq$ 3
COT St. Seg.	$\geq$ 2
Conversion	$\neq$ 1
Had/Em	$\leq (0.055 + (0.00045 \times E))$
Isolation	$\leq$ 4 GeV
LshrTrk	$\leq$ 0.2
E/P	$\leq$ 2.0 unless $p_T \geq$ 50GeV/c
CES ΔZ	$\leq$ 3.0 cm
Signed CES ΔX	-3.0 $\leq q \times \Delta X \leq$ 1.5
CES Strip χ^2	$\leq$ 10.0

Table 3.1: Central electron selection cuts.

Variable	Forward Electron
Region	$1.2 \leq \lvert\eta\rvert \leq 2.8$
E_T	$\geq$ 20 GeV
Had/Em	$\leq$ 0.05
Pem3x3FitTow	$\neq$ 0
Pem3x3Chisq	$\leq$ 10
Pes5by9U	$\geq$ 0.65
Pes5by9V	$\geq$ 0.65
Isolation	$\leq$ 4 GeV
ΔR_{PesPem}	$\leq$ 3.0 cm
DefMatch*	TRUE
COT track**	TRUE
otherwise SISA track***	TRUE

Table 3.2: Forward electron selection cuts. DefMatch* : The highest P_T track should be within a cone size $\Delta R = \sqrt{(\Delta X)^2 + (\Delta Y)^2} < \sqrt{2}$. COT track** : COT Ax. and St. hits $\geq$ 5, Silicon hits $\geq$ 3, $\chi^2/dof <$ 10 and 0.2 $<$ E/P $<$ 4.0. SISA track*** : $|\eta| >$ 1.6, Silicon hits $\geq$ 5, $\chi^2/dof <$ 5, $|\Delta X|$, $|\Delta Y| <$ 0.4 and 0.65 $<$ E/P $<$ 4.0.

$2(1 - \rho_{charge\ fake\ rate}) - 1$, the requirements of good matching track are optimized so as to minimize the charge mis-identification rate and to maximize the electron acceptance. The distributions of the track variables are shown in Figure 3.3 (GEN5) and in Figure 3.4 (GEN6) and demonstrate the quality of these tracks. We find that GEN6 MC has better agreement with data than GEN5 MC. In particular, the residuals (ΔX and ΔY) on PES show a discrepancy between GEN5 MC and data. This affects the electron track efficiency scale factor (shown later in Section 6.6).

Additionally, to select $W \rightarrow e\nu$ events, we reject the low missing energy events, $\not\!\!E_T$ $<$ 25 GeV.

3.6 $Z \rightarrow e^+e^-$ Selection Requirements

The $Z \rightarrow e^+e^-$ sample is used to set the calorimeter energy scale, to determine the electron charge fake rate, to determine the signal template for QCD background estimate, and to measure the electron identification efficiencies. Most of the Z selection requirements are identical to the description in Section 3.5. For forward electrons we have an additional electron tracking type, the Phoenix electron track (PHX), to increase the acceptance. The requirements for PHX tracks are shown in Table 3.3.

The geometric requirements on selected events are that two electron candidates are identified in either the central ($|\eta| < 1$) or forward regions of the detector. Events in which both electrons are reconstructed in the central region of the detector are referred to as central-central (CC), events with one central and one forward electron are referred to as central-forward (CF), and events in which both electrons are forward are referred to as forward-forward (FF).

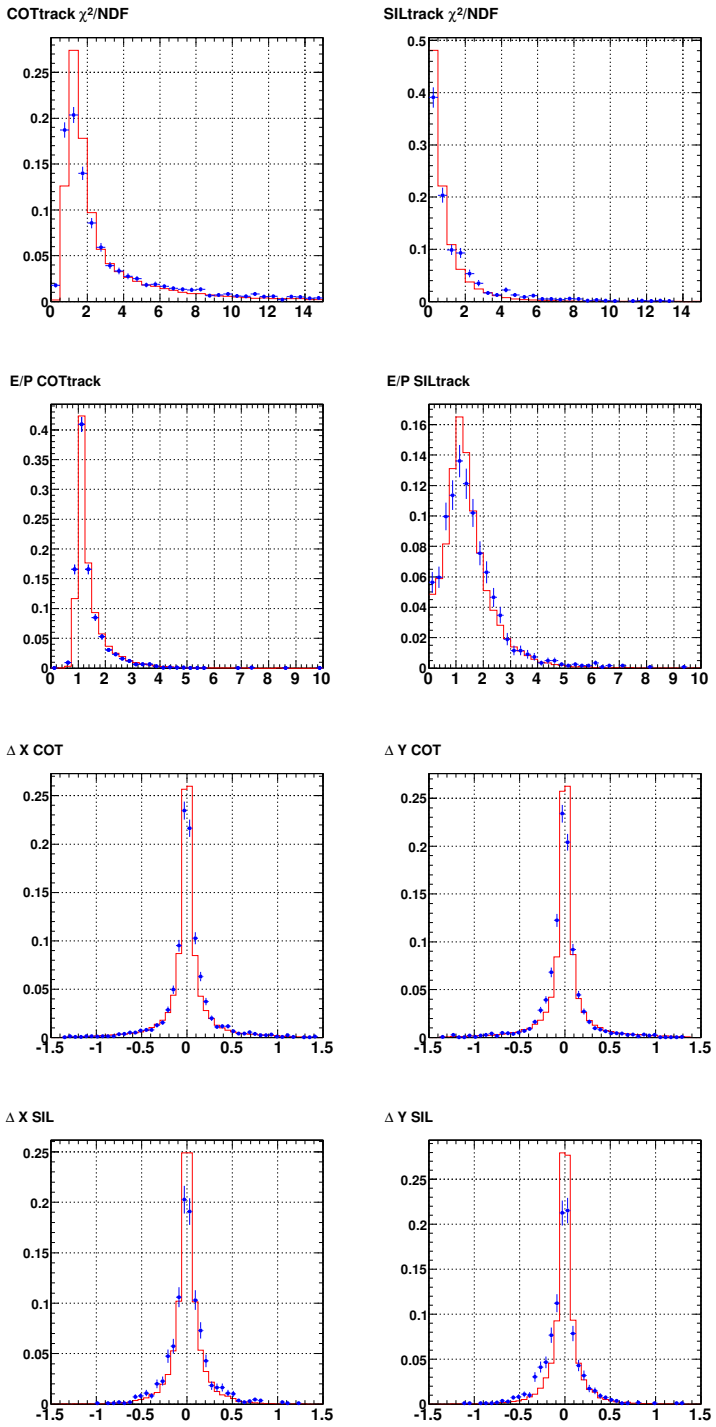

Figure 3.3: Good matching track variables from $Z \rightarrow e^+e^-$ events in the forward region. Points and histograms are Run II data and Monte Carlo simulation (GEN5), respectively. COT tracks ($1.2 < |\eta| < 1.6$) and SISA tracks ($1.6 < |\eta| < 2.8$).

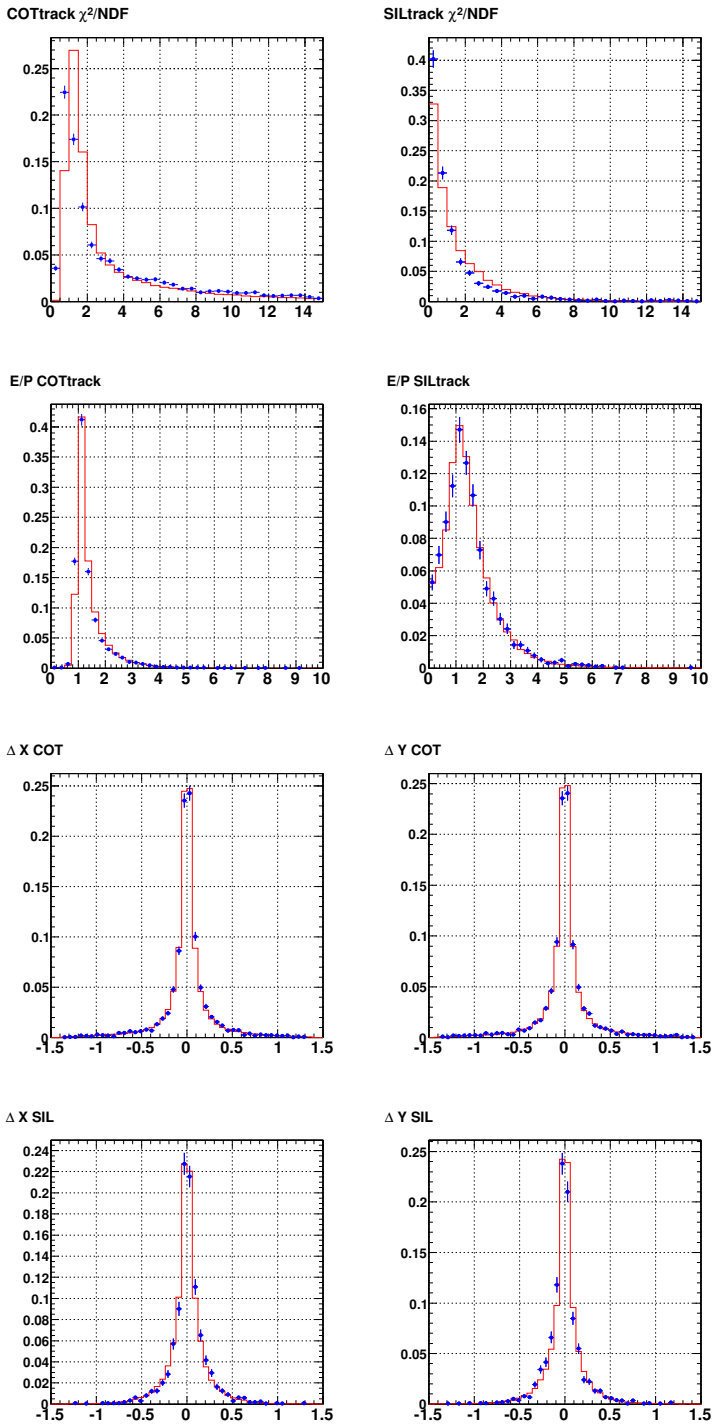

Figure 3.4: Good matching track variables from $Z \rightarrow e^+e^-$ events in the forward region. Points and histograms are Run II data and Monte Carlo simulation (GEN6), respectively. COT tracks ($1.2 < |\eta| < 1.6$) and SISA tracks ($1.6 < |\eta| < 2.8$).

Variable	PHX
Region	== plug
E_T	$\geq$ 25 GeV
Pes2dEta	$1.2 \leq \lvert\eta\rvert \leq 2.8$
Had/Em	≤ 0.05
Pem3x3FitTow	$\neq 0$
Pem3x3Chisq	≤ 10
Pes5by9U	≥ 0.65
Pes5by9V	≥ 0.65
Isolation	$\leq$ 4 GeV
ΔR_{PesPem}	$\leq$ 3.0 cm
PHXMatch	TRUE
$N_{hits}^{Silicon}$	≥ 3
$\lvert z_0^{PHX}\rvert$	$\leq$ 60 cm

Table 3.3: Phoenix electron selection cuts.

Chapter 4

Background Determination

As described in Chapter 3, we selected $W \rightarrow e\nu$ candidates by identifying high-p_T electrons in events with a large missing transverse energy. Although the $W \rightarrow e\nu$ selection is designed to reject events other than direct W production, a few other physics processes with identical final-state signatures also pass the selection cuts. We separate the background sources into two main categories: QCD backgrounds to electrons, and events containing real electrons. The most significant $W \rightarrow e\nu$ background is the direct QCD production of multi jets. In some QCD multi jet events, a jet mimics the signature of an electron, and mismeasured transverse energy results in a large apparent $\not\!\!E_T$. Other physics processes that contribute to our W event sample include $W \rightarrow \tau\nu$ ($\tau \rightarrow e\nu$), $Z \rightarrow e^+e^-$ and $Z \rightarrow \tau^+\tau^-$. The production cross section for $W \rightarrow \tau\nu$ is identical to that of $W \rightarrow e\nu$, and the τ lepton decays to an electron with a branching fraction of 18%. In $Z \rightarrow e^+e^-$ events, a large $\not\!\!E_T$ can be observed if an electron is mismeasured or escapes through an uninstrumented part of the detector. In this chapter we describe the techniques used to estimate the contributions to our candidate $W \rightarrow e\nu$ sample from each background source and are to be used in the measurement of the W production charge asymmetry analysis.

4.1 Electroweak Backgrounds

The backgrounds to $W \rightarrow e\nu$ include other electroweak processes that yield an electron and $\not\!\!E_T$ in the final state. The three principal backgrounds in this category are $Z \rightarrow e^+e^-$, $Z \rightarrow \tau^+\tau^-$ and $W \rightarrow \tau\nu$.

4.1.1 $Z \rightarrow e^+e^-$ Background

The second type of boson background is from $Z \rightarrow e^+e^-$ production. Although the cross section times branching ratio for $Z \rightarrow e^+e^-$ is a factor of 10 smaller than that of $W \rightarrow e\nu$, the presence of a high E_T electron, together with a large $\not\!\!E_T$, can produce an experimental signature identical to that of $W \rightarrow e\nu$. Whereas the electron E_T spectra for $Z \rightarrow e^+e^-$ and $W \rightarrow e\nu$ are similar, the large $\not\!\!E_T$ in $Z \rightarrow e^+e^-$ events results from mismeasured jets or a second electron that passes through an uninstrumented region of the detector. We measure the $Z \rightarrow e^+e^-$ background by generating $Z \rightarrow e^+e^-$ events using PYTHIA as described in Section 3.1.2.

4.1.2 $Z \rightarrow \tau^+\tau^-$ Background

$Z \rightarrow \tau^+\tau^-$ events can fake a W when one of the τ's decays to an electon or its hadronic decay fakes an electron. Again the PYTHIA Monte Carlo generator and detector simulation were used.

4.1.3 $W \rightarrow \tau\nu$ Background

The $W \rightarrow e\nu$ signature can also be reproduced by $W \rightarrow \tau\nu$ events in which the τ lepton subsequently decays into an electron via $\tau \rightarrow e\nu\bar{\nu}$. $W \rightarrow \tau\nu$ accounts for one third of all leptonic W decays, and the τ has a significant branching fraction (18%) to electrons. The experimental signatures of both $W \rightarrow e\nu$ and $W \rightarrow \tau\nu$ consist of an true electron

Source	Contribution to $W \rightarrow e\nu$	
region	central	plug
$Z \rightarrow e^+e^-$	$0.593 \pm 0.018\%$	$0.542 \pm 0.025\%$
$Z \rightarrow \tau^+\tau^-$	$0.091 \pm 0.004\%$	$0.101 \pm 0.008\%$
$W \rightarrow \tau\nu$*	$2.295 \pm 0.036\%$	$2.044 \pm 0.050\%$

Table 4.1: Estimates of $Z \rightarrow e^+e^-$, $Z \rightarrow \tau^+\tau^-$ and $W \rightarrow \tau\nu$ contributions to the $W \rightarrow e\nu$ sample. Note that $W \rightarrow \tau\nu$ ($\tau \rightarrow e\nu$) is not considered to be a background but is included in the signal acceptance for the W charge asymmetry analysis.

and $\not\!\!E_T$. The electron from τ decay is generally softer than that of direct $W \rightarrow e\nu$ decay because the momentum of the τ is shared among three decays products. Many $W \rightarrow \tau\nu$ events are therefore rejected by the electron E_T cut. To study this process, samples of $p\bar{p} \rightarrow W \rightarrow \tau\nu$ are generated as described in Section 3.1.2.

In order to estimate the background fractions from the electroweak bosons, we apply the $W \rightarrow e\nu$ selection cuts to these events to obtain the fraction of events that pass the cuts. Then, based on Standard Model predictions for the relative production rates of our signal process and the three background processes, we use the estimated acceptances from Monte Carlo to obtain the relative contributions of each process to our candidate sample. The results from $Z \rightarrow e^+e^-$, $Z \rightarrow \tau^+\tau^-$ and $W \rightarrow \tau\nu$ are summarized in Table 4.1, and in Figure 4.1, the rapidity distribution and the background effects on the charge asymmetry are shown. However, we do not consider the $W \rightarrow \tau\nu$ ($\tau \rightarrow e\nu$) decay channel as a background in the W charge asymmetry analysis since it has same charge asymmetry as $W \rightarrow e\nu$. Instead we add $W \rightarrow \tau\nu$ events which pass our analysis cuts to our signal sample of $W \rightarrow e\nu$ events and the difference in reconstructed rapidity since the electron comes from the τ decay instead of the W decay directly is taken into account as a smearing effect. Thus it is considered in the end as the part of the total signal.

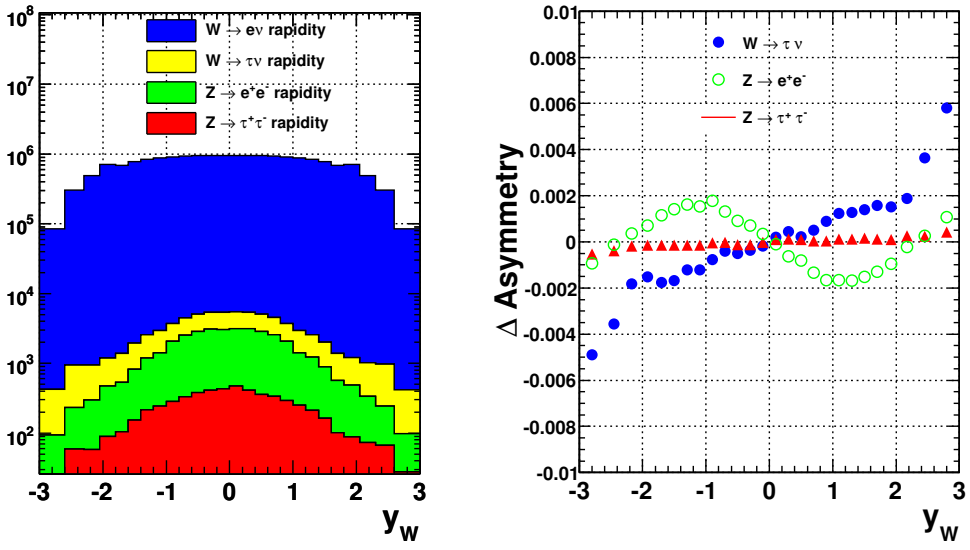

Figure 4.1: The rapidity distribution of $Z \rightarrow e^+e^-$, $Z \rightarrow \tau^+\tau^-$ and $W \rightarrow \tau\nu$ that pass the $W \rightarrow e\nu$ selection cuts to compare to $W \rightarrow e\nu$ signal event. The right plot shows systematic uncertainty on asymmetry measurement when these other electroweak processes are considered in the data.

4.2 QCD Background

Extracting the contribution of events to the $W \rightarrow e\nu$ candidate samples in which real or fake leptons from hadronic jets are reconstructed in the detector is challenging. Real leptons are produced both in the semileptonic decay of hadrons and by photon conversions in the detector material. Some events also contain other particles in hadronic jets which are misidentified and reconstructed as leptons. Typically, these types of events will not be accepted into our $W \rightarrow e\nu$ candidate sample because we require large event $\not\!\!E_T$. In a small fraction of these events; however, a significant energy mis-measurement anywhere in the calorimeter does reproduce the $\not\!\!E_T$ signature. Because of the large total cross section for hadronic jets, even this small fraction of such events passing our selections results in a substantial number of background events in our $W \rightarrow e\nu$ signal region.

In this section, we present a technique for estimating the QCD background in $W \rightarrow e\nu$ events by fitting the isolation distribution of the electrons [29]. The principal idea behind the method is to exploit the differences in the shapes of the isolation distribution of jets compared to that of electrons. We obtain a template shape for electrons (signal) from $Z \rightarrow e^+e^-$ events and a template shape for jets (background) from a dijet enriched sample described below. This is done separately for central electrons and for forward (plug) electrons, and the isolation shapes are fitted in each detector to extract a background measurement from the data itself.

4.2.1 Electron (Signal) Template

To obtain the electron template for the isolation distribution for electrons we use $Z \rightarrow e^+e^-$ data samples. The selections for centeral and forward electrons are different because of the differences in the detectors

Central electrons

We select central-central electrons where one electron passes the central electron cuts in Table 3.1 (the electrons whose isolation distribution will be used in the template), except for the isolation cut, and where the other electron candidate passes a tighter electron selection which requires tighter cuts of isolation ratio (E_T^{iso}/E_T) $<$ 0.05 and L_{shr} $<$ 0.1. We also use central-forward events where one electron passes the central cuts (the electron used to measure the electron isolation template), except for the isolation cut, and where the other electron candidate passes the tight phoenix cuts in Table 3.3 including a cut on isolation ratio $<$ 0.05. We also require 81 GeV $< M_{ee} <$ 101 GeV for the two electrons in these events. The background fraction of central-central $Z \rightarrow e^+e^-$ is small and can be ignored, but the background in the central-forward(PHX) $Z \rightarrow e^+e^-$ sample must be subtracted from that electron template. The details of the background constribution in the $Z \rightarrow e^+e^-$ sample will be discussed at the end of this section.

In Figure 4.2 (top) we check the E_T dependence of the isolation distribution for data (black points). Since we use the isolation distribution from electrons from $Z \rightarrow e^+e^-$ events as a template for electrons from $W \rightarrow e\nu$ events, we also compare the E_T dependence to $Z \rightarrow e^+e^-$ MC (red) as well as $W \rightarrow e\nu$ MC (blue) and find that they both agree well with the data. We also check the dependence of the isolation shape on $\not\!\!E_T$ for $W \rightarrow e\nu$ MC events and separately for different E_T ranges; this is shown in Figure 4.2 (bottom). We observe that for $\not\!\!E_T < 35$ GeV there is no dependence of the isolation shape on $\not\!\!E_T$ but find a dependence on $\not\!\!E_T$ for events with $\not\!\!E_T$ above 35 GeV (as well as an E_T dependence). Therefore, we have two signal templates for the isolation distribution, one for 25 GeV $< \not\!\!E_T <$ 35 GeV and the other for $\not\!\!E_T >$ 35 GeV. In Figure 4.3 we compare the shape of the isolation distributions of electrons from W and Z decay by looking at the ratio of the distributions in bins of isolation.

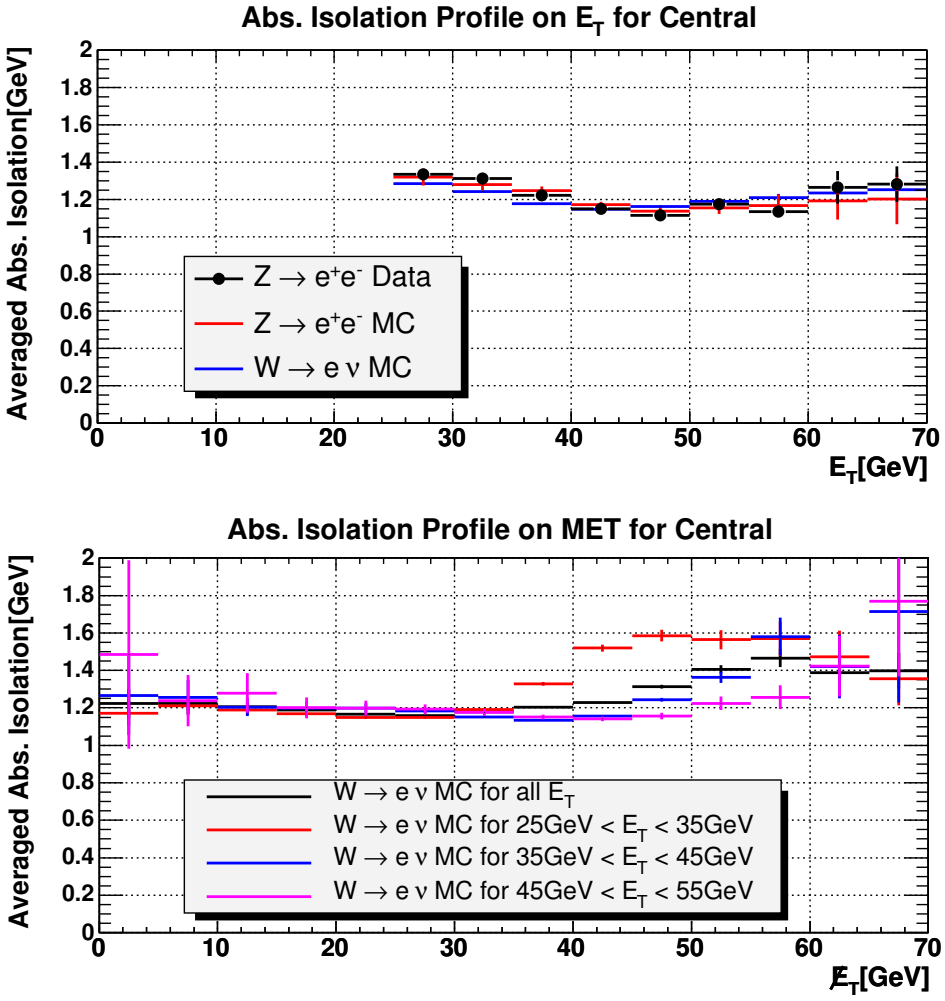

Figure 4.2: Profile plot of the isolation distribution for central electrons vs. E_T (top) and vs. $\not\!\!E_T$ (bottom).

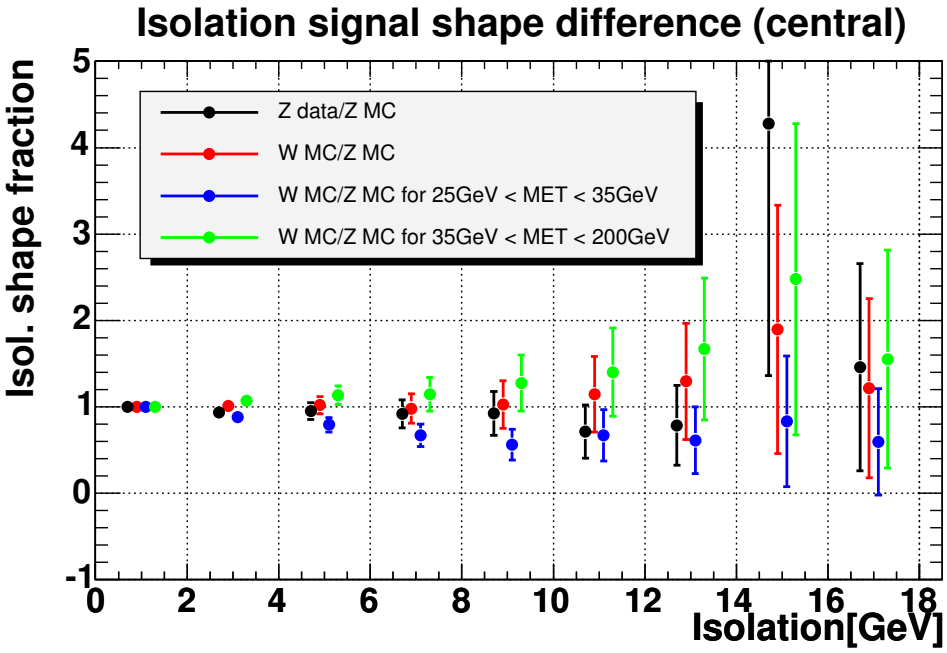

Figure 4.3: Shape comparisons of the isolation distribution. Shown are the ratios of the isolation distributions in bins of isolation for central electrons for Z data/Z MC (black), W MC/Z MC (red), W MC/Z MC for 25 GeV $< \not\!\!E_T <$ 35 GeV (blue) and W MC/Z MC for 35 GeV $< \not\!\!E_T <$ 200 GeV (green).

Forward electrons

Similar to what was done for central electrons, we use $Z \rightarrow e^+e^-$ events to obtain the electron template for the isolation distribution for forward electrons. Here, we select central-forward electrons where one electron passes the forward electron cuts and default track requirements in Table 3.2 (the electron used in the isolation template), except for the isolation cut, and where the other electron candidate passes a tighter central electron selection which requires tighter cuts of isolation ratio < 0.05 and $L_{shr} < 0.1$. We also use forward-forward events where one electron passes the DefTrack cuts (the electron used to form the isolation template), except for the isolation cut, and where the other passes the PHX cuts and in addition passes a cut on isolation ratio < 0.05. We also require 81 $\mathrm{GeV} < M_{ee} <$ 101 GeV. We use two signal templates for the forward isolation distribution, one for 25 GeV $< \not\!\!E_T <$ 35 GeV and one for $\not\!\!E_T >$ 35 GeV, as was done in the central electron case.

Background contamination for electron templates

Since the background contaminations for central-forward and forward-forward Zs in the template samples are non-negligible, the signal template needs to be corrected for these backgrounds. First, we estimate the amount of background by selecting central-forward and forward-forward events as described above, except that the fitting leg is forced to have isolation $>$ 2 GeV for the electron, and then fit the dielectron invariant mass distribution to a Gaussian plus a 3rd order polynomial as illustrated in Figure 4.4. The polynomial is used to interpolate the background shape under the largely Gaussian signal region, and therefore can be used to estimate the background events contributing to the templates with isolation $>$ 2 GeV. The background fraction for electron templates are summarized in Table 4.2.

We subsequently subtract this fraction of background events from the signal isola-

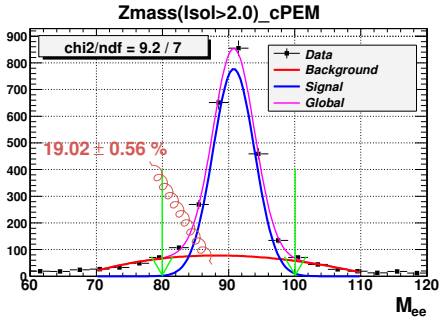

(a) Z(CF) is applied by PEM cuts

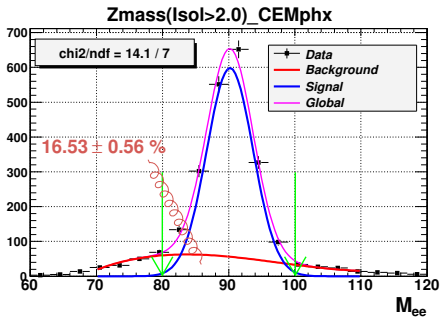

(b) Z(CF) is applied by PHX cuts

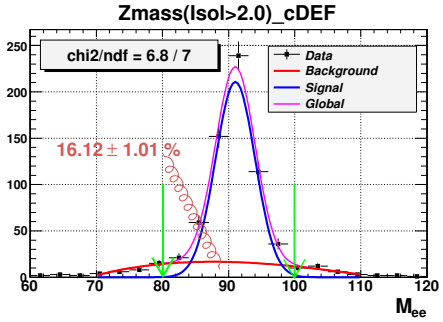

(c) Z(CF) is applied by PEM+DefTrk cuts

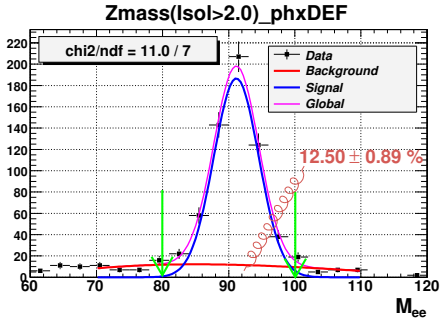

(d) Z(CF) is applied by PHX+DefTrk cuts

Figure 4.4: Invariant mass distribution reconstructed from central-forward and forward-forward electrons as described in the text. We require that the electron candidate has non-isolated energy, Isolation$>$ 2 GeV. We fit the distribution to a Gaussian plus a 3rd order polynomial to get an estimate of the background contamination in the signal region of 81 GeV $< M_{ee} <$ 101 GeV.

$80GeV/c^2 < M_{ee} < 100GeV/c^2$	Background Fraction(%)
$Z \rightarrow e^+e^-$ CF(PEM)	0.677 ± 0.020 %
$Z \rightarrow e^+e^-$ CF(PHX)	0.691 ± 0.024 %
$Z \rightarrow e^+e^-$ CF(Def)	0.479 ± 0.030 %
$Z \rightarrow e^+e^-$ CF(PHX+Def)	0.326 ± 0.023 %

Table 4.2: The summary of background estimates for the electron template in $Z \rightarrow e^+e^-$ events.

tion template, using the background isolation shape described in section 4.2.2. In this subtraction the signal template has negative bins in the high isolation region due to the statistical limit in $Z \rightarrow e^+e^-$ data. In order to fit $W \rightarrow e\nu$ data we make the negative value to be zero. This effect on the fit results is much smaller than the systematic uncertainty due to the background shape, which will be discussed in Section 4.2.4. The signal shapes after eliminating the background contamination are shown in Figure 4.5.

4.2.2 Jet (Background) Template

We obtain the jet background template for the isolation distribution for QCD jets faking electrons from the inclusive high-p_T electron data. Again, because of differences in the calorimeters, the central and forward regions are treated differently.

Central jet

We select dijet events where one jet passes anti-electron cuts in Table 4.3 (the jet used to form the background template), and where the other jet passes the jet cuts in Table 4.3. Although these cuts select primarily dijet candidates, some electron signal events still remain in this sample. To remove dielectron events we require no more than one cluster with EM transverse energy $>$ 15 GeV, and to remove W + jet events we require $\not\!\!E_T <$ 10 GeV and that the angle between the jets in the $r - \phi$ plane is near 180 degrees. The

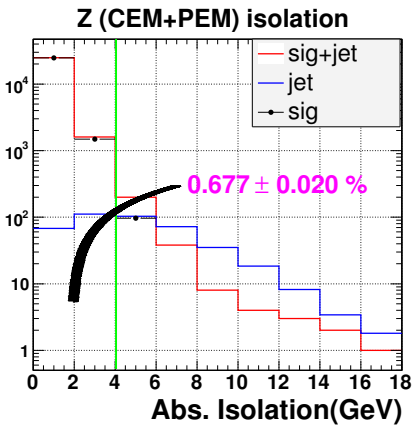

(a) Z(CF) is applied by PEM cuts

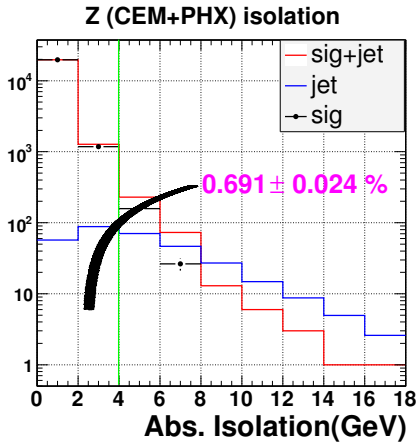

(b) Z(CF) is applied by PHX cuts

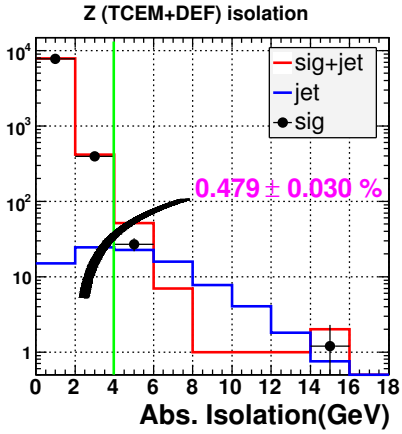

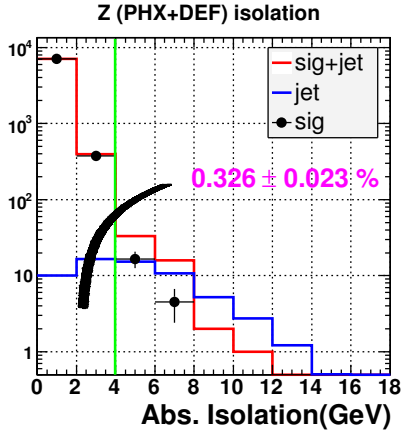

(c) Z(CF) is applied by PEM+DefTrk cuts and Z(FF) is applied by PHX and DefTrack for each electron

Figure 4.5: The signal isolation distribution. Black point is the signal shape, red is $Z \rightarrow e^+e^-$ data before removing background and blue is the background shape.

Variable	Anti-CEM	variable	JET
Region	== central	Region	== central or forward
Fiducial	1	JetCluster	0.4
E_T	$\geq$ 25 GeV	Jet E_T	$\geq$ 25 GeV
Track Z_0	$\leq$ 60 cm	Had/Em	$\geq$ 0.125
Track p_T	$\geq$ 10 GeV/c		
Had/em	$\geq (0.055 + (0.00045 \times E))$		
LshrTrk	$\leq$ 0.2		
E/P	$\leq$ 2.0 (unless $p_T \geq$ 50GeV/c)		
CES ΔZ	$\leq$ 5.0 cm		
Singed CES ΔX	-3.0 $\leq q \times \Delta X \leq$ 1.5		
CES StripChi2	$\leq$ 10.0		
$\lvert\Delta\phi_{\rm jj}\rvert$	if $15 < P_T < 25$, $\lvert\Delta\phi_{\rm jj}\rvert \geq 2.8$ else $\lvert\Delta\phi_{\rm jj}\rvert \geq 2.6$		
nEmObj	== 1		
nJet	== 1		
$\not\!\!E_T$	$\leq$ 10 GeV		

Table 4.3: Dijet event selection criteria for the QCD background estimate for central electrons.

distribution of $r - \phi$ angles between the jets is shown in Figure 4.6 for the dijet sample and for $W \rightarrow e\nu$ MC. We also show this distribution in three ranges of the p_T of the dijets with the blue dashed line indicating cut for the different p_T values. These cuts in angle are summarized in Table 4.3.

Forward jet

As was done for central electrons, we select dijet events where one jet behaves like an forward electron but passes anti-electron cuts in Table 4.4 (the jet used to form the background template), and where the other passes the jet cuts in Table 4.4.

In Figure 4.7 (top) we show the $\not\!\!E_T$ distribution of the dijet events in the data, and $W \rightarrow e\nu$, $W \rightarrow \tau\nu$ and $Z \rightarrow e^+e^-$ MC. We use the MC for these electroweak processes

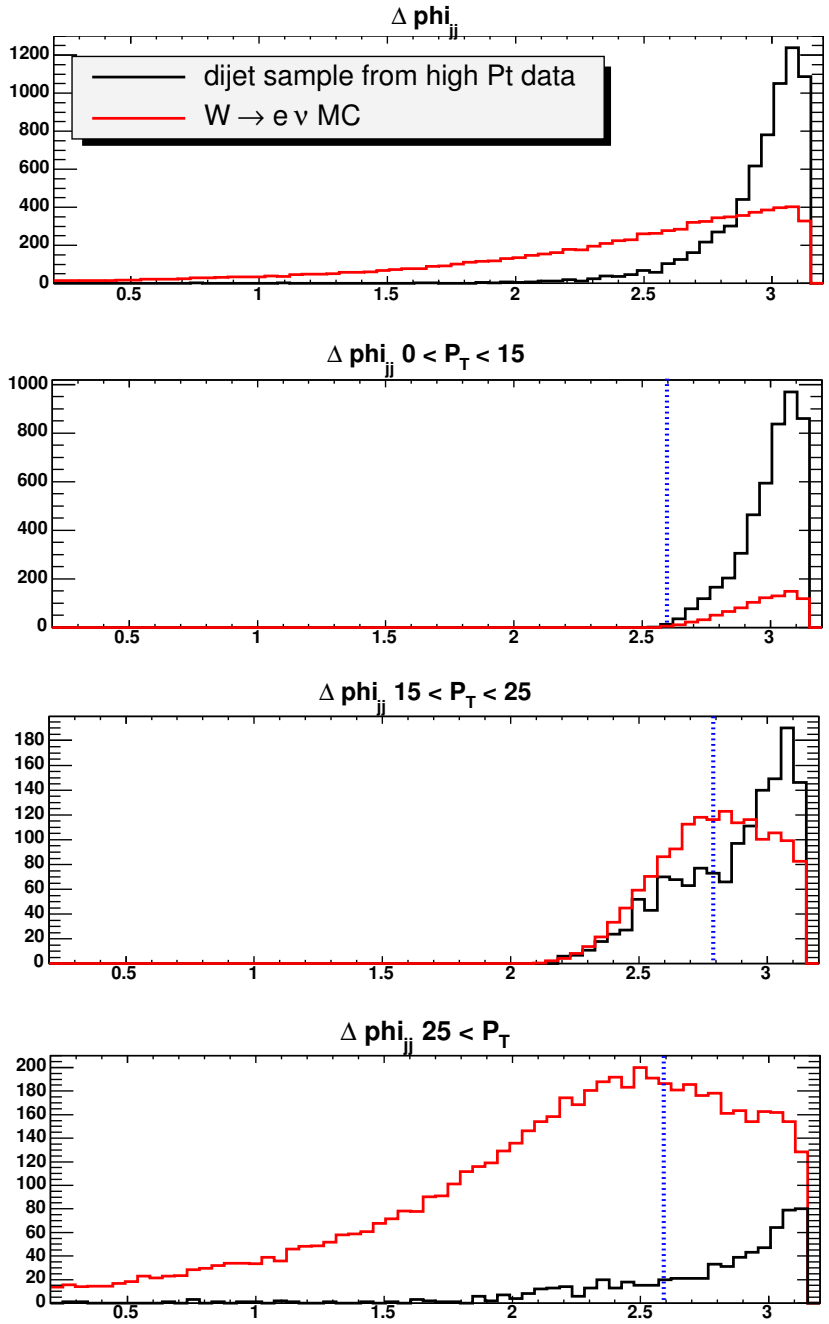

Figure 4.6: The opening angle (in the $x-y$ plane), $\Delta\phi$, distribution between the jet-like central electron (non-isolated and $Had/Em > 0.05$) and the leading jet in high p_T electron data (black). We compare this with the W plus jet events from MC (red) as a function of the p_T of the dijets. The blue dashed line represents the dijet event selection cut for the different p_T as summarized in Table 4.3.

Variable	Anti-PEM	variable	JET
Region	== forward	Region	== central or forward
Pes2dEta	$1.2 \leq \|\eta\| \leq 2.8$	JetCluster	0.4
E_T	$\geq$ 20 GeV	Jet E_T	$\geq$ 25 GeV
Had/Em	≥ 0.05	Had/Em	≥ 0.125
Pem3x3FitTow	$\neq 1$		
ΔR_{PesPem}	≤ 3.0		
DefTrk	TRUE		
$\|\Delta\phi_{\text{jj}}\|$	if $15 < P_T < 25$, $\|\Delta\phi_{\text{jj}}\| \geq 2.8$ else $\|\Delta\phi_{\text{jj}}\| \geq 2.6$		
nEmObj	== 1		
nJet	== 1		
$\not\!\!E_T$	$\leq$ 10 GeV		

Table 4.4: Dijet event selection criteria for the QCD background estimate for forward electrons.

to subtract the remaining contributions from real electron events to obtain the final jet background templates in the central and forward region, respectively. In Figure 4.7 (bottom) we show the isolation distributions for dijet events for 0 GeV $< \not\!\!E_T <$ 10 GeV and 10 GeV $< \not\!\!E_T <$ 20 GeV. Because these are significantly different, we use the differences in the shapes of these distributions as a measurement of the systematic uncertainty in the background shape as discussed in Section 4.2.4.

4.2.3 Isolation Fit Results

Electrons from the selected $W \rightarrow e\nu$ candidate data are composed of signal and background contributions, and it is these candidate event distributions in isolation that we fit with the signal shape described in section 4.2.1 and background shape described in section 4.2.2. The fit itself uses a binned maximum likelihood method. The fit results for central and forward electron are shown in Figure 4.8. We estimate the QCD background fraction in the total central and forward $W \rightarrow e\nu$ candidate sample to be ($1.21 \pm 0.14_{\text{stat}}$)

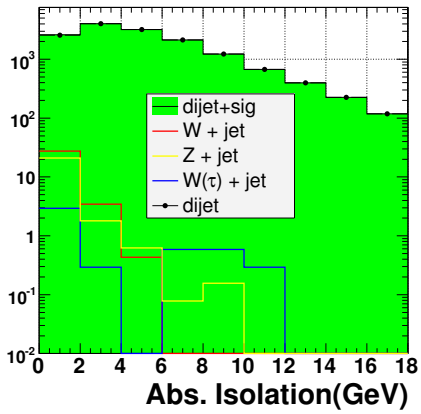

(a) $\not\!\!E_T$ for central jet

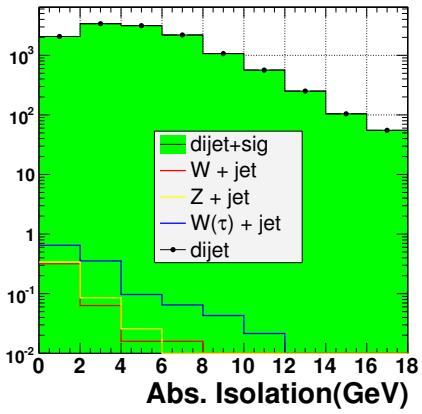

(b) $\not\!\!E_T$ for forward jet

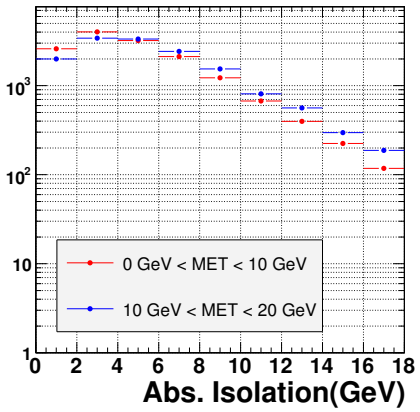

(c) E_T^{iso} for central jet

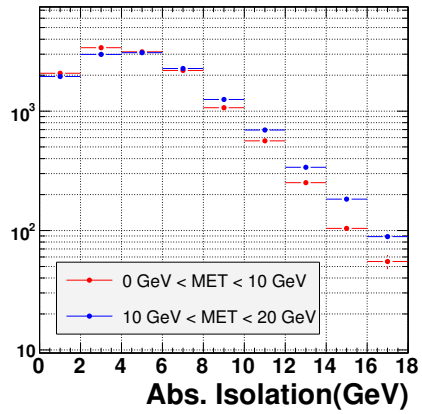

(d) E_T^{iso} for forward jet

Figure 4.7: Top: $\not\!\!E_T$ distribution of the dijet events in data (black points) and for $W \rightarrow e\nu$, $W \rightarrow \tau\nu$, and $Z \rightarrow e^+e^-$ MC. We correct the dijet data for these electroweak processes. Bottom: The isolation distribution for dijet events for 0 GeV $< \not\!\!E_T <$ 10 GeV (red) and 10 GeV $< \not\!\!E_T <$ 20 GeV (blue). The isolation distribution for 0 GeV $< \not\!\!E_T <$ 10 GeV is used as the background template for electrons.

$\%$ and ($0.67 \pm 0.12_{\rm stat}$) $\%$, respectively.

4.2.4 Systematic Uncertainty in QCD Background Estimate

We consider several possible sources of systematics uncertainty in the QCD background estimate: In the electron subtraction of jet templates, jet isolation shape differences for different $\not\!\!E_T$ regions as in Figures 4.7, and uncertainties in the background subtraction of the forward electron template.

To evaluate the uncertainty in the electron subtraction from the jet templates, we consider a $\pm 1\sigma$ statistical variation on the electron content of the jet template and re-extract the background with these varied templates. In a similar way, we re-extract the background fraction we find if we use different $\not\!\!E_T$ cuts in forming the jet template. For forward electrons, we propagate the fit errors from the Z mass distributions through to the evaluation of the final background. These systematic uncertainties on the QCD background estimates for $W \rightarrow e\nu$ candidates in the central and in the forward are summarized in Table 4.5 and Table 4.6, respectively.

4.3 Summary of Backgrounds to the $W \rightarrow e\nu$ Sample

We have introduced the background sources to the $W \rightarrow e\nu$ sample to be used for the W charge asymmetry analysis. The background contributions are estimated for two categories, the electroweak processes and hadronic jets. For the hadronic jet background we have used an method by fitting the isolation shape of electron candidates from $W \rightarrow e\nu$ data. Table 4.7, 4.8 summarize the total background estimates for central and forward $W \rightarrow e\nu$ candidates.

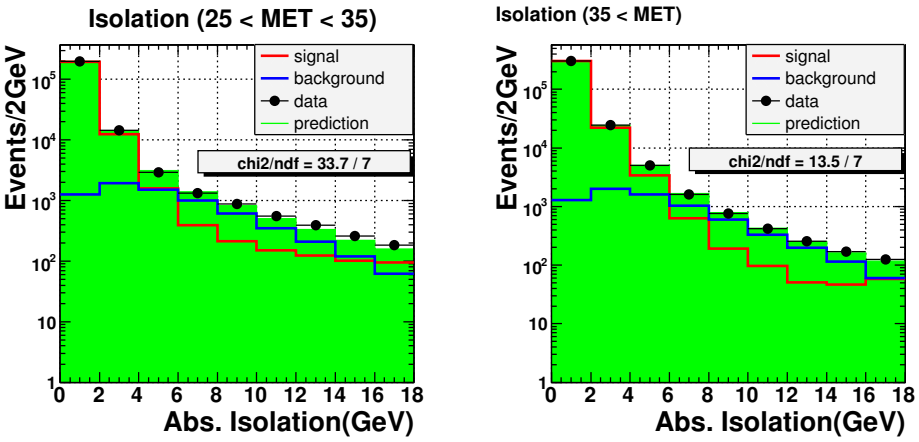

(a) E_T^{iso} for central electron

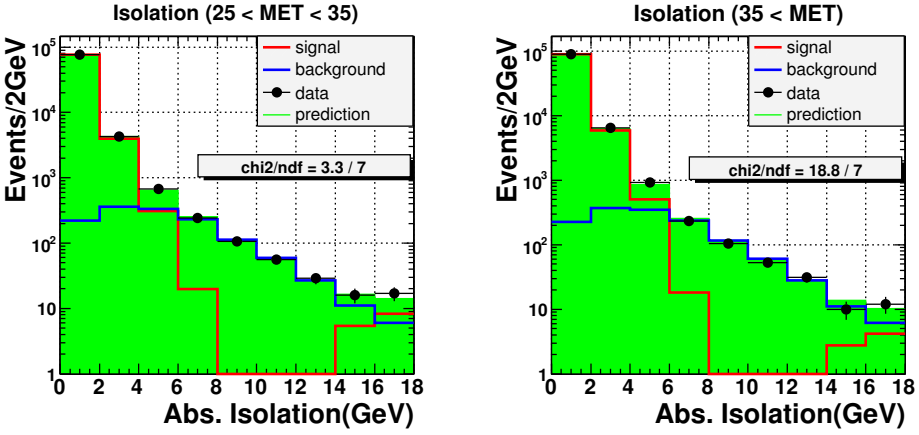

(b) E_T^{iso} for forward electron

Figure 4.8: Isolation fit distributions for the $W \rightarrow e\nu$ data (black dots), signal template (red), background template (blue) and the prediction from the fit (green). The results for two different $\not\!\!E_T$ regions are presented : $25\mathrm{GeV} < \not\!\!E_T < 35\mathrm{GeV}$ (left) and $\not\!\!E_T > 35\mathrm{GeV}$ (right). (a) for central electrons. (b) for forward electrons.

sources of the systematic	central		
	$25 < \not\!\!E_T < 35$	$35 < \not\!\!E_T$	total
Electron subtraction of jet template	0.002	0.000	0.002
Jet shape difference for $\not\!\!E_T$ regions	0.105	0.100	0.145
Jet subtraction of electron template	0.014	0.010	0.017
total syst.(%)	± **0.146**		

Table 4.5: Systematic uncertainties on the QCD background estimate in central electron candidates.

sources of the systematic	forward		
	$25 < \not\!\!E_T < 35$	$35 < \not\!\!E_T$	total
Electron subtraction of jet template	0.002	0.000	0.002
Jet shape difference for $\not\!\!E_T$ regions	0.098	0.094	0.136
Jet subtraction of electron template	0.027	0.036	0.045
total syst.(%)	± **0.143**		

Table 4.6: Systematic uncertainties on the QCD background estimate in forward electron candidates.

Central	events	BG/DATA fraction (%)
DATA	537858	
$Z \to e^+e^-$	3173.36	0.59 ± 0.02 (stat.)
$Z \to \tau^+\tau^-$	487.21	0.09 ± 0.00 (stat.)
$W \to \tau\nu$	12370.73	2.30 ± 0.04 (stat.)
QCD	6508.08	1.21 ± 0.14 (stat.) ± 0.15 (syst.)

Table 4.7: The predicted background contribution in central $W \to e\nu$ candidates. The error represents the statistical uncertainty and the systematic uncertainty caused by our isolation fit method (QCD).

Forward	events	fraction (%)
DATA	176941	
$Z \rightarrow e^+e^-$	955.48	0.54 ± 0.03 (stat.)
$Z \rightarrow \tau^+\tau^-$	179.81	0.10 ± 0.01 (stat.)
$W \rightarrow \tau\nu$	3609.60	2.04 ± 0.05 (stat.)
QCD	1185.50	0.67 ± 0.12 (stat.) ± 0.14 (syst.)

Table 4.8: The predicted background contribution in forward $W \rightarrow e\nu$ candidates. The error represents the statistical uncertainty and the systematic uncertainty caused by our isolation fit method (QCD).

Chapter 5

Analysis Technique

In this chapter, since the W decay to leptons, in our case $W^{\pm} \rightarrow e^{\pm}\nu$, involves a neutrino whose longitudinal momentum cannot be experimentally determined. I explain my analysis technique to resolve the kinematic ambiguity of the longitudinal momentum of the neutrino in order to directly reconstruct the $W^{\pm}$ rapidity. The neutrino longitudinal momentum is constrained by the W mass,

$$M_W^2 = (E_l + E_\nu)^2 - (\vec{P_l} + \vec{P_\nu})^2 \tag{5.1}$$

The W mass, M_W, is experimentally measured [30, 31, 32, 33, 34, 35, 36, 37] to be $80.403 \pm 0.029\ \mathrm{GeV}$.

Since the missing energy is reconstructed in $x - y$ plane as defined in Section 3.4 the energy, momentum and direction of neutrino are determined from the reconstructed $\not\!\!E_T$ and are used in Eq. 5.1. There are some events which cannot satisfy the W mass constraint with real values of the neutrino z-momentum due to a mis-reconstruction of the neutrino (missing) transverse energy, $\not\!\!E_T$. In such cases, we do not change the direction but re-scale the magnitude of $\not\!\!E_T$ to the value which makes the imaginary part to be zero. This new $\not\!\!E_T$ is then used to correct the y_W for the event.

The W mass constraint in Eq. 5.1 results in a two-fold ambiguity. This ambiguity can be partly resolved on a statistical basis from the known $V-A$ (vector-axial vector) decay distribution using the center-of-mass decay angle between the electron and the proton, θ^*, and from the W^+ and W^- production cross-sections as a function of W rapidity, $d\sigma^{\pm}/dy_W$. These are discussed in the next sections.

5.1 $V-A$ decay distribution

$W^{\pm}$ bosons at the Tevatron are primarily produced from the valence quarks in the proton and in the anti-proton and rarely from sea anti-quarks because W production requires at least one moderately high x parton to be involved in the collision. At very large forward or backward rapidities where one very high x parton must participate in the production, the production probability from the sea quarks nearly vanishes. Understanding of the sea quark contribution affects the decay angle distributions from the $V-A$ structure because W production by sea anti-quarks will result in the opposite W polarization from valence quark production.

We use a Monte Carlo simulation based on the MC@NLO generator with NLO QCD corrections [38] to determine the production probability from sea anti-quarks by identifying the initiating partons of the W production reaction in different regions of y_W. As expected, the angular distribution from production of $W^{\pm}$ with quarks in the proton follows a $(1+cos\theta^*)^2$ distribution and the production from anti-quarks in the proton flips the sign of the angular term. For example, in Fig. 5.1(a), we show the cosθ^* distributions of e^+ in the W^+ rest frame for the case when a quark from the proton and an anti-quark from the anti-proton form the W^+ (labeled "quark") and the case when an anti-quark from the proton and a quark from the anti-proton form the W^+ (labeled "anti-quark"). The ratio of quark (proton) and anti-quark (proton) induced W production therefore determines the angular decay distribution. In the simulation, we measure the fraction

of quark and anti-quark contributions, and parameterize the angular distributions for y_W and the W transverse momentum, p_T^W. We find an empirical functional form that fits the data,

$$P_{\pm}(cos\theta^*, y_W, p_T^W) = (1 \mp cos\theta^*)^2 + Q(y_W, p_T^W)(1 \pm cos\theta^*)^2, \tag{5.2}$$

$$Q(y_W, p_T^W) = f(p_T^W) e^{-[g(p_T^W) * {y_W}^2 + 0.05 * |{y_W}^3|]}, \tag{5.3}$$

where the functions $f(p_T^W)$ and $g(p_T^W)$ are

$$\begin{aligned} f(p_T^W) &= 0.2811 \mathcal{L}(p_T^W, \mu = 21.7\text{GeV}, \sigma = 9.458\text{GeV}) \\ &\quad + 0.2185 e^{(-0.04433\text{GeV}^{-1} p_T^W)}, \\ g(p_T^W) &= 0.2085 + 0.0074\text{GeV}^{-1} p_T^W \\ &\quad - 5.051 \times 10^{-5}\text{GeV}^{-2} {p_T^W}^2 \\ &\quad + 1.180 \times 10^{-7}\text{GeV}^{-3} {p_T^W}^3. \end{aligned} \tag{5.4}$$

Here $\mathcal{L}(x, \mu, \sigma)$ is the Landau distribution with most probable value μ and the RMS σ. The first term of Eq. 5.2 corresponds to the contribution from quarks in the proton and the second term from anti-quarks in the proton. The parameterization, $Q(y_W, p_T^W)$, the ratio of the two angular distributions as a function of the W rapidity and p_T^W, is obtained from the fit to the distribution in Fig. 5.1(b). Figure 5.2 and Figure 5.3 compare the NLO QCD prediction with LO prediction for $Q(y_W, p_T^W)$ in Figure 5.2 and the functions $f(p_T^W)$ and $g(p_T^W)$ in Figure 5.3.

5.2 The differential cross section, $d\sigma^{\pm}/dy_W$

A second relevant factor distinguishing the two W rapidity solutions is the W differential cross-section as a function of y_W, $d\sigma^{\pm}/dy_W$. The W boson production decreases sharply beyond $|y_W| > 2$ because of the scarcity of high x quarks as shown in Figure 5.4.

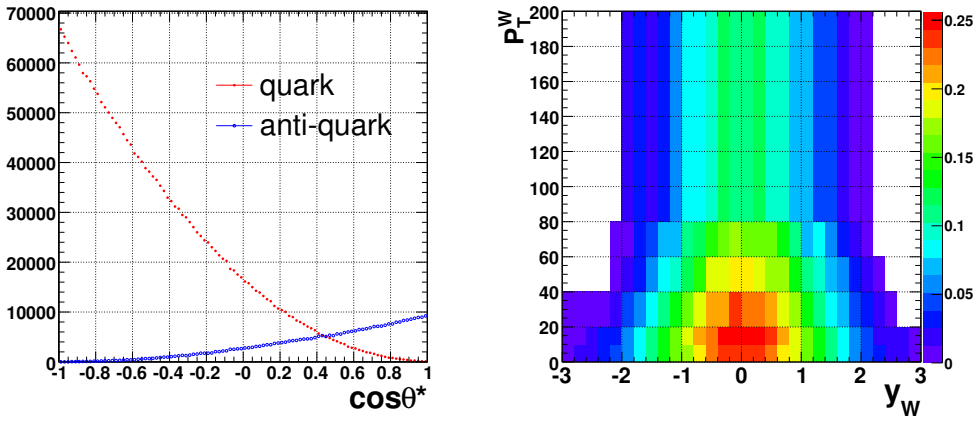

(a) (b)

Figure 5.1: (a) The cosθ^* distributions of e^+ in the W^+ rest frame, averaged over all produced W^+. The curve labeled "quark" shows the case when a quark from the proton and anti-quark from the anti-proton form the W^+. The curve labeled "anti-quark" shows the opposite case, when an anti-quark from the proton and a quark from the anti-proton form the W^+. (b) The dependence of the ratio of "anti-quark" ($\bar{q}$) and "quark" (q) contributions to the overall W decay angle distribution, $Q(y_W, p_T^W)$, as a function of W rapidity and p_T of the W.

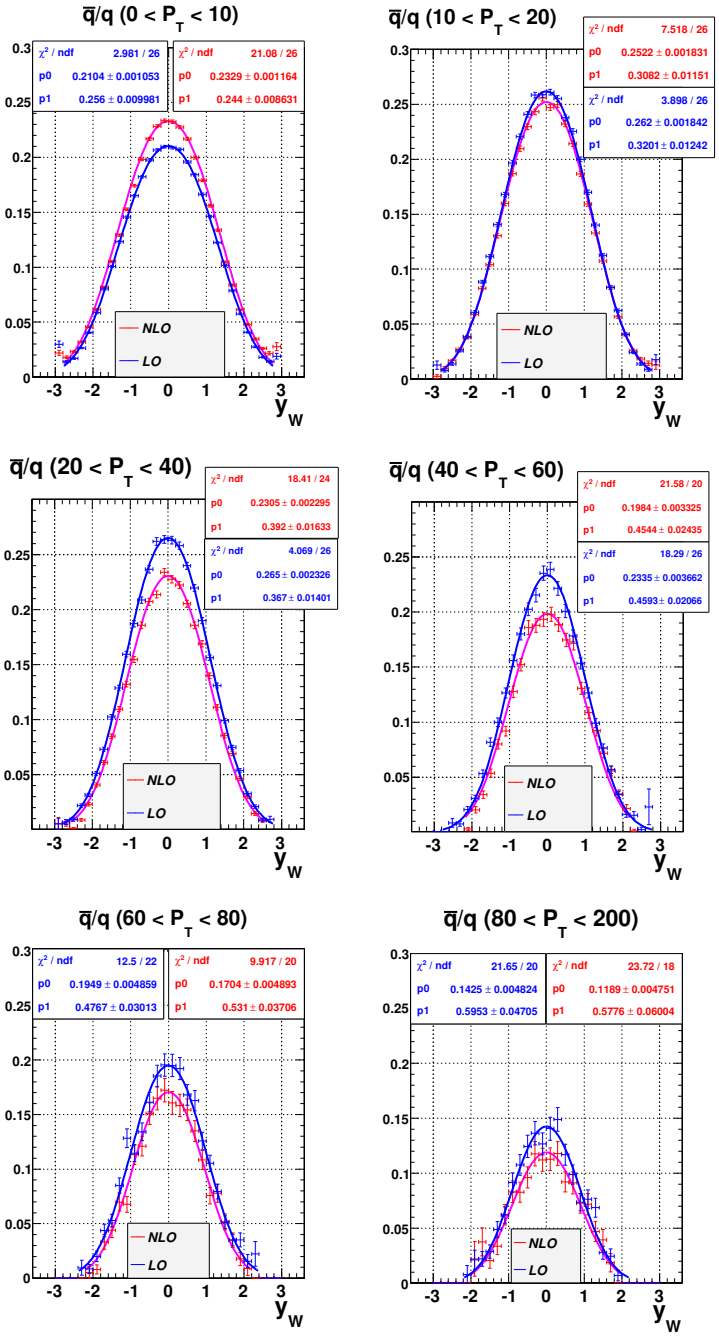

Figure 5.2: The ratio of anti-quark and quark in $\cos\theta^*$ distribution as a function of y_W and P_T^W.

For instance, if one of the two possible solutions falls in the central region of rapidity and the other has $|y_W| > 2$, the former should receive more weight as the latter is very unlikely to be produced. As mentioned in Section 1.3, we use a simulation to leading order (LO) in QCD, but we apply a the $K(y_W)$ factor which includes next-to-next-to leading order in QCD to the cross section,

$$K(y_W) = \frac{d\sigma^{NNLO}(y_W)}{d\sigma^{LO}(y_W)}, \tag{5.5}$$

The rapidity distributions of W through NNLO in QCD [22] are shown in Figure 5.4 with the $K(y_W)$.

5.3 Event Reconstruction Probability

The information used to select among the two solutions can be represented by a weighting factor for each rapidity solution and charge, $w^{\pm}_{1,2}$, can be represented as

$$w^{\pm}_{1,2} = \frac{P^{\pm}(cos\theta^*_{1,2}, y_{1,2}, P^W_T)\sigma^{\pm}(y_{1,2})}{P^{\pm}(cos\theta^*_1, y_1, P^W_T)\sigma^{\pm}(y_1) + P^{\pm}(cos\theta^*_2, y_2, P^W_T)\sigma^{\pm}(y_2)}, \tag{5.6}$$

where the $\pm$ signs indicate the W boson charge and indices of 1, 2 are for the two W rapidity solutions. In Eq 5.6, the weighting factor depends primarily on the W^+ and W^- cross-sections, but also depends on the W charge asymmetry itself. Therefore, this method requires us to iterate the procedure to eliminate the dependence of the asymmetry on the weighting factor for our measurement. The iteration starts with a known predicted $\sigma^+(y_W)$ and $\sigma^-(y_W)$ used in the weighting factor to reconstruct $W^{\pm}$ rapidity from real data, and then the reconstructed $W^{\pm}$ rapdity provides new $\sigma^+(y_W)$ and $\sigma^-(y_W)$. The iteration procedure subsequently reproduces the measurement of W charge asymmetry.

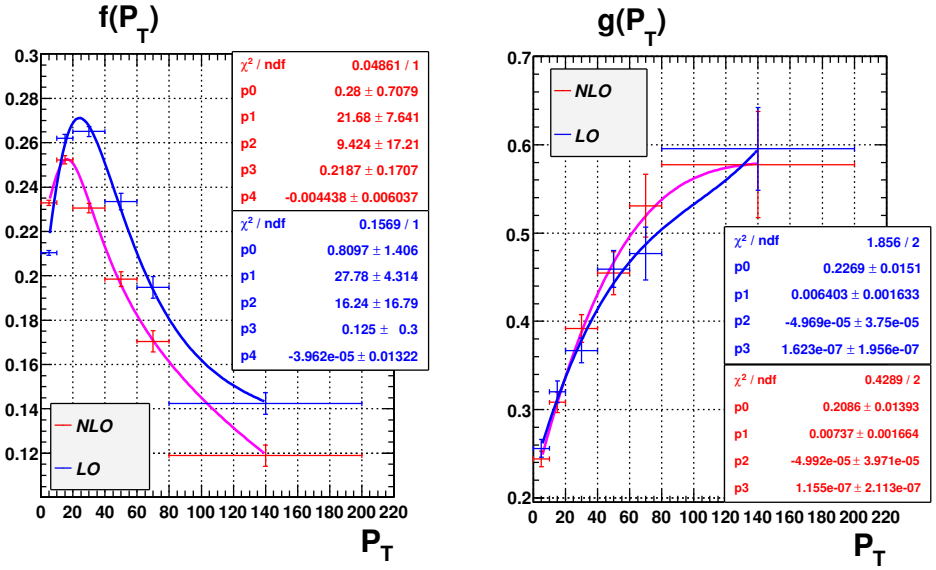

Figure 5.3: $\bar{q}/q$ parameterization functions.

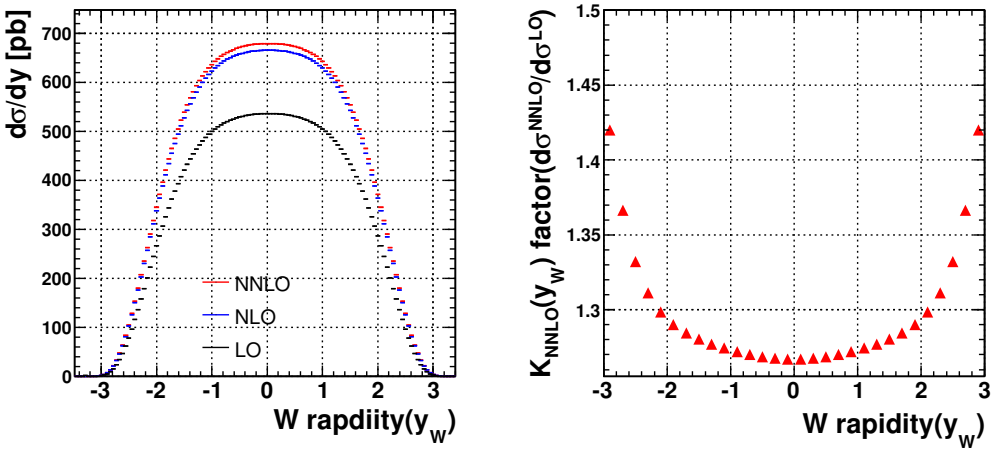

Figure 5.4: The comparison of the W rapidity with NNLO, NLO, and LO QCD predictions (left). The K-factor is determined from the fraction of NNLO and LO predicted distributions (right).

Chapter 6

Corrections

In this chapter, we describe corrections to address several experimental effects and to remove the biases which affect our measurement. In order to measure the W charge asymmetry in $W \rightarrow e\nu$ decay, any detector acceptances and event selection efficiencies that treat positive and negative events differently must be accounted for. Similarly, any sources contributing to the mismeasurement of electron charge and W rapidity must also be accounted for. These effects include:

- electron energy scale and resolution
- W boson recoil energy
- charge mis-identification in the central and forward tracking
- backgrounds
- trigger efficiency and electron identification efficiency (the difference between what is expected from the simulation and what is measured in data is referred to as a ”scale factor”)
- effects of smearing in reconstructed rapidity and detector acceptance

6.1 Energy Scale Determination

Both energy scale and resolution corrections are applied to the electron energy. Using a control sample of $Z \rightarrow e^+e^-$ events, the energy scale and resolution are determined for both the collected data and the generated Monte Carlo. This procedure sets the absolute calibration of the central and forward calorimeters or the "energy scale". The energy scale is numerically a factor which multiplies the initial energy measurement of the calorimeter before matching the invariant mass distribution of $Z \rightarrow e^+e^-$ candidates in Monte Carlo to the one in the data. An energy resolution factor is applied to improve agreement in the width of the invariant mass distribution of $Z \rightarrow e^+e^-$ candidates by adding additional smearing to that already in the simulation.

The formula used to tune the cluster E_T scale is shown in Eq 6.1 and the energy resolution is tuned using a random number pulled from Gaussian distribution with width $\sigma_{E_T} = R_s \times E_T$, where R_s is the energy resolution factor.

$$(E_T^{scale})' \;=\; (K_s \times E_T) \tag{6.1}$$

In order to determine the CEM and PEM energy scales, the calorimeter scales are varied in small steps in the simulated data and the resulting Z mass peak monitored. To measure the CEM scale, the sample used were central-central dielectron events, and for the PEM scale the scale was studied using central-forward dielectron events. In the PEM, independent energy scales for four different regions, $-2.8 < \eta_d < -1.6$, $-1.6 < \eta_d < -1.2$, $1.2 < \eta_d < 1.6$, $1.6 < \eta_d < 2.8$, are considered. At each energy scale step a χ^2 is calculated between the rescaled simulated Z mass peak and the data. The fit is made in the mass window 80 $\mathrm{GeV/c^2} < M_{ee} <$ 100 $\mathrm{GeV/c^2}$. This small window is used to reduce bias from any mismodeling of the radiative tail in the simulation. The energy resolution is studied in the same way, by introducing extra smearing on top of

the best-fitting value in the simulation by generating a random number from a Gaussian distribution with mean equal to E_T and width equal to a chosen σ_{E_T} for each lepton candidate in our samples and calculating χ^2 at each step. The mass peaks are shown in Figure 6.1, 6.2 and 6.3. The χ^2 distributions are shown in Figure 6.4, 6.5 and 6.6. The cluster E_T scaling and smearing factors in Table 6.1 and 6.2 are applied to the lepton energy in the $W \rightarrow e\nu$ Monte Carlo sample used to measure W charge asymmetry. As part of this work, appropriate energy scalings were found for data in different offline versions (GEN5 and GEN6) which correspond to different periods of data taking.

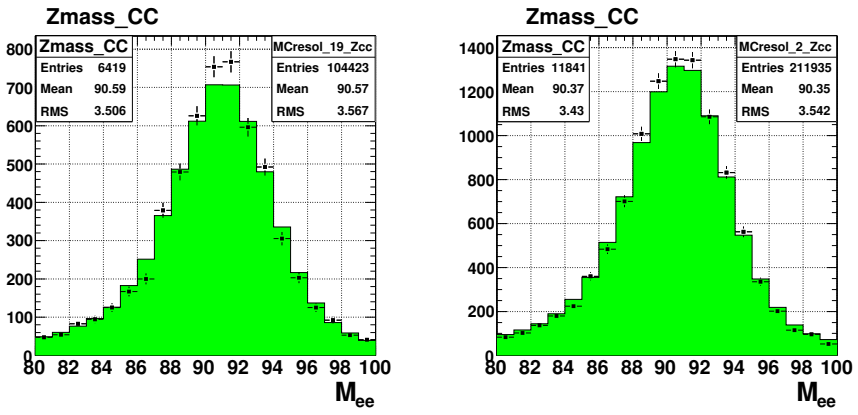

(a) GEN5 MC (b) GEN6 MC

Figure 6.1: M_{ee} for central-central events : The plots show the scaling and smearing giving the best χ^2 fit between data and simulation.

6.2 Boson Recoil Energy Scale Determination

The modeling of hadronic showering, the boson recoil-energy, and the underlying event energy in the Monte Carlo may be inaccurate and could lead to differences between the

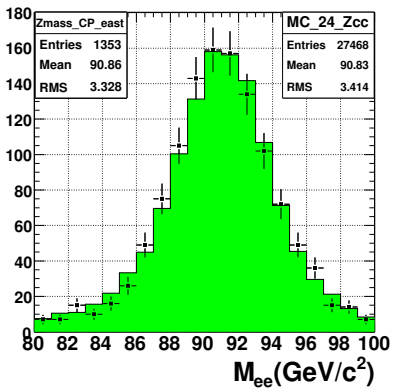

(a) $1.2 < \eta < 1.6$

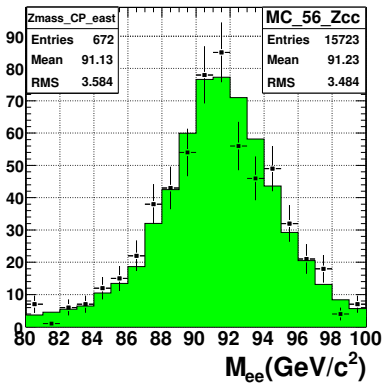

(b) $1.6 < \eta < 2.8$

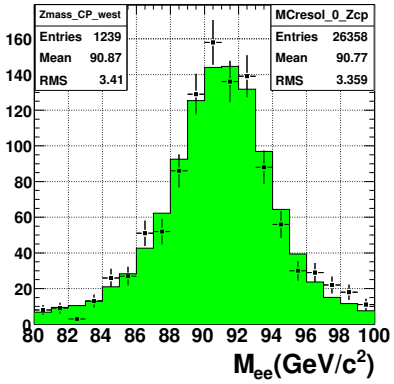

(c) $-1.6 < \eta < -1.2$

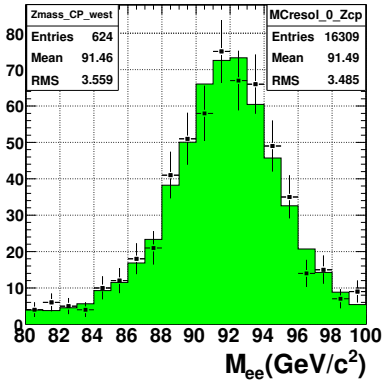

(d) $-2.8 < \eta < -1.6$

Figure 6.2: central-forward events for GEN5: The comparison of the $Z \rightarrow e^+e^-$ invariant mass between data and MC.

.

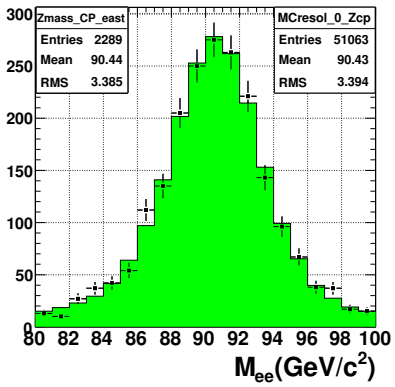

(a) $1.2 < \eta < 1.6$

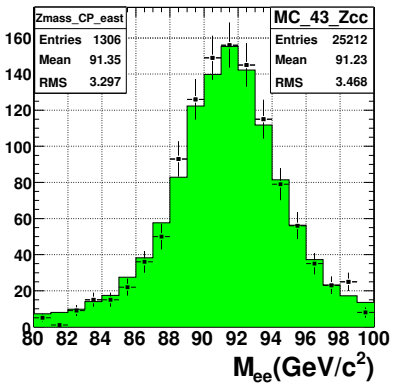

(b) $1.6 < \eta < 2.8$

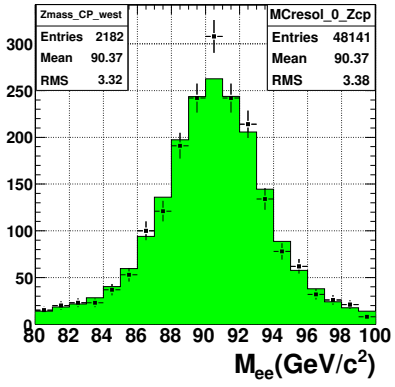

(c) $-1.6 < \eta < -1.2$

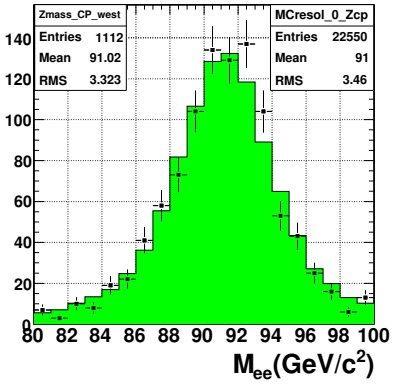

(d) $-2.8 < \eta < -1.6$

Figure 6.3: central-forward events for GEN6 : The comparison of the $Z \rightarrow e^+e^-$ invariantmass between data and MC.

.

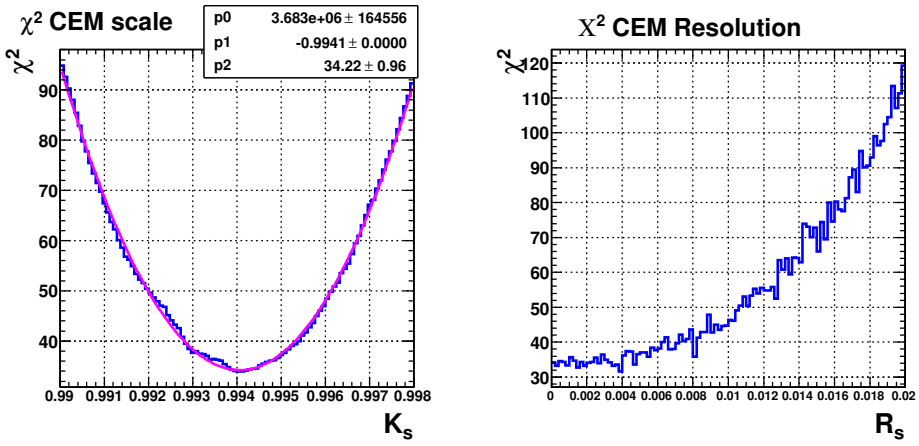

(a) GEN5 MC

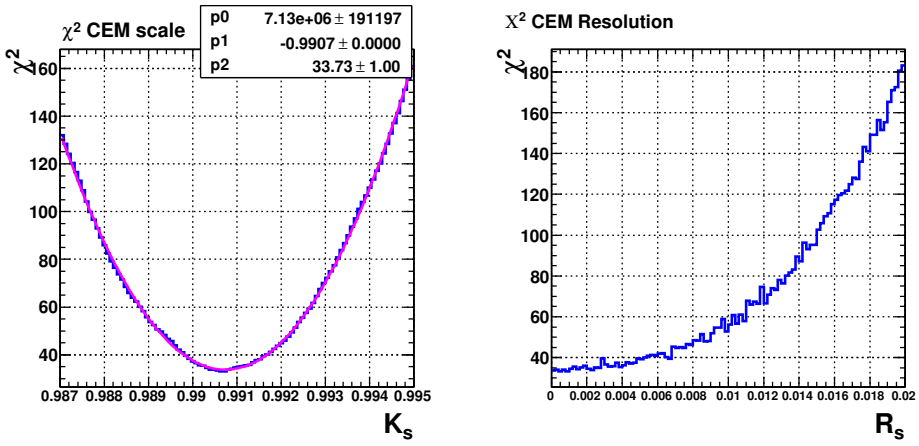

(b) GEN6 MC

Figure 6.4: Central electrons : The best χ^2 fit of the $Z \rightarrow e^+e^-$ invariant mass comparison between data and MC for the cluster E_T energy scale. The fit formula is $p0(x + p1)^2 + p2$.

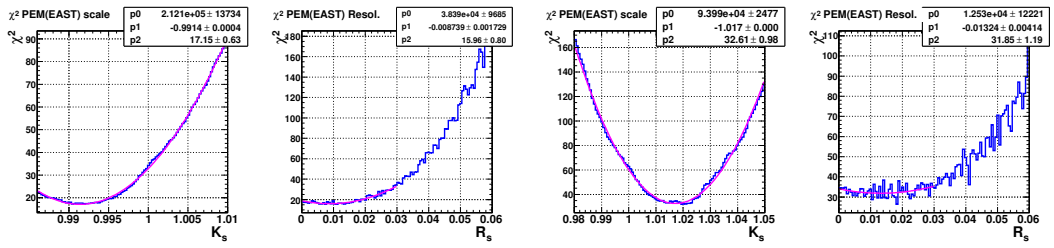

(a) $1.2 < \eta < 1.6$ (b) $1.6 < \eta < 2.8$

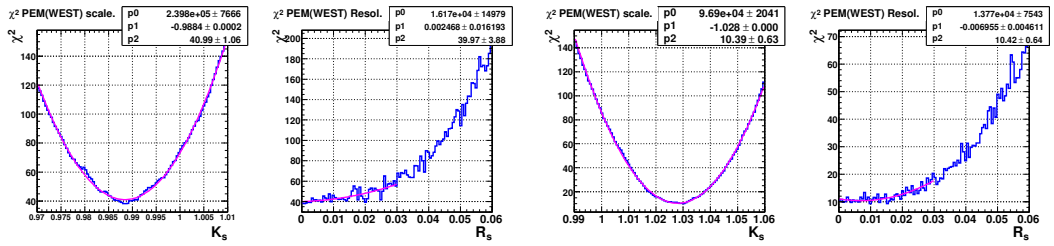

(c) $-1.6 < \eta < -1.2$ (d) $-2.8 < \eta < -1.6$

Figure 6.5: Forward electrons for GEN5: The best χ^2 fit of the $Z \rightarrow e^+e^-$ invariant mass comparison between data and MC for the cluster E_T energy scale. The fit formula is $p0(x + p1)^2 + p2$.

.

Region	$K_s \pm 1\sigma$	$R_s \pm 1\sigma$
$\|\eta\| < 1.2$	0.9941 ± 0.0005	-
$1.2 < \eta < 1.6$	0.9914 ± 0.0022	0.0087 ± 0.0051
$1.6 < \eta < 2.8$	1.0171 ± 0.0021	0.0132 ± 0.0044
$-1.6 < \eta < -1.2$	0.9884 ± 0.0020	0.0000 ± 0.0054
$-2.8 < \eta < -1.6$	1.0280 ± 0.0032	0.0070 ± 0.0085

Table 6.1: The cluster E_T scaling and resolution factors (GEN5).

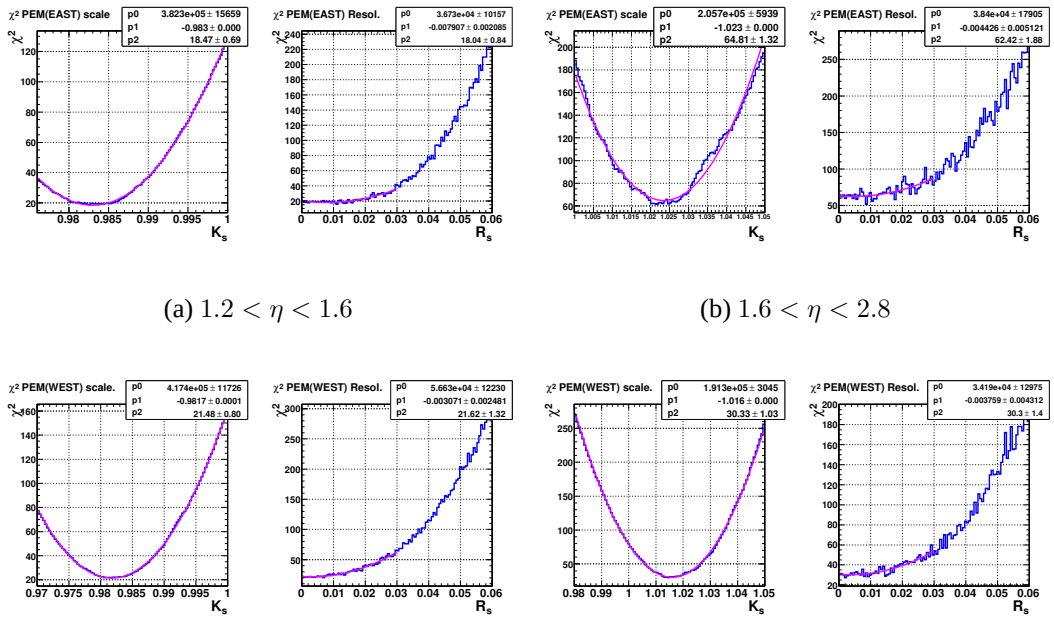

(a) $1.2 < \eta < 1.6$ (b) $1.6 < \eta < 2.8$

(c) $-1.6 < \eta < -1.2$ (d) $-2.8 < \eta < -1.6$

Figure 6.6: Forward electrons for GEN6: The best χ^2 fit of the $Z \rightarrow e^+e^-$ invariant mass comparison between data and MC for the cluster E_T energy scale. The fit formula is $p0(x + p1)^2 + p2$.

.

Region	$K_s \pm 1\sigma$	$R_s \pm 1\sigma$
$\|\eta\| < 1.2$	0.9907 ± 0.0004	-
$1.2 < \eta < 1.6$	0.9830 ± 0.0016	0.0079 ± 0.0052
$1.6 < \eta < 2.8$	1.0235 ± 0.0022	0.0044 ± 0.0051
$-1.6 < \eta < -1.2$	0.9817 ± 0.0015	0.0031 ± 0.0042
$-2.8 < \eta < -1.6$	1.0160 ± 0.0023	0.0038 ± 0.0054

Table 6.2: The cluster E_T scaling and resolution factors (GEN6).

Monte Carlo and the data. Since these aspects of the calorimeter energy measurement play important roles in determining the $\not\!\!E_T$, the Monte Carlo model for calorimeter deposition in $W \rightarrow e\nu$ events should be tuned to provide the best possible match with data. Using the $W \rightarrow e\nu$ samples, the recoil energy scale is determined for the Monte Carlo model.

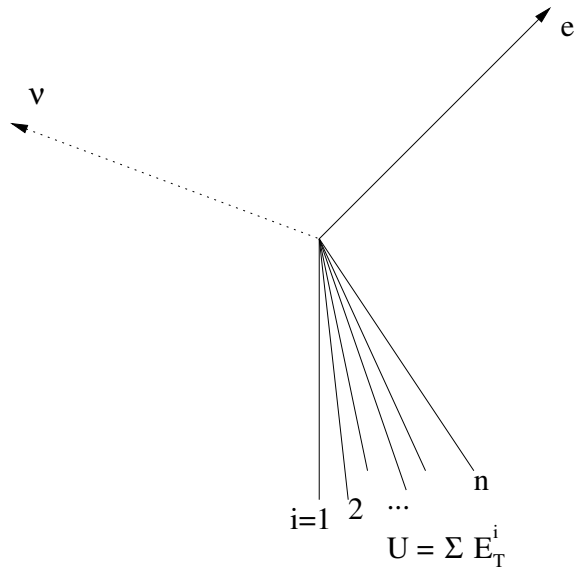

Figure 6.7: Kinematics of W boson production and decay, as viewed in the transverse plane to the proton-antiproton beams.

We define the recoil energy of an event in the directions parallel and perpendicular to the direction of the high p_T lepton from the W boson decay in the transverse plane of the detector as shown in Figure 6.7. These components of the recoil energy are:

$$\begin{aligned} U_x &= -\not\!\!E_{Tx} - (E_T^{EM} + E_T^{HAD})cos(\phi_e) \\ U_y &= -\not\!\!E_{Ty} - (E_T^{EM} + E_T^{HAD})sin(\phi_e) \\ U_{||} &= U_x cos(\phi_e) + U_y sin(\phi_e) \\ U_{\perp} &= U_x sin(\phi_e) - U_y cos(\phi_e) \end{aligned} \tag{6.2}$$

The appropriate corrections to apply to the MC recoil energy model are an overall scale correction for both the parallel and perpendicular directions and an additional constant term (shift correction). The scaling correction accounts for potential problems in modeling calorimeter response and the effects of multiple interactions, the underlying event model, and accelerator backgrounds which should not be dependent on the lepton direction. The shift correction is designed to account for modeling effects that do have a lepton-direction dependence such as the W boson recoil model and the model for lepton energy deposition in the calorimeter.

The MC recoil energy distributions to match those seen in data by corrections of the form:

$$\begin{aligned} (U_{||})' &= (K_{||} \times U_{||}) + C_{||} \\ (U_{\perp})' &= (K_{\perp} \times U_{\perp}) + C_{\perp} \end{aligned} \tag{6.3}$$

In order to determine the best values for the scaling and shifting constants in these formulas, χ^2 fits between the data recoil energy distributions and corrected MC distributions for a range of scaling and shifting constants are performed. An iterative process is used in which we first determine the best possible shifting constants and then fit for scaling constants based on those values. This process repeats until the χ^2 fits for both the scaling and shifting constants stablilze at set values. The results of the χ^2 fits used to obtain the central values and uncertainties for the tuning parameters defined in Eq. 6.3 are shown in Table 6.4 and as a function of electron η in Figure 6.19. Figure 6.8 - 6.13 show the results of the final χ^2 fits for the recoil energy corrections in the parallel and perpendicular directions and a comparison of the tuned Monte Carlo recoil energy distributions with those obtained from the data are shown in Figure 6.14 - 6.18.

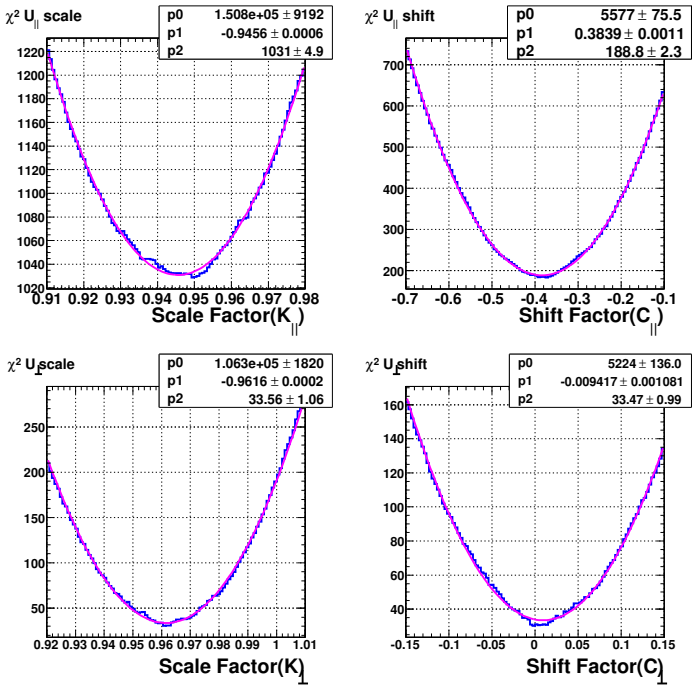

Figure 6.8: Central electron fiducial region (GEN5): The best χ^2 fit of the recoil energy comparison between data and MC for central electrons. The fit formula is $p0(x + p1)^2 + p2$.

.

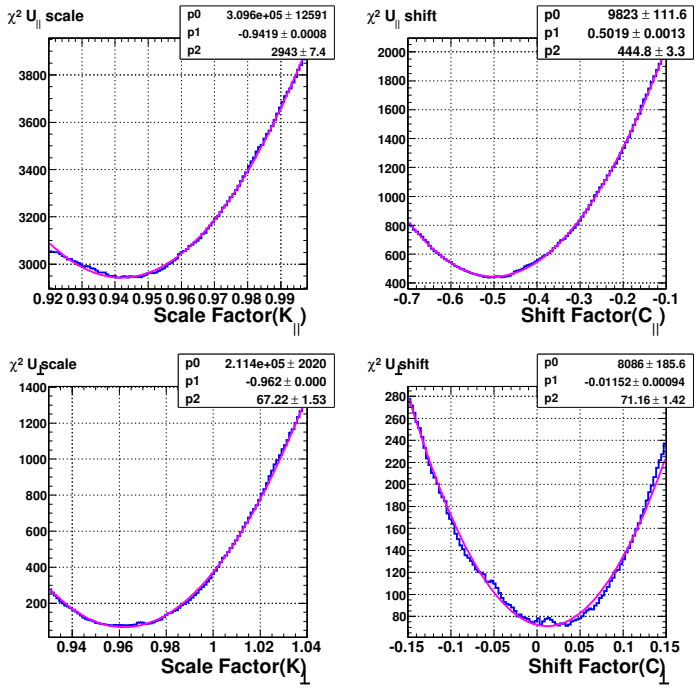

Figure 6.9: Central electron fiducial region (GEN6): The best χ^2 fit of the recoil energy comparison between data and MC for central electrons. The fit formula is $p0(x + p1)^2 + p2$.

.

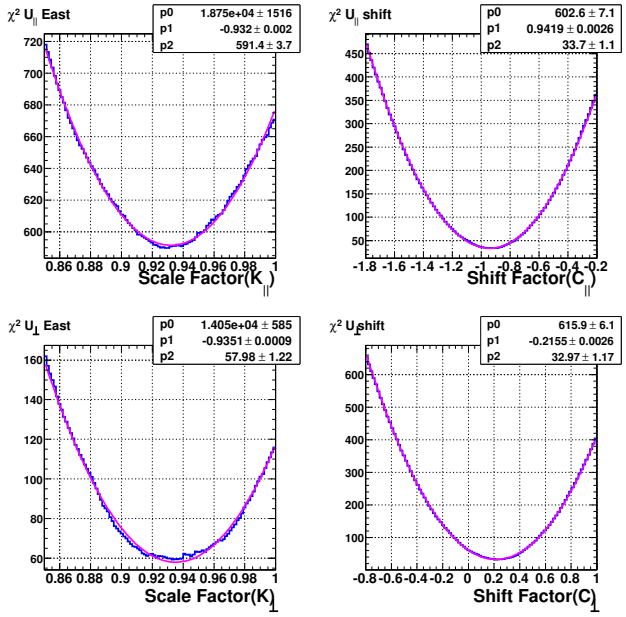

(a) $1.2 < \eta < 1.6$

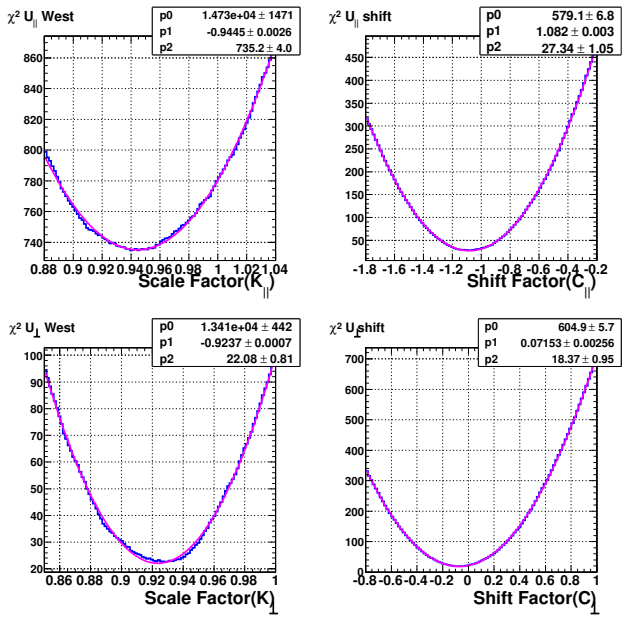

(b) $-1.6 < \eta < -1.2$

Figure 6.10: GEN5 MC foward electron region: The best χ^2 fit of the recoil energy comparison between data and MC for foward electrons with COT tracks. The fit formula is $p0(x + p1)^2 + p2$.

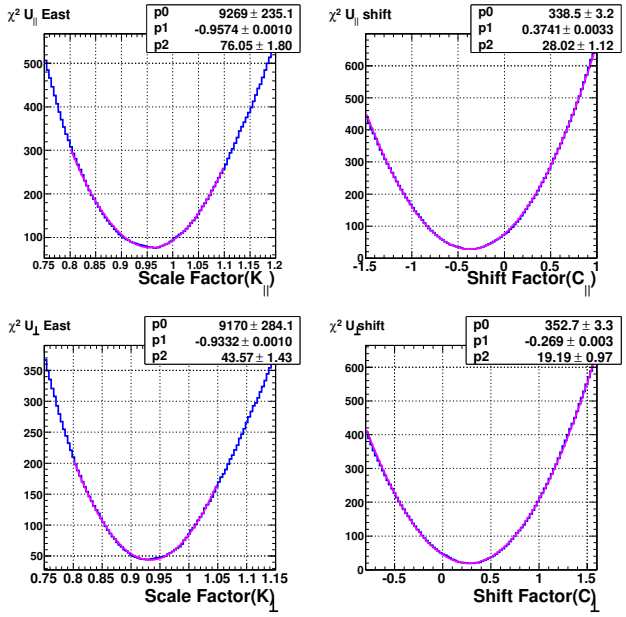

(a) $1.6 < \eta < 2.8$

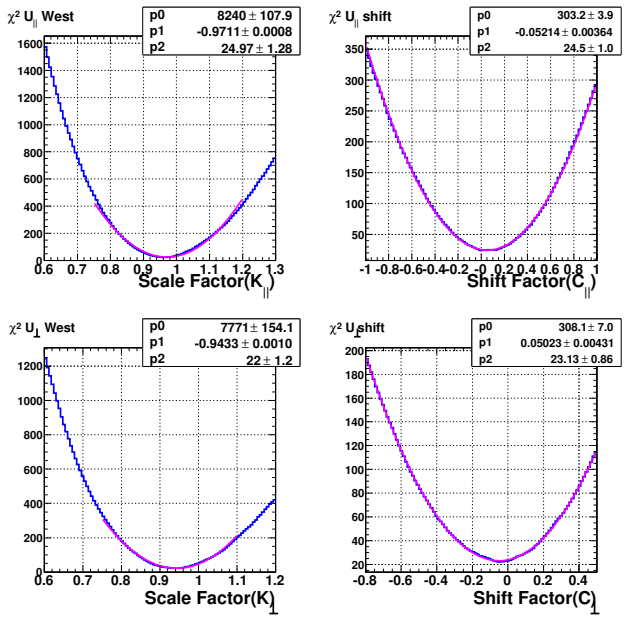

(b) $-2.8 < \eta < -1.6$

Figure 6.11: GEN5 MC foward electron region: The best χ^2 fit of the recoil energy comparison between data and MC for foward electrons with SISA tracks. The fit formula is $p0(x + p1)^2 \ + \ p2$.

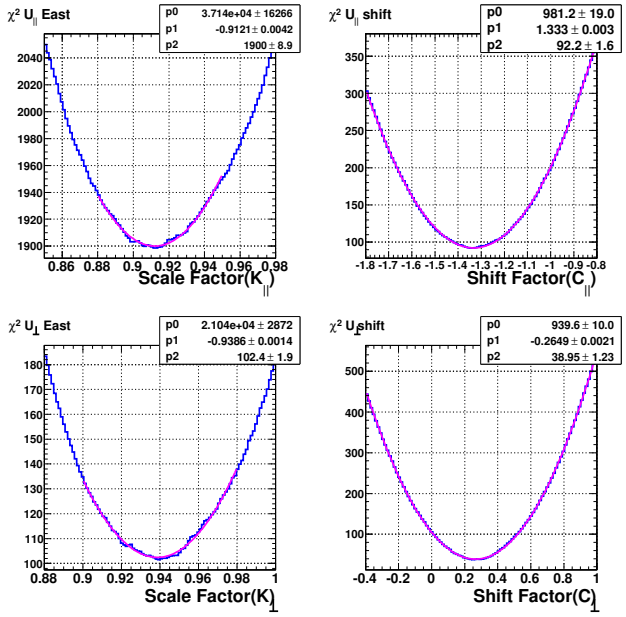

(a) $1.2 < \eta < 1.6$

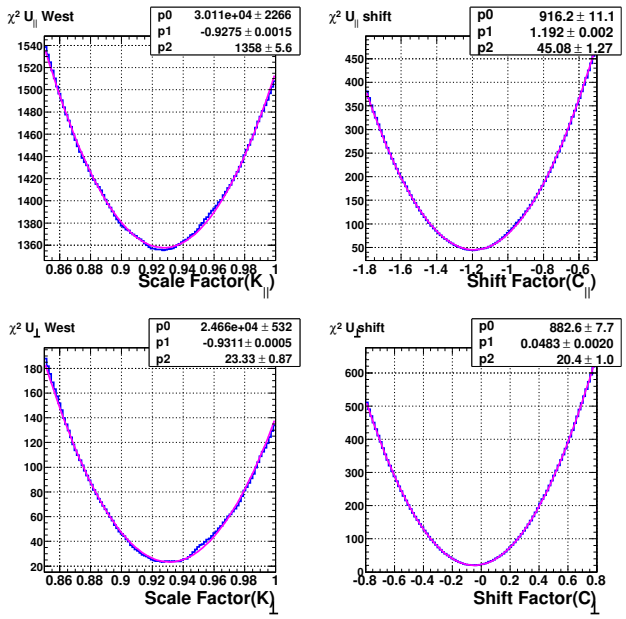

(b) $-1.6 < \eta < -1.2$

Figure 6.12: GEN6 MC foward electron region: The best χ^2 fit of the recoil energy comparison between data and MC for foward electrons with COT tracks. The fit formula is $p0(x + p1)^2 \ + \ p2$.

.

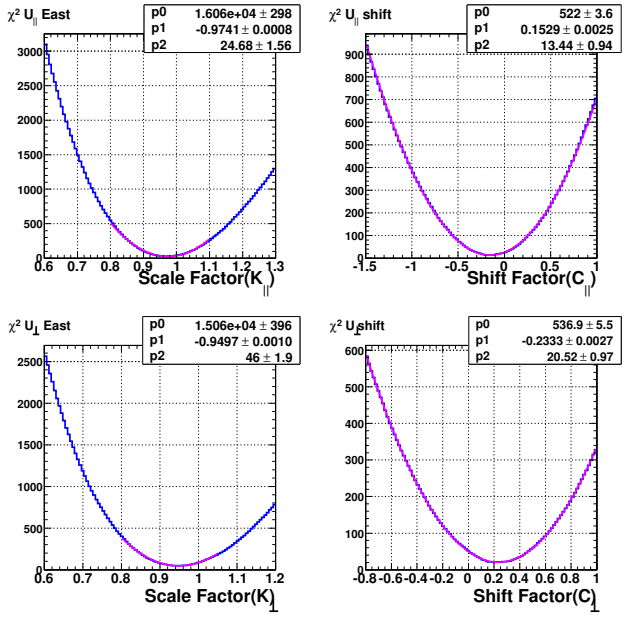

(a) $1.6 < \eta < 2.8$

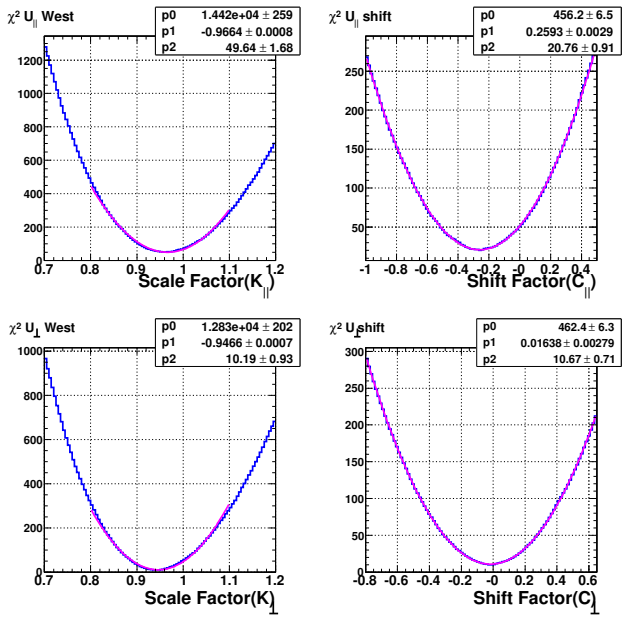

(b) $-2.8 < \eta < -1.6$

Figure 6.13: GEN6 MC foward electron region: The best χ^2 fit of the recoil energy comparison between data and MC for foward electrons with SISA tracks. The fit formula is $p0(x + p1)^2 \ + \ p2$.

.

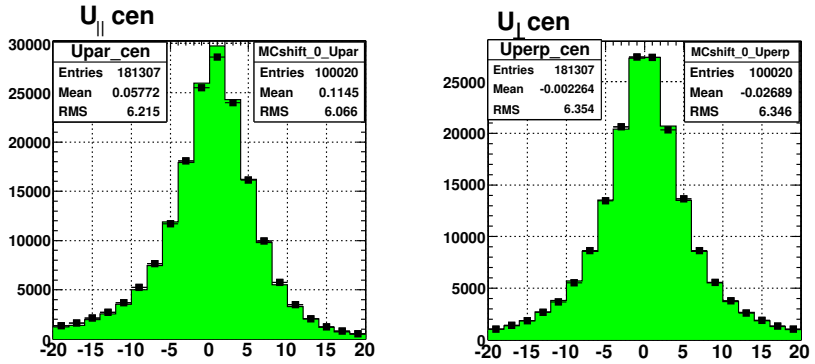

(a) GEN5 MC

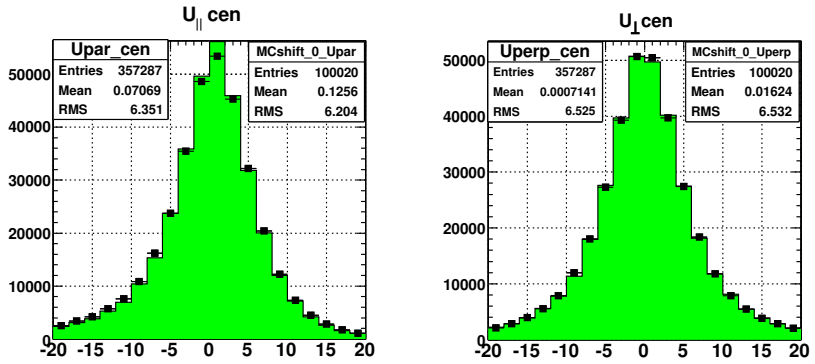

(b) GEN6 MC

Figure 6.14: Central electron fiducial region: The recoil energy distributions after the MC is tuned.

.

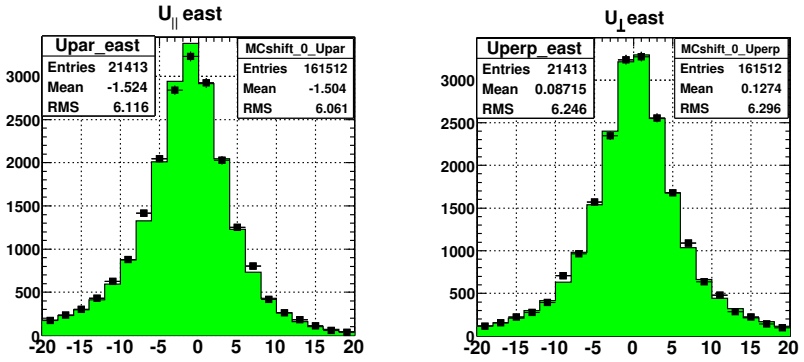

(a) $1.2 < \eta < 1.6$

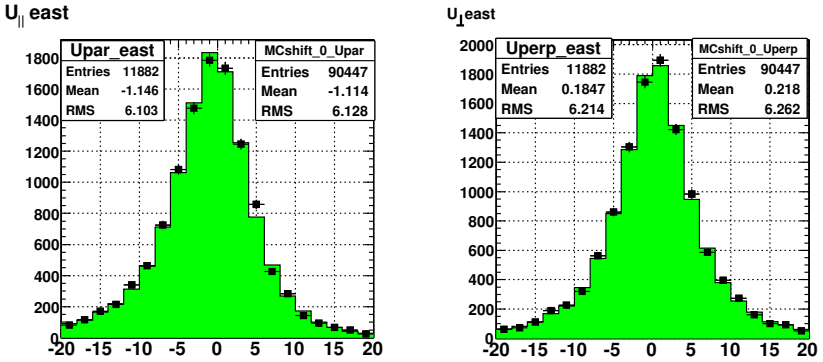

(b) $1.6 < \eta < 2.8$

Figure 6.15: GEN5 MC forward electron region ($\eta > 1.2$): The comparison of recoil energy between data and MC. We applied the cluster E_T scale, resolution and recoil energy scale factors to MC sample.

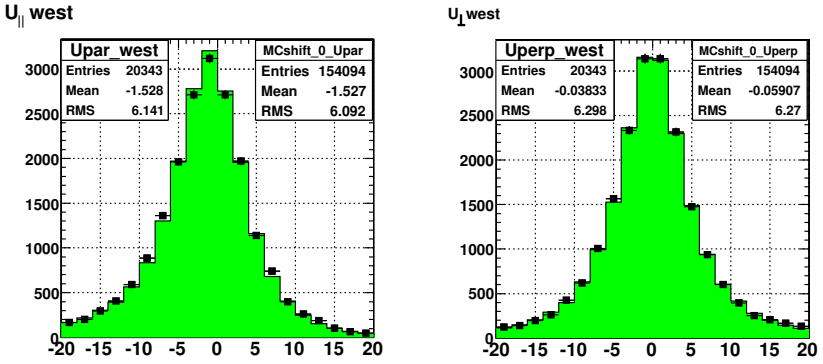

(a) $-1.6 < \eta < -1.2$

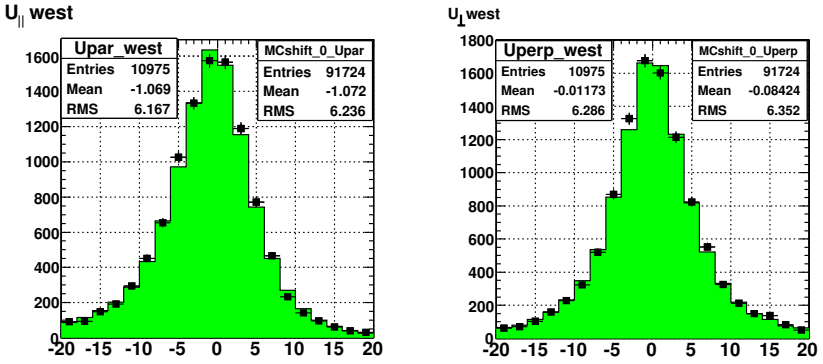

(b) $-2.8 < \eta < -1.6$

Figure 6.16: GEN5 MC forward electron region ($\eta < -1.2$): The comparison of recoil energy between data and MC. We applied the cluster E_T scale, resolution and recoil energy scale factors to MC sample.

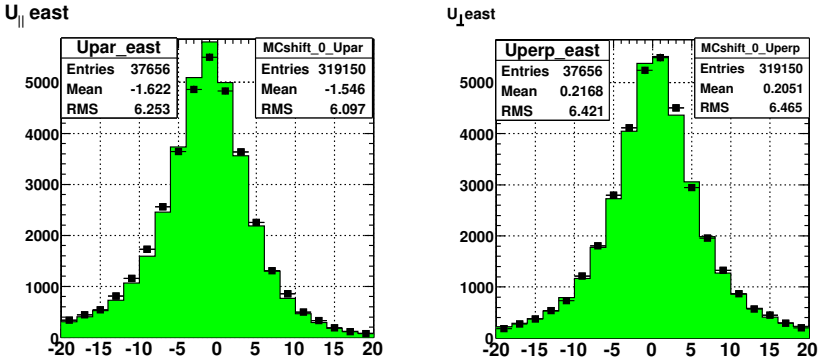

(a) $1.2 < \eta < 1.6$

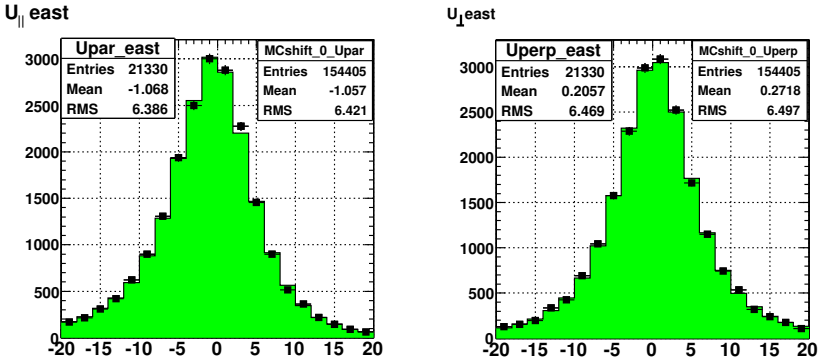

(b) $1.6 < \eta < 2.8$

Figure 6.17: GEN6 MC forward electron region ($\eta > 1.2$): The comparison of recoil energy between data and MC. We applied the cluster E_T scale, resolution and recoil energy scale factors to MC sample.

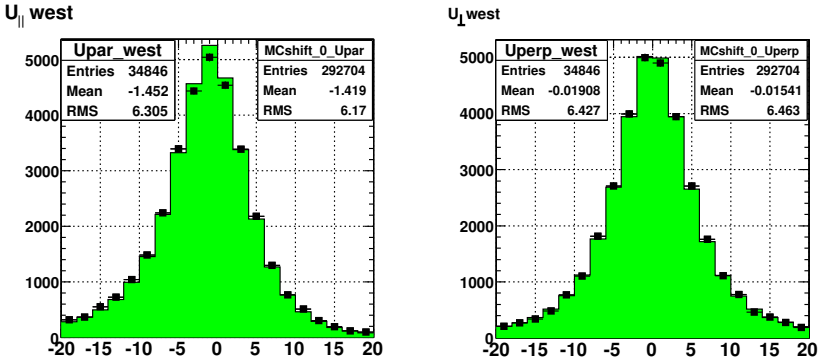

(a) $-1.6 < \eta < -1.2$

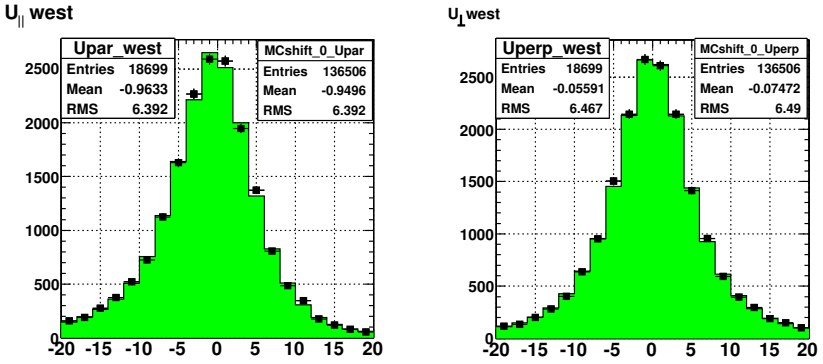

(b) $-2.8 < \eta < -1.6$

Figure 6.18: GEN6 MC forward electron region ($\eta < -1.2$): The comparison of recoil energy between data and MC. We applied the cluster E_T scale, resolution and recoil energy scale factors to MC sample.

$U_{\|\|}$	$K_{\|\|} \pm 1\sigma$	$C_{\|\|} \pm 1\sigma$
$\|\eta\| < 1.2$	0.9726 $\pm$ 0.0031	-0.3760 $\pm$ 0.0136
$1.2 < \eta < 1.6$	0.9635 $\pm$ 0.0096	-0.8461 $\pm$ 0.0405
$1.6 < \eta < 2.8$	0.9482 $\pm$ 0.0120	-0.3371 $\pm$ 0.0557
$-1.6 < \eta < -1.2$	0.9759 $\pm$ 0.0100	-1.0146 $\pm$ 0.0426
$-2.8 < \eta < -1.6$	0.9619 $\pm$ 0.0126	0.0675 $\pm$ 0.0613
$U_{\perp}$	$K_{\perp} \pm 1\sigma$	$C_{\perp} \pm 1\sigma$
$\|\eta\| < 1.2$	0.9645 $\pm$ 0.0036	0.0008 $\pm$ 0.0142
$1.2 < \eta < 1.6$	0.9368 $\pm$ 0.0098	0.1870 $\pm$ 0.0414
$1.6 < \eta < 2.8$	0.9335 $\pm$ 0.0127	0.1963 $\pm$ 0.0563
$-1.6 < \eta < -1.2$	0.9424 $\pm$ 0.0102	-0.0664 $\pm$ 0.0426
$-2.8 < \eta < -1.6$	0.9394 $\pm$ 0.0142	-0.0575 $\pm$ 0.0568

Table 6.3: The recoil energy scaling factors (GEN5).

$U_{\|\|}$	$K_{\|\|} \pm 1\sigma$	$C_{\|\|} \pm 1\sigma$
$\|\eta\| < 1.2$	0.9751 $\pm$ 0.0022	-0.4646 $\pm$ 0.0104
$1.2 < \eta < 1.6$	0.9587 $\pm$ 0.0070	-1.1924 $\pm$ 0.0320
$1.6 < \eta < 2.8$	0.9687 $\pm$ 0.0095	-0.1519 $\pm$ 0.0450
$-1.6 < \eta < -1.2$	0.9567 $\pm$ 0.0073	-1.0944 $\pm$ 0.0336
$-2.8 < \eta < -1.6$	0.9554 $\pm$ 0.0098	-0.2037 $\pm$ 0.0477
$U_{\perp}$	$K_{\perp} \pm 1\sigma$	$C_{\perp} \pm 1\sigma$
$\|\eta\| < 1.2$	0.9724 $\pm$ 0.0024	0.0192 $\pm$ 0.0110
$1.2 < \eta < 1.6$	0.9434 $\pm$ 0.0077	0.2526 $\pm$ 0.0330
$1.6 < \eta < 2.8$	0.9448 $\pm$ 0.0098	0.2253 $\pm$ 0.0443
$-1.6 < \eta < -1.2$	0.9309 $\pm$ 0.0076	-0.0448 $\pm$ 0.0338
$-2.8 < \eta < -1.6$	0.9380 $\pm$ 0.0103	-0.0009 $\pm$ 0.0469

Table 6.4: The recoil energy scaling factors (GEN6).

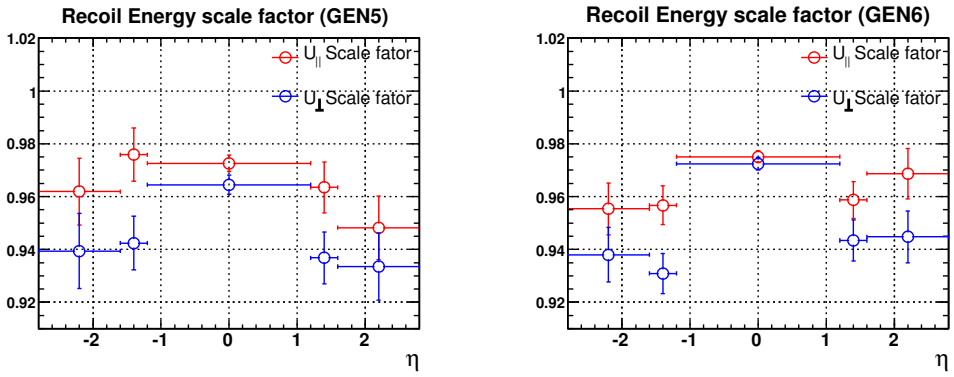

Figure 6.19: Recoil Energy Scale Factors as a function of η_e.

6.3 Charge Identification

Good charge identification is crucial for the asymmetry measurement because the charge determines the sign of the weight factor, $w^{\pm}$ (see Eqn. 5.6), which determines the number of $W^{\pm}$ rapidity events. Therefore, charge misidentification of electrons changes the W charge asymmetry and the charge misidentification rate needs to be properly determined. The charge fake rate (CFR) of an electron is measured using the $Z \rightarrow e^+e^-$ samples and is defined as:

$$f_{mis}(\eta) = \frac{N_{wrong-sign}(\eta)}{N_{right-sign}(\eta) + N_{wrong-sign}(\eta)}, \tag{6.4}$$

where $N_{wrong-sign}$ is the number of Z candidates where two electrons have the same sign, and $N_{right-sign}$ is the number where they have the opposite sign. In order to study this charge misidentification, Z candidates from the high-p_T electron dataset are used. This is a good sample since $Z \rightarrow e^+e^-$ events have very low backgrounds, the electrons have similar kinematics to the $W \rightarrow e\nu$ events, and the events self-identify as correct or incorrect charge measurements by comparing the same to opposite sign dielectron

events. Z data sample is compared to a Monte Carlo sample to determine any difference in charge misidentification between the data and the simulation.

For central-central Zs, two electrons are required with one passing the tight electron cuts used for the $W \rightarrow e\nu$ sample in Table 3.1, but other electrons must pass extra tight cuts: isolation ratio $<$ 0.05 and the lateral shower quality(L_{shr}) $<$ 0.1. For central-forward Zs, the central electron is selected with the same extra tight cuts, and the forward electron must pass the PEM and default track requirements in Table 3.2. For all candidates, the dielectron invariant mass is also required to be between 76 and 106 GeV/c^2 for central-central Zs and between 81 and 101 GeV/c^2 for central-forward Zs. The background contribution (0.48%) from jets in Z data is subtracted for the central-forward Zs; the background estimate is described in section 4.2.1. The charge fake rate from the selected Z candidates is measured as a function of η_d. Figure 6.20 shows that the CFRs of two different run-periods data (run 138425 - 186598 : 0d and run 190697 - 212133 : 0h+0i) are consistent but the CFR of GEN6 MC is higher than one of GEN5 MC at $|\eta_d| > 1.6$. Thus, GEN5 and GEN6 simulation charge fake rates are tuned to the corresponding data. The CFR of the MC is tuned by scale factors which are determined from the best χ^2 value between data and MC for four η_d regions of the electron listed in Table 6.5.

In order to have a charge mis-identification correction for our asymmetry, we need

Region	GEN5 MC $K_s \pm 1\sigma$	GEN6 MC $K_s \pm 1\sigma$
$-2.8 > \eta > -1.6$	1.7 ± 0.2	1.0 ± 0.1
$-1.6 > \eta > -1.1$	0.5 ± 0.2	0.5 ± 0.2
$1.1 > \eta > 1.6$	0.3 ± 0.1	0.3 ± 0.2
$1.6 < \eta < 2.8$	1.5 ± 0.2	0.8 ± 0.1

Table 6.5: Charge Fake Rate Scale factors.

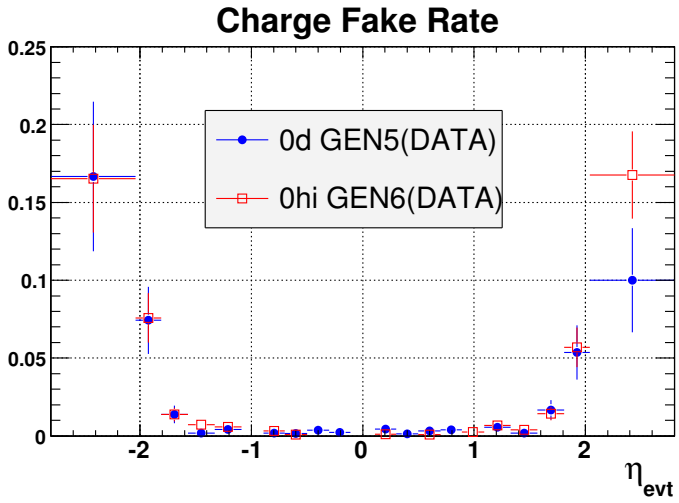

(a) The consistency of CFRs for both 0d and 0h+0i dataset

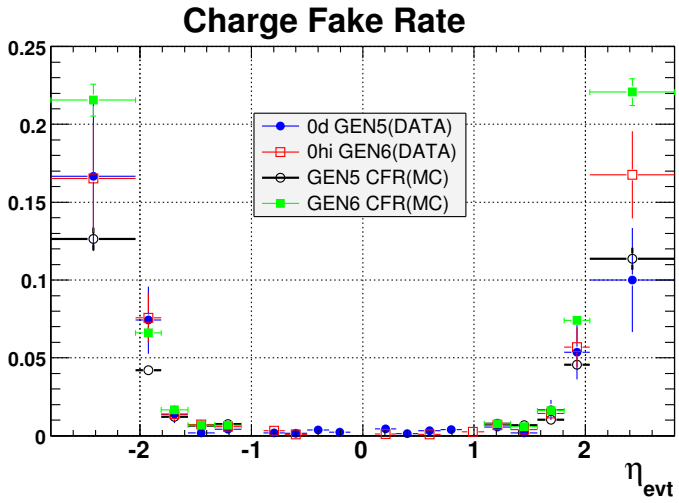

(b) The comparison of CFR between data and MCs

Figure 6.20: The charge fake rate is plotted as a function of electron η.

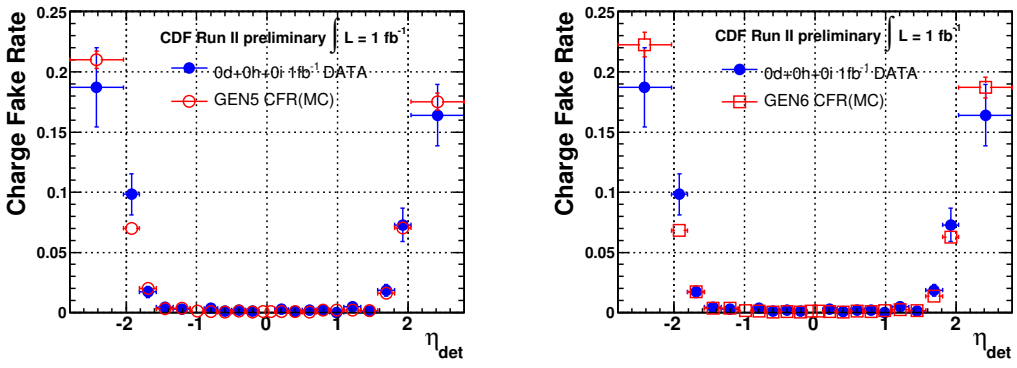

Figure 6.21: Charge Fake Rates for data and GEN5 MC (left) and GEN6 MC (right). We applied the scale factors to the MC samples.

to describe the charge fake rate as a function of W rapidity. Thus, we derive a correction of charge fake rate such that it can be put into the acceptance correction from the charge fake rate vs. η in Figure 6.21. The total reconstructed number of positively and negatively charged events and the total number of true charged events are described in Eq. 6.5 and 6.6, respectively.

$$\begin{aligned} N^{+}_{obs}(w^{+}) &= N^{+}_{+}(w^{+}) + N^{-}_{+}(w^{+}) \\ N^{-}_{obs}(w^{-}) &= N^{-}_{-}(w^{-}) + N^{+}_{-}(w^{-}) \end{aligned} \tag{6.5}$$

$$\begin{aligned} N^{+}_{true} &= N^{+}_{+}(w^{+}) + N^{+}_{-}(w^{+}) \\ N^{-}_{true} &= N^{-}_{-}(w^{-}) + N^{-}_{+}(w^{-}) \end{aligned} \tag{6.6}$$

$N^{+}_{-}(w^{+})$ is the number of truly positive (superscript) events reconstructed with a negative (subscript) charge. This is a function of the weight factor (w) associated with the true (superscript) charge in that bin of W rapidity, where the charge dependence of the

weight factor must be carefully handled. The number of true charged events is alternatively described with the reconstructed information as

$$\begin{aligned} N^{+}_{true} &= \left[N^{+}_{+}(w^{+}) + N^{-}_{+}(w^{+})\right] \times \frac{N^{+}_{+}(w^{+})}{\left[N^{+}_{+}(w^{+}) + N^{-}_{+}(w^{+})\right]} \\ &\quad + \left[N^{-}_{-}(w^{+}) + N^{+}_{-}(w^{+})\right] \times \frac{N^{+}_{-}(w^{+})}{\left[N^{-}_{-}(w^{+}) + N^{+}_{-}(w^{+})\right]} \\ &= N^{+}_{obs}(w^{+}) \times \left(1 - \rho^{+}(w^{+})\right) + N^{-}_{obs}(w^{+}) \times \left(\rho^{-}(w^{+})\right) \qquad (6.7) \\ N^{-}_{true} &= \left[N^{-}_{-}(w^{-}) + N^{+}_{-}(w^{-})\right] \times \frac{N^{-}_{-}(w^{-})}{\left[N^{-}_{-}(w^{-}) + N^{+}_{-}(w^{-})\right]} \\ &\quad + \left[N^{+}_{+}(w^{-}) + N^{-}_{+}(w^{-})\right] \times \frac{N^{-}_{+}(w^{-})}{\left[N^{+}_{+}(w^{-}) + N^{-}_{+}(w^{-})\right]} \\ &= N^{-}_{obs}(w^{-}) \times \left(1 - \rho^{-}(w^{-})\right) + N^{+}_{obs}(w^{-}) \times \left(\rho^{+}(w^{-})\right) \qquad (6.8) \end{aligned}$$

In Eq. 6.9, the four charge fake rates, that are $\rho^{+}(w^{+})$, $\rho^{+}(w^{-})$, $\rho^{-}(w^{-})$ and $\rho^{-}(w^{+})$ in Eq. 6.7 and 6.8, are defined as the reconstructed charge and the weight factors of the two W rapidity solutions.

$$\begin{aligned} \rho^{+}(w^{+}) &= \frac{N^{-}_{+}(w^{+})}{N^{+}_{+}(w^{+}) + N^{-}_{+}(w^{+})} \\ \rho^{+}(w^{-}) &= \frac{N^{-}_{+}(w^{-})}{N^{+}_{+}(w^{-}) + N^{-}_{+}(w^{-})} \\ \rho^{-}(w^{-}) &= \frac{N^{+}_{-}(w^{-})}{N^{-}_{-}(w^{-}) + N^{+}_{-}(w^{-})} \\ \rho^{-}(w^{+}) &= \frac{N^{+}_{-}(w^{+})}{N^{-}_{-}(w^{+}) + N^{+}_{-}(w^{+})} \qquad (6.9) \end{aligned}$$

6.4 Backgrounds

The corrections for two backgrounds are used for this analysis: QCD and $Z \to e^{+}e^{-}$. Recall that we consider the $W \to \tau\nu \to e\nu$ as signal since it has the same W production

charge asymmetry and that it is included in the acceptance. The estimates of these backgrounds are described in the Chapter 4. For the $Z \rightarrow e^+e^-$ and $W \rightarrow \tau\nu$ contributions, we rely on Monte Carlo simulation and the contributions are shown in Figure 4.1.

6.4.1 Jet-like-electron sample

In order to estimate the QCD jet contribution in the measured W rapidity, the QCD fake W rapidity should be reconstructed using our analysis technique and it can be done with a jet sample plus require large $\not\!\!E_T$. Since the dijet sample in Section 4.2.2 has been restricted in $\not\!\!E_T < 10$ GeV, An alternative approach is used to extract the QCD background in y_W bins for the W charge asymmetry measurement. The approach defines QCD electron-fake sample using the same dataset and trigger path as is used to form the W candidate sample, but the fake electron are selected by requiring an electron cluster which passes all baseline selection cuts in Table 3.1 and 3.2 but fail the Had/Em and isolation cut. An electron which meets this criteria is referred to as an "jet-like-electron". A jet-like-electron sample excludes any other tight electron and low $\not\!\!E_T$ ($<$ 25 GeV) events.

This sample contains some signal contamination, which can be estimated by fitting the isolation distribution and must be subtracted from the sample. As was discussed in Section 4.2, the isolation shape of the jet-like-electron data is fitted to estimate the signal contribution using the electron and jet templates. However, since $Z \rightarrow e^+e^-$ data with the veto cuts has limited statistics for this purpose, the electron template for this fit is obtained from $W \rightarrow e\nu$ MC instead. The results for the different $\not\!\!E_T$ regions are presented in Figure 6.22. We estimate the electron fraction in the central and non-isolated (< 6 GeV) jet-like-electron sample to be $(0.5 \pm 1.3_{\rm stat})$ % for 25 GeV $< \not\!\!E_T <$ 35 GeV and $(3.0 \pm 1.7_{\rm stat})$ % for $\not\!\!E_T >$ 35 GeV and in the forward the electron contributions are very small quantity, for example, the electron fraction is $(0.0 \pm 1.8_{\rm stat})$ % for 25 GeV

$< \not\!\!E_T < 35$ GeV and $(0.2 \pm 2.2_{\rm stat})$ % for $\not\!\!E_T > 35$ GeV.

6.4.2 QCD contribution on the W rapidity

The QCD fake W rapidity is reconstructed using the jet-like-electron plus $\not\!\!E_T$ sample and then the electron contribution is subtracted as just discussed. Figure 6.23 shows the fake W rapidity constructed in this matter with the same weight factors and reconstruction algorithm applied to the signal sample. The QCD and $Z \rightarrow e^+e^-$ backgrounds as a function of rapidity and charge are then subtracted from the W samples as a function of reconstructed rapidity.

6.5 Trigger Efficiencies

The trigger efficiency is the probablility that a $W \rightarrow e\nu$ signal event meeting the kinematic cuts is accepted by the trigger. The efficiency for an event to pass the trigger requirement is measured in other samples containing the object selected by the trigger but not biased by the analysis trigger requirements. Using trigger paths parallel to the analysis path, the trigger response is determined in the offline from correctly reconstructed objects searched for in the triggers. The efficiency of each trigger is measured separately for the L1, L2, and L3 efficiencies and then the product of these is taken as the overall efficiency. The measured efficiency is then applied to the simulated signal sample to correct the predicted number of events.

For the central electron trigger efficiency, only the L1 tracking trigger efficiecny has an η dependence, which is what is relevent for this analysis. For electrons in the forward region, the L2 trigger has a dependence on η and E_T. The details this complicated measurement are discussed in Appendix A.

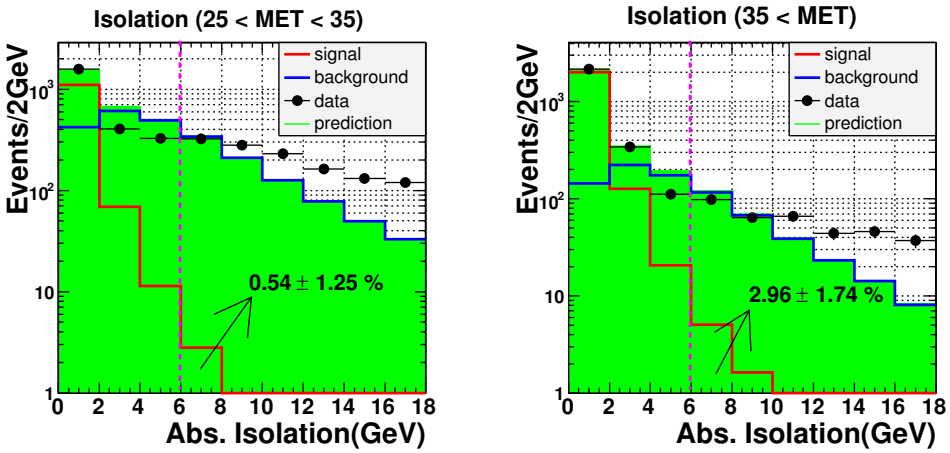

(a) Central Fiducial Region

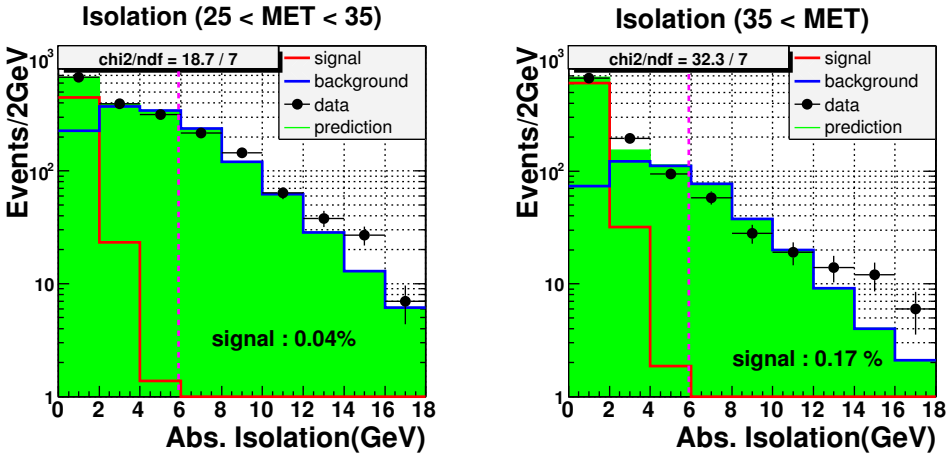

(b) Forward Fiducial Region

Figure 6.22: Isolation distribution fit of jet-like-electron data.

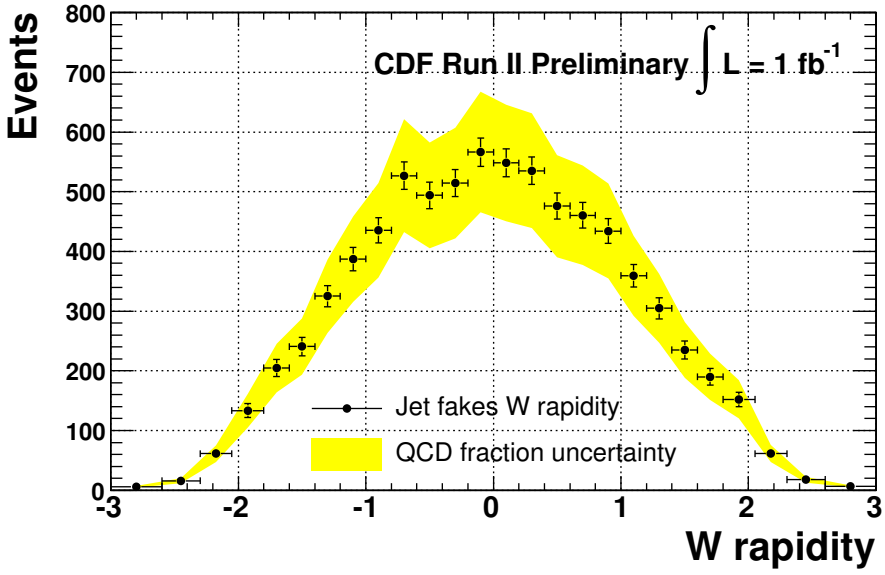

Figure 6.23: QCD Fake W rapidity distribution obtained from the jet-like plus $\not\!\!E_T$ sample.

6.6 Electron Identification Efficiencies

A systematic bias in the W charge asymmetry occurs if the electron identification cuts have any η or energy dependence or if the detector response to electrons differs from that of positrons. Separate from the electron indentification selection in the calorimeter, the tracking reconstruction efficiency is compared between the data and detector simulation.

6.6.1 Central Electron Identification efficiency

To measure the central electron identification efficiencies [39], the tight electron requirements of Table 3.1 are applied to one leg, the geometric and kinematic cuts of $E_T > 25$ GeV, $p_T > 10$ GeV and fiduciality are applied to the second leg, and opposite sign and tight invariant mass cuts are made (76 $\mathrm{GeV/c^2} < M_{ee} <$ 106 $\mathrm{GeV/c^2}$). Figure 6.24 shows that the central electron identification efficiencies have an η dependence and the data/MC scale factor of the ID efficiency has a few percent variation as a function of η. This correction is applied to $W \rightarrow e\nu$ acceptance in this analysis.

For the central electron tracking, the COT tracking reconstruction is measured using a W no-track sample. The efficiency that a high-p_T track is reconstructed for a central electron with $E_T > 25$ GeV is found to be 100 $\pm$ 0.4$\%$ in both the data and the simulation. Therefore, no correction is needed.

6.6.2 Forward Electron Identification efficiency

The forward electron identification efficiency is more straightforward to obtain than the central efficiencies as the selection of the central leg of central-forward events is independent of the forward leg used as the probe. However even more care must be taken over the backgrounds, which are greater. In addition to the forward electron selection, the track quality cuts are required for the forward electrons, as shown in Table 3.2. The

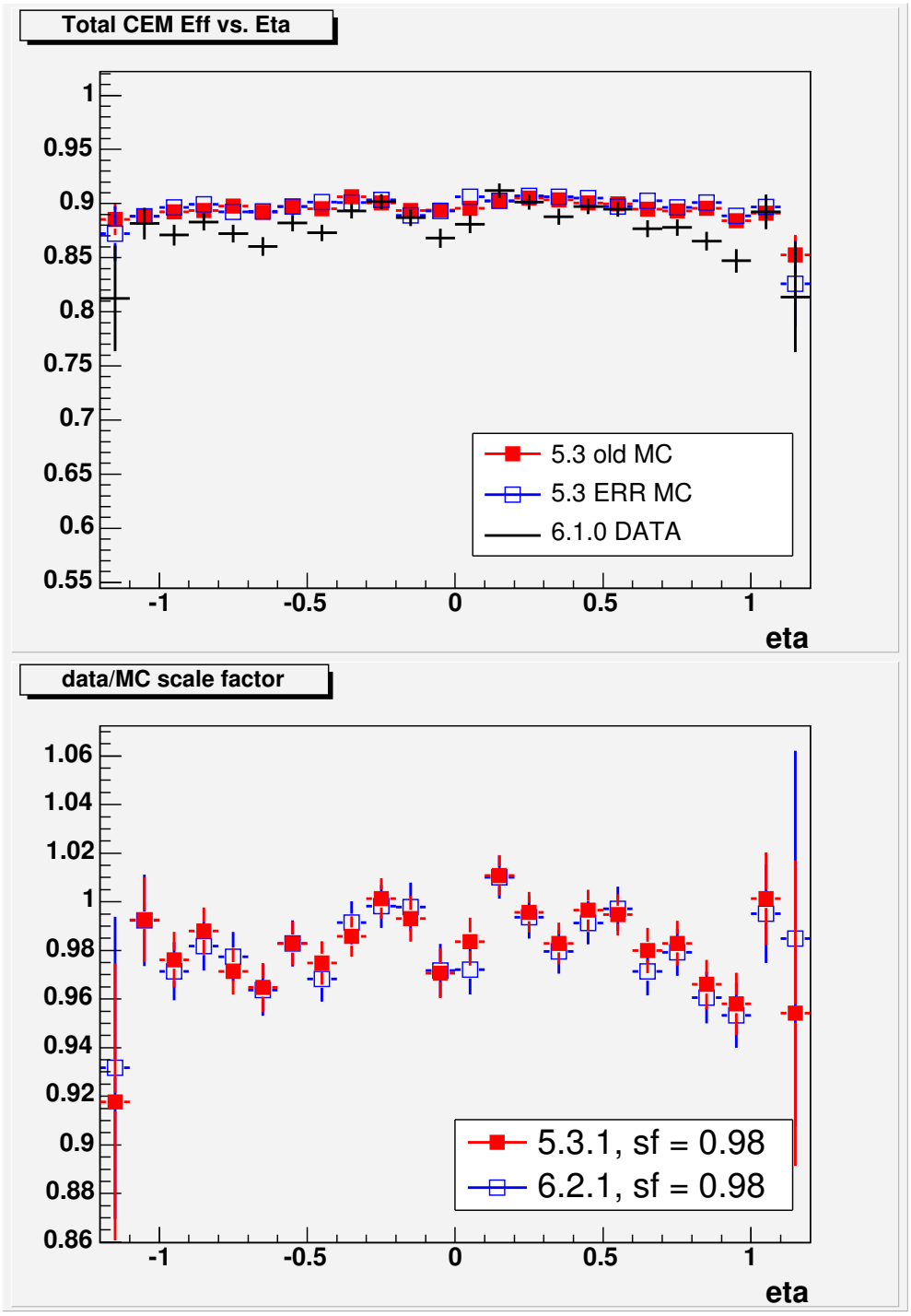

Figure 6.24: The central electron identification efficiency in $Z \rightarrow e^+e^-$ events as a function of η (top) and the scale factor of ratio data/MC (bottom).

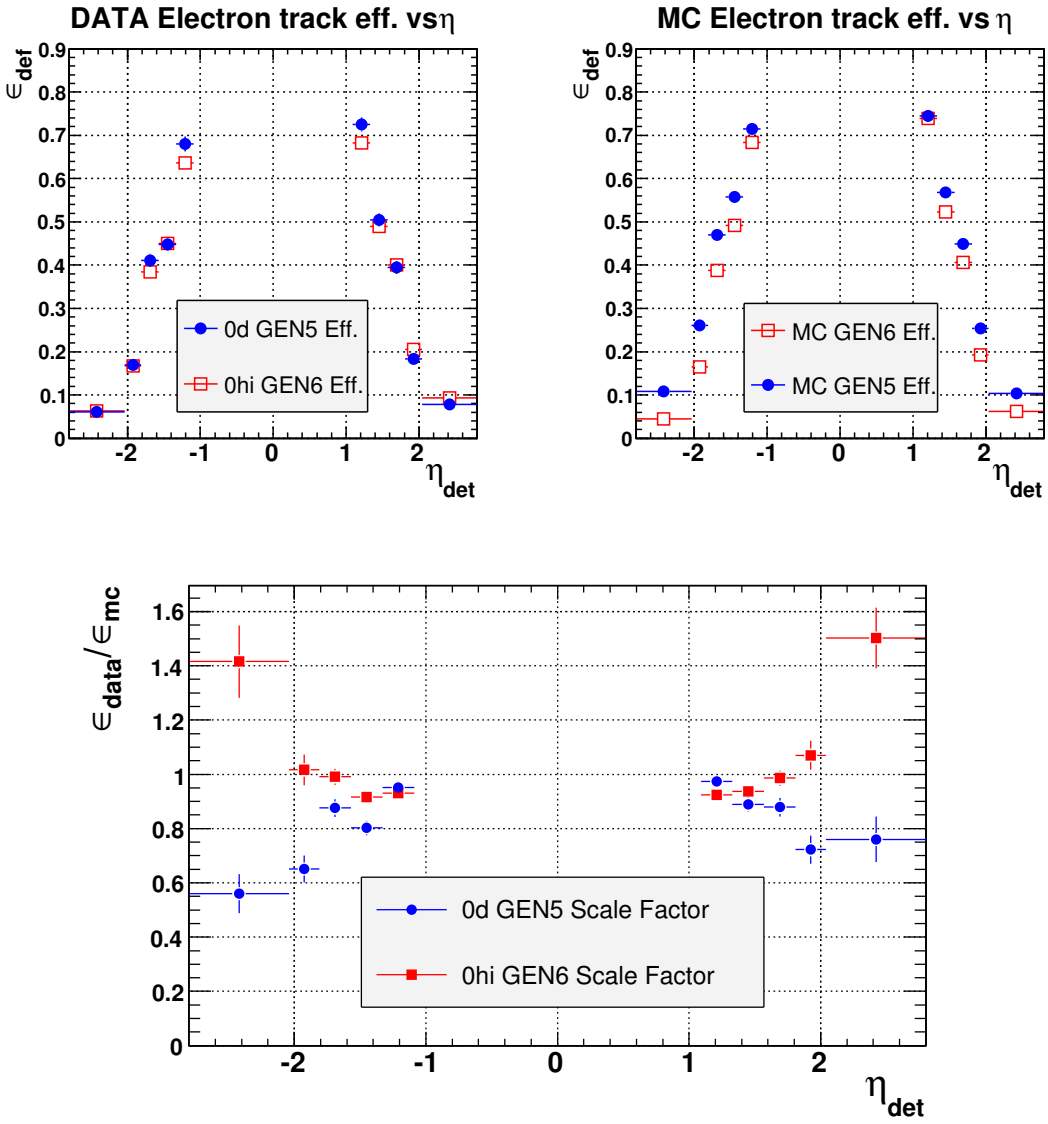

Figure 6.25: The tracking efficiency of the forward leg in $Z \rightarrow e^{+}e^{-}$ events as a function of η (top) and the scale factor of ratio data/MC (bottom).

efficiency scale factor of the track quality cuts in the forward using CF $Z \rightarrow e^{+}e^{-}$ events is measured, where the forward leg has only the PEM selection. To reduce backgrounds, one leg passes extra tight CEM cuts (Iso < 0.05 and Lshr < 0.1) and the invariant mass should be in the region 81 GeV $< M_{ee} <$ 101 GeV. To measure the efficiency vs. η in the data and the MC the track quality cuts on the PEM electron are applied to these events. A correction factor for the simulated data is calculated as the ratio of the two efficiencies.

However, as mentioned in section 3.5 the forward tracking efficiency of GEN5 MC is higher than GEN6 MC and this effect requires us to use two different electron tracking scale factors for both run-periods (0i and 0h+0i) as show in Figure 6.25. Figure 6.26 shows no charge dependence of the correction for the forward tracking efficiency.

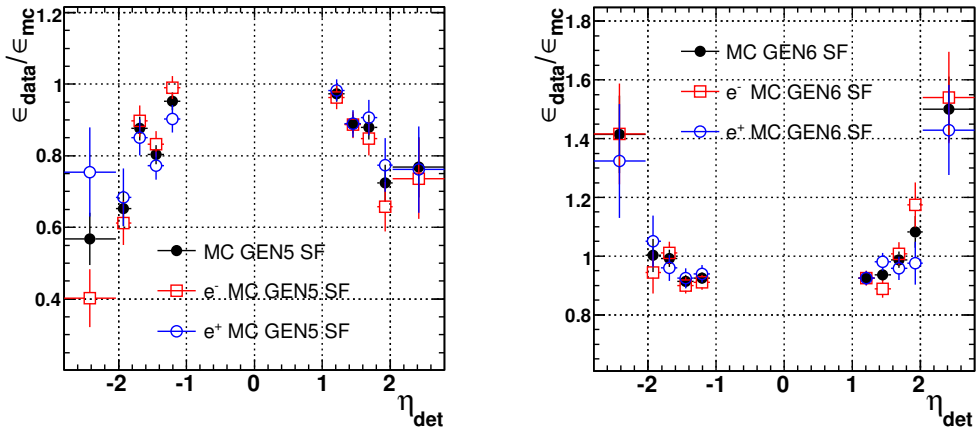

Figure 6.26: The scale factor of ratio data/MC (bottom) separately for positrons and electrons.

6.7 $W \rightarrow e\nu$ Acceptance

The raw W charge asymmetry must be corrected for detector acceptance and smearing effects to obtain the true W asymmetry, which can be compared to theoretical calculations. In order to address the smearing a response matrix is determined as

$$\begin{aligned} R_{ij}^{\pm} &= \frac{P(\text{ observed in bin } i \text{ and true value in bin } j\ )}{P(\text{ true value in bin } j\ )} \\ &= P(\text{ observed in bin } i \mid \text{true value in bin } j\ ) \end{aligned} \tag{6.10}$$

where the response matrix element R_{ij} is the conditional probability that an event will be found in bin i given that the true value was in bin j. The effect of off-diagonal elements in R is to smear out any fine structure. Figure 6.27 shows the response matrix distribution for two possible W rapidities. Table 6.6 and Table 6.7 also represent the values in the response matrix. When comparisons are made between a prediction of the W charge asymmetry in bins of this analysis and the measurement, it is this response matrix that should be convoluted with the number of events produced at each charge to compare with the experimental measurement. Fortunately this matrix is largely diagonal so the smearing correction is small, except in the most forward bins.

The acceptance, $a^{\pm}(y_W)$, is simply defined as the fraction of the W events generated that meet the geometric and kinematic requirements of the analysis:

$$a^{\pm}(y_W) = \frac{\#\text{ of events from MC and simulation which pass cuts}}{\#\text{ of events from MC without cuts at generation level}}, \tag{6.11}$$

where the sign, $\pm$, indicates the charge of W boson. The acceptance depends on the charge of the W boson, and such effects need to be carefully studied and evaluated before being applied in this analysis because of their direct impact on the charge asymmetry. The corrections to the acceptance are the trigger efficiency measured from the

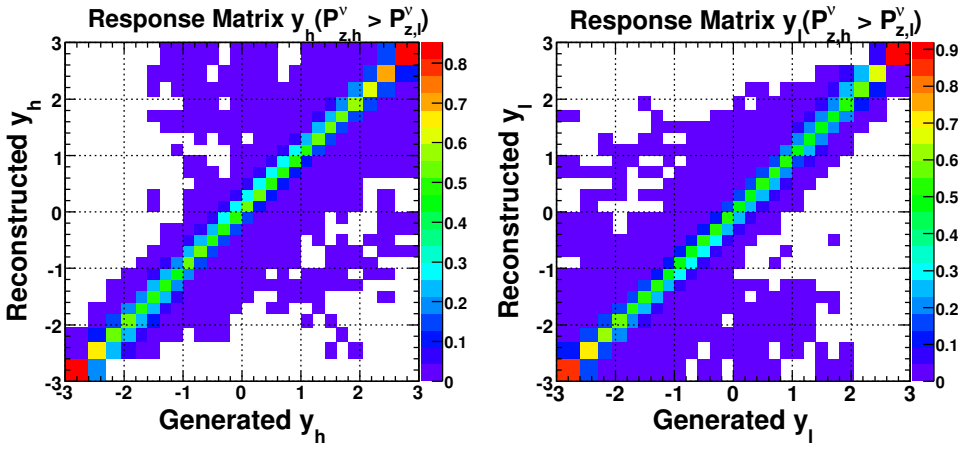

Figure 6.27: Response Matrix for the reconstructed W rapidities ($y_h > y_l$).

y_W	-2.8	-2.45	-2.175	-1.925	-1.7	-1.5	-1.3	-1.1	-0.9	-0.7	-0.5	-0.3	-0.1
-2.8	0.8292	0.0264	0.0007	0	0	0	0	0	0	0	0	0	0
-2.45	0.1707	0.6794	0.1155	0.0091	0	0	0	0	0	0	0	0	0
-2.175	0	0.2256	0.5421	0.1304	0.0132	0.0004	0	0	0	0	0	0	0
-1.925	0	0.0589	0.2455	0.5385	0.1896	0.0356	0.0019	0	0	0	0	0	0
-1.7	0	0.0051	0.0831	0.2152	0.4819	0.194	0.0419	0.0026	0	0	0	0	0
-1.5	0	0.0008	0.0104	0.0905	0.2276	0.4882	0.2181	0.0617	0.0041	0	0	0	0
-1.3	0	0	0.0011	0.0132	0.075	0.2154	0.4881	0.2443	0.0504	0.0025	0	0	0
-1.1	0	0	0.0002	0.0016	0.01	0.0575	0.201	0.467	0.1784	0.0258	0.0013	0	0
-0.9	0	0	0	0.0006	0.0015	0.0065	0.0421	0.1874	0.5534	0.2204	0.0527	0.0041	0
-0.7	0	0	0.0004	0.0002	0.0003	0.001	0.0051	0.0302	0.1614	0.5402	0.2437	0.0675	0.0057
-0.5	0	0	0.0002	0	0.0002	0.0004	0.0007	0.005	0.0404	0.1587	0.5009	0.2547	0.0727
-0.3	0	0	0.0001	0	0	0.0002	0.0002	0.0009	0.0088	0.0421	0.1596	0.4882	0.2662
-0.1	0	0	0	0	0	0	0.0001	0.0004	0.0018	0.0077	0.0343	0.1529	0.4922

Table 6.6: The values in Response Matrix ($y_W < 0.0$).

y_W	0.1	0.3	0.5	0.7	0.9	1.1	1.3	1.5	1.7	1.925	2.175	2.45	2.8
0.1	0.5125	0.271	0.0629	0.0057	0.0001	0	0	0	0	0	0	0	0
0.3	0.1209	0.5241	0.285	0.0704	0.0064	0.0001	0	0	0	0	0	0	0
0.5	0.0183	0.1137	0.5082	0.285	0.071	0.0064	0.0001	0	0	0	0	0	0
0.7	0.003	0.0197	0.1131	0.492	0.2851	0.0697	0.0059	0.0001	0	0	0	0	0
0.9	0.0007	0.0034	0.0207	0.119	0.4787	0.277	0.0498	0.0035	0.0001	0	0	0	0
1.1	0.0001	0.0007	0.0036	0.0223	0.1267	0.4833	0.2327	0.0264	0.002	0.0001	0.0001	0	0
1.3	0	0.0002	0.0008	0.0041	0.0256	0.1357	0.5418	0.2484	0.0496	0.0045	0.0002	0.0001	0.0001
1.5	0	0	0.0002	0.0008	0.0048	0.0232	0.1424	0.5412	0.2429	0.0466	0.0021	0.0001	0
1.7	0	0	0	0.0002	0.0008	0.0035	0.0236	0.1533	0.5197	0.2069	0.0217	0.0006	0.0001
1.925	0	0	0	0	0.0002	0.0005	0.0029	0.0245	0.1681	0.5863	0.2038	0.014	0.0005
2.175	0	0	0	0	0	0	0.0002	0.0016	0.0154	0.1422	0.6263	0.1671	0.0056
2.45	0	0	0	0	0	0	0.0001	0.0003	0.0013	0.012	0.1409	0.7215	0.1412
2.8	0	0	0	0	0	0	0	0	0.0001	0.0006	0.0045	0.0958	0.8519

Table 6.7: The values in Response Matrix ($y_W > 0.0$).

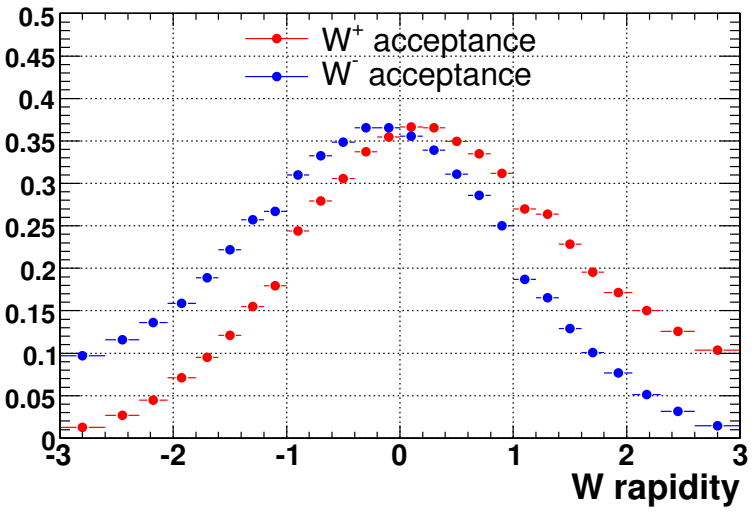

Figure 6.28: The acceptance correction.

data, the electron ID and tracking efficiency scale factors (data/MC) and the charge fake rate also measured in the data. The acceptance correction is shown in Figure 6.28. Note that this acceptance correction must also be iterated since the weighting of the Ws at reconstruction level depends on the underlying assumed distributions.

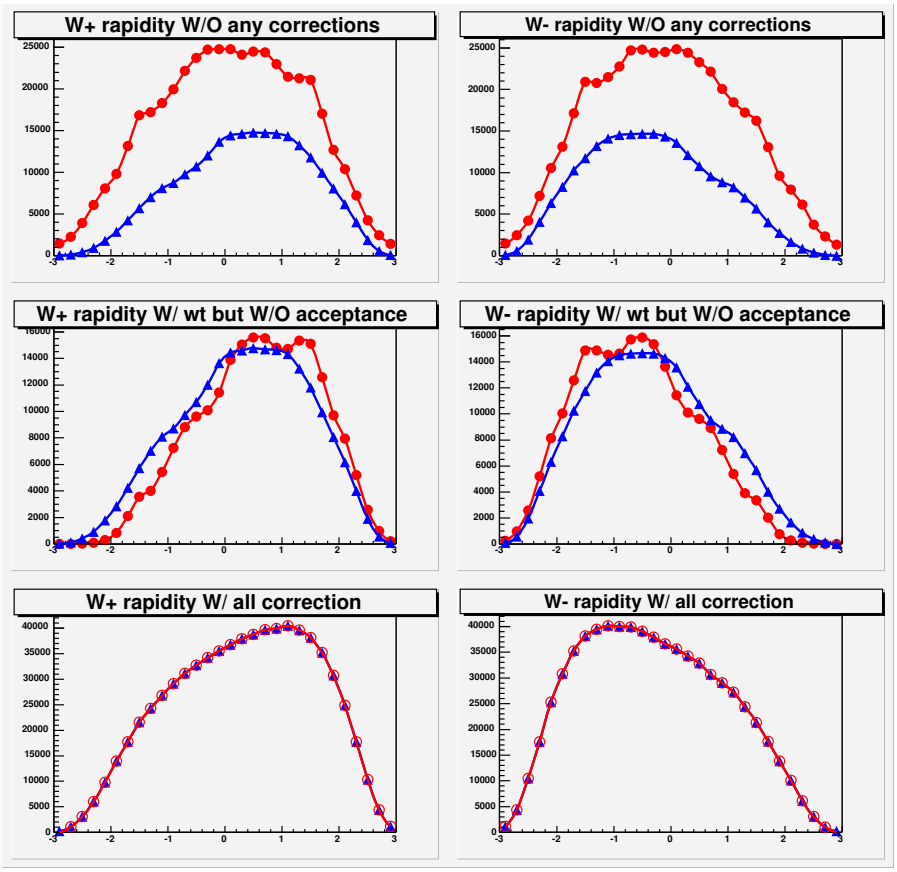

Figure 6.29: The blue triangles show the true W boson rapidity, and the red circles indicate the W rapidity as reconstructed. The top plots show the reconstructed rapidity without weighting or corrections, and the middle plots show the weighted rapidity distributions before the acceptance correction, and the bottom plots show the distributions after weighted and corrected for the acceptance.

Chapter 7

Measurement of W Charge Asymmetry

In this chapter, the results obtained in the preceding sections are put together in to measure the W boson charge asymmetry, which is then interpreted and their significance discussed. The statistical and systematic uncertainties associated with this analysis are summarized in the following sections. The result is compared with the predictions from the perturbative QCD calculation and the different PDFs. The effects on our measurement of the assumed input valence, sea quark and gluon distributions are also studied.

7.1 Summary of Statistical Uncertainties

The W production charge asymmetry is measured by the differential cross sections of $W^{\pm}$ which are reconstructed using the weighting factor in the iterative method. In Eq. 7.1, the statistical uncertainty on the W charge asymmetry is evaluated from the weighting factor of the two possible solutions. Since our iteration method might amplify the expected statistical fluctuations the statistical error is measured using a pseudo-experiment technique. 600 pseudo-experiments are randomly formed from a 20M event $W \rightarrow e\nu$ simulated sample. The total number of events in each pseudo-experiment sam-

ple is set to be the number of $W \rightarrow e\nu$ candidates observed in the data. In Figure 7.1, the result from each of the pseudo-experiments is compared with input default charge asymmetry to the simulation. In the absence of effects from the iteration the calculated statistical error is:

$$\begin{aligned} A_i^{true}(y_W) &= \frac{\mu_i^+ - \mu_i^-}{\mu_i^+ + \mu_i^-} \\ (\sigma_{A_i})^2 &= \frac{4(\mu_i^+\mu_i^-)^2}{(\mu_i^+\mu_i^-)^4} \times \left[\left(\frac{\sigma_{\mu_i}^+}{\mu_i^+} \right)^2 + \left(\frac{\sigma_{\mu_i}^-}{\mu_i^-} \right)^2 \right] \\ \text{where } \mu_\text{i} &= a_i^{-1}\nu_i \\ (\sigma_{\mu_i})^2 &= \left[\left(\frac{\partial \mu_i}{\partial \nu_i} \sigma_{\nu_i} \right)^2 + \left(\frac{\partial \mu_i}{\partial a_i^{-1}} \sigma_{a_i^{-1}} \right)^2 \right] \\ &= \left[(a_i^{-1}\sigma_{\nu_i})^2 + (\nu_i \sigma_{a_i^{-1}})^2 \right] \end{aligned} \tag{7.1}$$

where a_i indicates the acceptance, $(\sigma_{\nu_j})^2 = \sum w^2$, and w is the weighting factor in Eq. 5.6. Figure 7.1 compares the calculated statistical error to the statistical error measured in pseudo-experiments, by defining a "pull", x for each pseudo-experiment and computing to the variance of the estimator σ_x^2 as

$$\begin{aligned} x &\equiv \frac{(A_{PE} - \bar{A})}{\sigma_{A_{PE}}} \\ \sigma_x^2 &= \frac{1}{N-1} \sum_{i=1}^{N} (x_i - \bar{x})^2 \\ V[\sigma_x^2] &= \frac{1}{N} (m_4 - \frac{N-3}{N-1} \sigma^4) \\ m_4 &= \frac{1}{N-1} \sum_{i=1}^{N} (x_i - \bar{x})^4, \end{aligned} \tag{7.2}$$

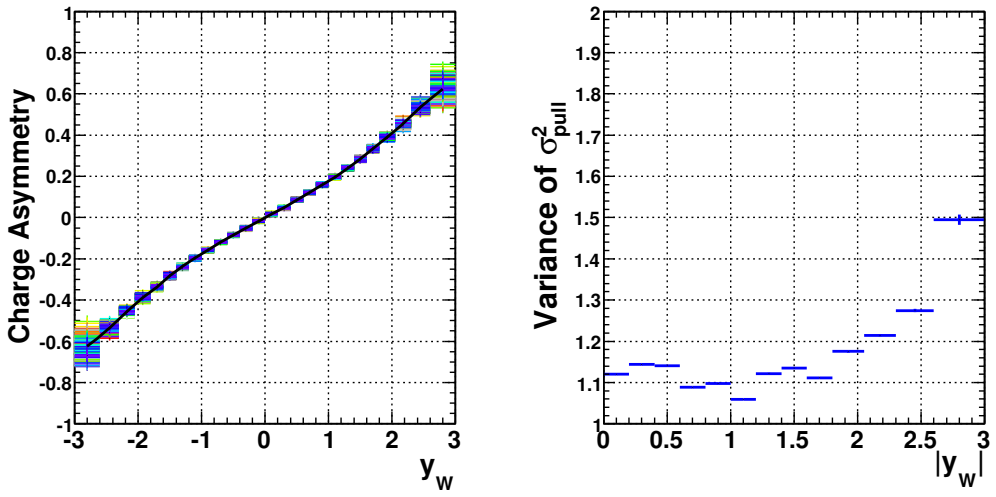

Figure 7.1: The W charge asymmetries from 600 pseudo-experiments (left), the variance of σ_x^2 on pull (right).

where A_{PE} and $\bar{A}$ indicate the charge asymmetry and the expectation for pseudo-experiment. The W charge asymmetries from pseudo-experiments and the variance of the estimator σ_x^2 on the pull are shown in Figure 7.1. As suspected, the statistical error is larger than that calculated in Eq. 7.1. The correlation coefficient of statistical error for adjacent bins is also evaluated and found to be < 0.05 as shown in Figure 7.2. Table 7.1 summarizes the total statistical uncertainty on the W charge asymmetry measurement.

7.2 Summary of Systematic Uncertainties

As described in previous chapters, the systematic uncertainty on the W charge asymmetry measurement arises from several potentially significant sources: the uncertainties in the total (charge summed) W production as a function of rapidity and the ratio of quark and anti-quark in the angular decay distribution, the energy scale uncertainty of the elec-

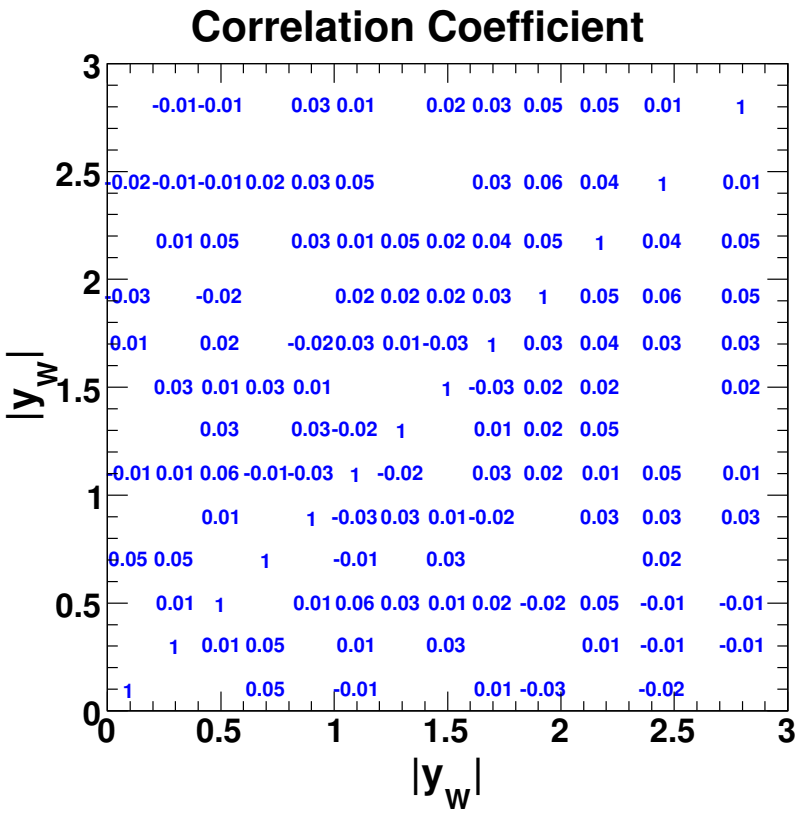

Figure 7.2: The correlation need not be zero because of the iterative method. theses correlations are weakly positive on average, but are small.

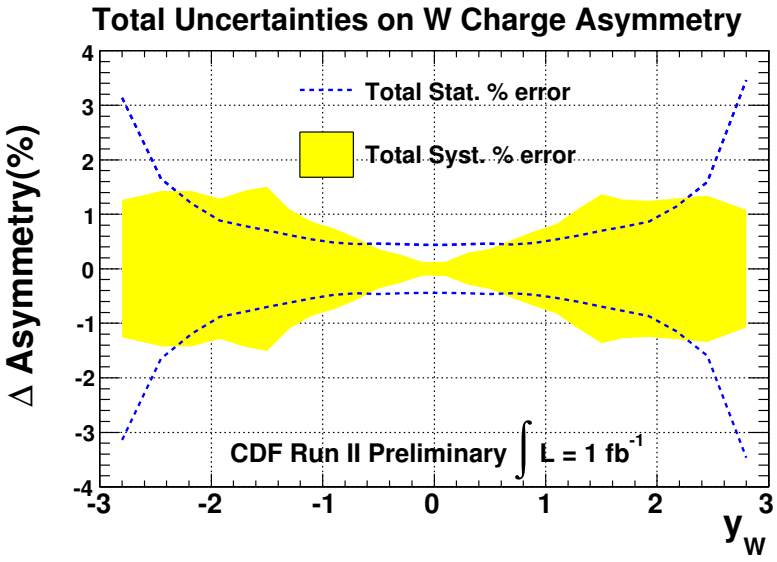

Figure 7.3: Total systematic uncertainty for the W production charge asymmetry comparing to the statistical uncertainty.

tron E_T and the uncertainty in the measured boson recoil energy scale, the uncertainties on the corrections of charge mis-identification and background as well as the trigger efficiency and electron identification scale factor. For each source, the corresponding uncertainty on the W charge asymmetry is evaluated by varying each input quantity by $\pm$ 1σ, by then recalculating W charge asymmetry, and by computing the difference in the new charge asymmetry in each y_W bin. The total systematic uncertainty on W charge asymmetry in a single y_W bin is found by adding in quadrature the uncertainties from the individual sources.

7.2.1 PDF uncertainty on input asymmetry, W rapidity and Q(y_W, p_T)

The charge-summed production $d\sigma/dy_w$ depends (at leading order) on sums of parton distributions such as $u, \bar{u}, dand\bar{d}$ quark and the ratio of anti-quarks and quarks,

$Q(y_W, p_T^W)$, in the angular distribution depends on $(\bar{u}r + \bar{d})/(u + d)$. Since input PDFs are used to determine the parameters of the weighting factor (Eq. 5.6), they may affect the final result and are considered as a source of systematic uncertainty. The uncertainties on the weighting factor arise from uncertainties on the momentum distribution of quarks and gluons in the proton modeled with the PDF sets used. The choice of PDF set has an effect on the shape of the $d(\sigma^+ + \sigma^-)/dy_W$ distribution, on the ratio of anti-quarks and quarks in the angular decay distribution and on the W charge asymmetry itself.

We re-determine the input W charge asymmetry, the $d\sigma/dy_W$ production cross section and the angular distribution of $(1 \pm cos\theta^*)^2$ using the CTEQ6.1M error PDF sets [4]. The systematic effects due to the PDF uncertainty are evaluated by checking the deviation of the asymmetry values based on these calculations from the central values. The effects are independently estimated.

First, we measure how the measured asymmetry is affected if the input asymmetry is varied by the error PDFs while keeping the total differential cross section constant. Figure 7.4(a) shows the input asymmetry and the uncertainty obtained from the error PDFs. The uncertainty on the W charge asymmetry is shown in Figure 7.4(b). Note that a change in the input asymmetry of $\pm$ 0.1 at high rapidity results in a change of the output asymmetry of only $\pm$ 0.003, which is evidence of the success of the iterative method for extracting the W charge asymmetry. We take this remaining bias from the input asymmetry as a systematic uncertainty.

Next, I consider the charge summed production cross-section $d(\sigma^+ + \sigma^-)/dy_W$ which enters into the weighting factor as shown in Eq 5.6. The differential cross section, $d\sigma/dy_W$, is first derived from each error PDF set and then normalized to a fixed value at $y_W = 0$. This normalization is appropriate since the differential cross-section in at central y_W is well known. The uncertainty of the W differential cross section obtained from the error PDF sets is shown in Figure 7.5(a). The resulting systematic uncertainty on the W asymmetry caused by the uncertainty of the differential W cross section is

shown in Figure 7.5(b).

In addition, uncertainties in the factor Q(y_W, p_T), the ratio of production from anti-quarks to that from quarks, will affect the measured W charge asymmetry. To measure the systematic uncertainty, the different cosθ^* distributions are obtained using the error PDFs as shown in Figure 7.6. The average ratio of anti-quark to quark for each of the error PDF sets is shown in Figure 7.7(a). The systematic uncertainty on W asymmetry caused by the change in the ratio of anti-quark to quark in the proton as we vary the PDFs is shown in Figure 7.7(b).

7.2.2 Electron Energy Scale, Resolution, and Recoil Energy Scale Factors

The scale and resolution of the electromagnetic (EM) calorimeter energy and the missing transverse energy ($\not\!\!E_T$) are directly related with the reconstructed W rapidity and thus the asymmetry measurement. The EM calorimeter energy scale and resolution are tuned in the simulation to match the $Z \rightarrow e^+e^-$ data mass peak as described in Section 6.1. The uncertainties on the energy scale and resolution for central electrons have been measured to be $\pm 0.05\%$ and $\pm 0.14\%$; for forward electrons they are $\pm 0.3\%$ and $\pm 0.8\%$, respectively. These values correspond to a $\pm$ 1 σ variation and contribute to the systematic uncertainty of our measurement as shown in Figure 7.8(a) and 7.8(b).

The neutrino transverse energy in our $W \rightarrow e\nu$ sample is determined by the assumption that the vector sum of all transverse energy should be zero and therefore that $\not\!\!E_T$ is only due to the undetected neutrino. Since hadronic transverse energy in the event balances to the W boson recoil energy, this transverse recoil energy, which is affected by multiple interactions in the event, must be carefully determined. Given the energy scale and resolution calibration, we fit the recoil energy in the simulation, including its dependence on η, to the $W \rightarrow e\nu$ data. The uncertainty on the transverse recoil energy

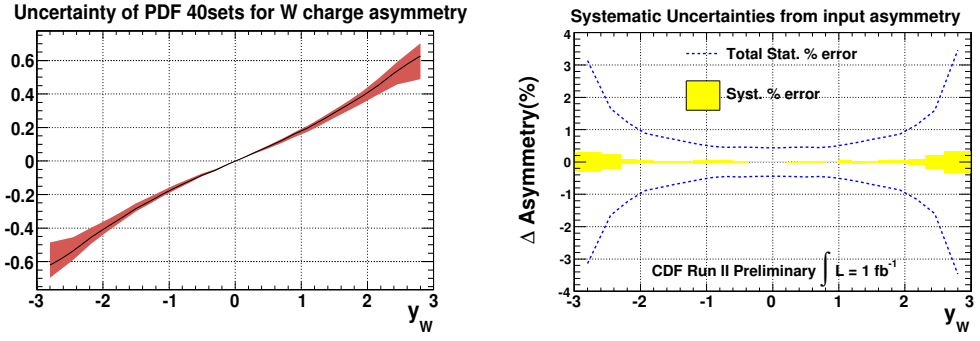

(a) (b)

Figure 7.4: (a) The W charge asymmetry using the error PDF sets. The band is the uncertainty on the input asymmetry from the error PDFs. (b) The systematic uncertainty on W asymmetry caused by varying the input asymmetry.

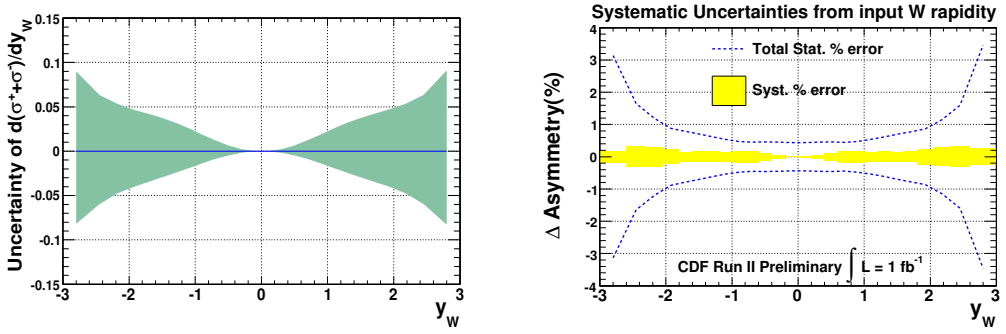

(a) (b)

Figure 7.5: (a) The uncertainty of the W differential cross section using the error PDF sets and the band is quadrature sum of the error PDFs. (b) The systematic uncertainty on W asymmetry caused by the uncertainty of the differential W cross section.

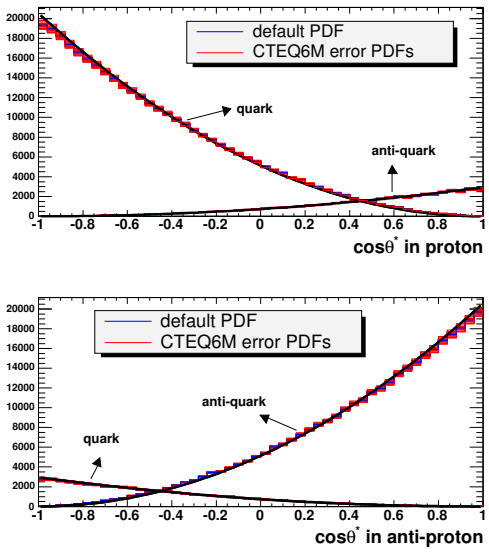

Figure 7.6: The effect of the 40 error PDFs on the cosθ^* distributions in the proton (top) and anti-proton (bottom).

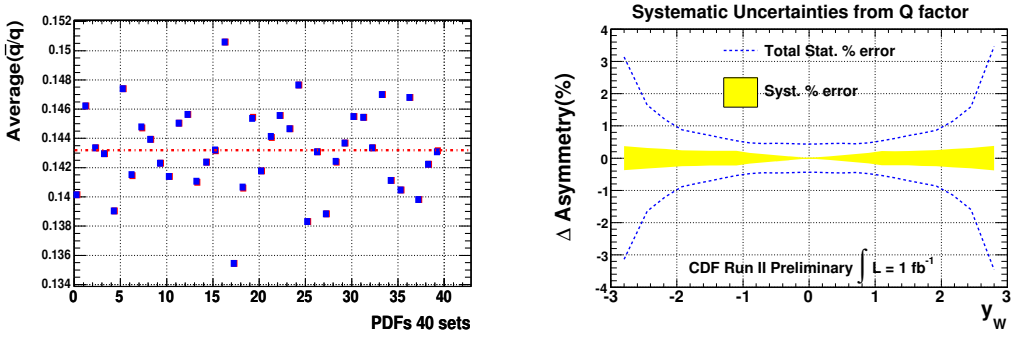

(a) (b)

Figure 7.7: (a) The average ratio of anti-quark to quark for each of the 40 error PDF sets. (b) The systematic uncertainty on the W asymmetry caused by the ratio of anti-quark and quark in the proton.

scale is $\pm 0.3\%$ and $\pm 1.4\%$ for central and forward electrons, respectively. Figure 7.8(c) shows the resulting systematic uncertainty on the W charge asymmetry measurement.

7.2.3 Trigger and Electron ID efficiencies

We investigate sources of any charge bias and η dependence in the kinematic and geometrical acceptance (measured with MC) of the event and efficiencies of the trigger and the electron identification (measured with data). However, these determinations cannot be done with perfect precision. Therefore, uncertainties in data/Monte Carlo scale factors or in measurements of efficiencies directly from the data may cause systematic uncertainties in this result.

The trigger efficiencies for the central and forward electrons are measured using data from independent triggers as discussed in Appendix A. The trigger efficiencies do not depend on charge, but depend on the η and E_T of the electron. The average trigger efficiencies for the central and forward electrons are 96.1$\pm 1.0\%$ and 92.5$\pm 0.3\%$, respectively. Since our MC has no trigger simulation, these efficiencies are applied to the MC to reflect those determined in data in each η bin and E_T value of the electron. Figure 7.9(a) shows the effect of the central and forward trigger efficiency on the W charge asymmetry. Electron identification and track matching efficiencies are measured using $Z \rightarrow e^+e^-$ control samples from both data and MC in Section 6.6. These efficiencies have uncertainties from the data statistics. Additionally, we use the scale factors of the electron ID efficiencies to correct for the differences between MC and data. The forward electron ID efficiency causes the biggest systematic uncertainty which is shown in Figure 7.9(b). The effect of central electron ID efficiency is negligible.

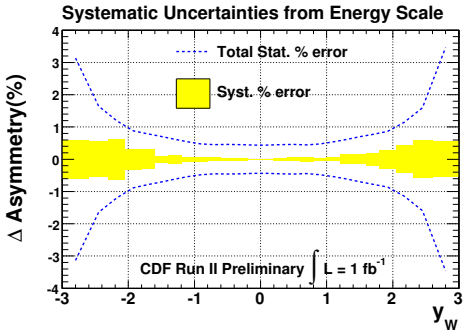

(a)

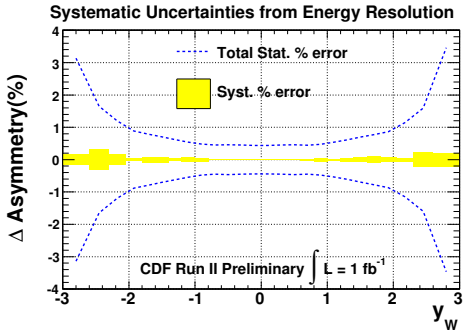

(b)

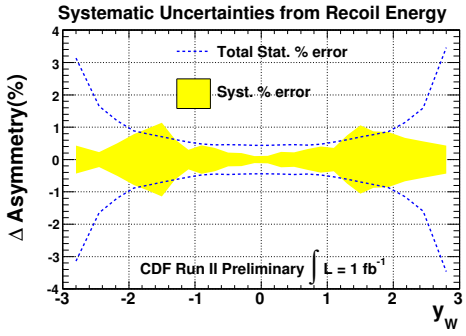

(c)

Figure 7.8: The effects of electron E_T scale uncertainty (a), energy resolution uncertainty (b) and the recoil energy scale uncertainty (c) on the W charge asymmetry.

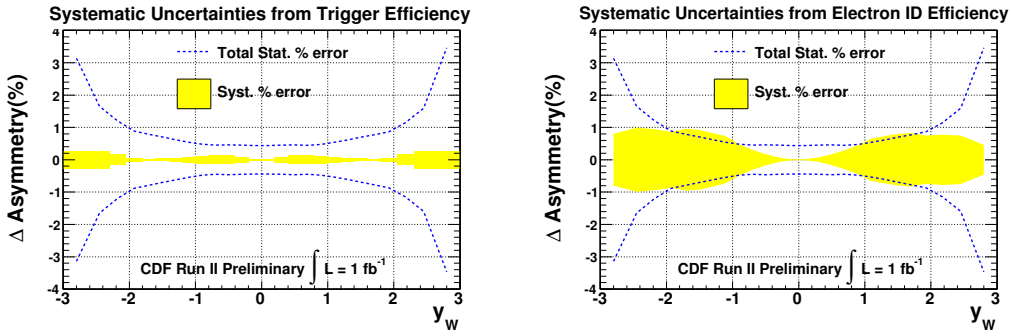

(a) (b)

Figure 7.9: The effect of the trigger efficiency uncertainty for the central and forward electron (a); the effect of the scale factor uncertainty of the forward electron efficiency (b) on the W charge asymmetry.

7.2.4 Charge Fake Rate and Background Estimate

As described in Section 6.3, the charge misidentification rate is determined from $Z \rightarrow e^+e^-$ events in different ranges of η_d where one lepton is used to identify the charge of the other. Therefore, the statistically limited $Z \rightarrow e^+e^-$ sample yields an uncertainty on estimating the charge misidentification rate, and the effect of this uncertainty is shown in Figure 7.10(a). As shown in Section 6.4, significant background contributions to our $W \rightarrow e\nu$ candidates come from QCD events with misidentified jets faking electrons and from $Z \rightarrow e^+e^-$ events where one of the jets or electrons is not reconstructed and mimics a neutrino. The background contributions to W charge asymmetry are corrected. The background from misidentified jets is estimated by fitting the isolation distribution of electron candidates. The uncertainty of fitting the isolation distribution shapes arises from the variation of electron and jet templates. The effect of the charge fake rate uncertainty and the QCD background on the W charge asymmetry is shown in Figure 7.10(a) and 7.10(b). Additionally, there is a systematic uncertainty due to the $Z \rightarrow e^+e^-$

background in Figure 7.10(c).

7.2.5 W boson p_T distribution

Although the transverse momentum of the W in simulation is corrected with parameters tuned on the transverse momentum of Z from $Z \rightarrow e^+e^-$ data, we further address the effects of the p_T^W distribution of produced W bosons since initial state soft gluon radiation and intrinsic p_T of partons in the proton are not very well known. These effects include the weighting factor being a function of p_T^W and the transverse boost of the W boson which affects the angular distributions and energies of the decay electrons and hence the acceptance.

The corrected p_T^W distribution in simulation is shown in Figure 7.11(a). The p_T^W relatively has a good agreement except for a small discrepancy at low p_T. To improve the agreement, a small Gaussian smearing of the simulation with the zero mean and 0.4GeV σ is added. Because this procedure isn't well motivated by a model, we consider the effect of the addition of this smearing as a systematic uncertainty. However, the corresponding uncertainty on the W charge asymmetry is less than 10^{-5}, which is a negligible effect.

7.3 Results for W Charge Asymmetry

In this section the measurement of the W production charge asymmetry is presented using an integrated luminosity of 1 fb^{-1}. The W rapidity is directly measured through our analysis method described in Chapter 5, and analysis corrections are considered to address several experimental effects discussed in Chapter 6.

Recall that several effects, such as tracking efficiency and charge fake rate, had some significant changes in the two different running periods considered in this analysis. Be-

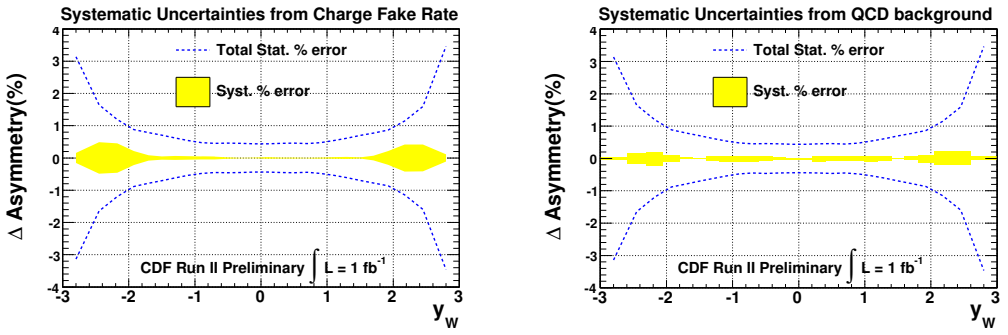

(a)

(b)

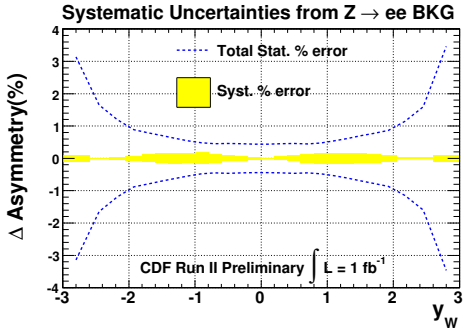

(c)

Figure 7.10: The effect of the charge fake rate uncertainty (a) and QCD event (b) and $Z \rightarrow e^+e^-$ event (c) contributions on the W charge asymmetry.

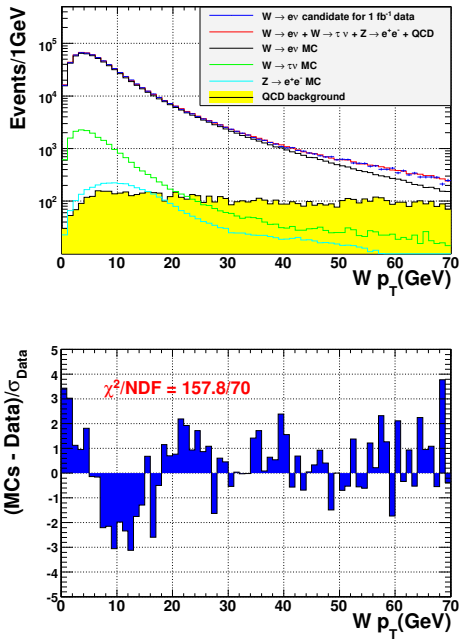

(a) The corrected p_T^W without an additional smearing

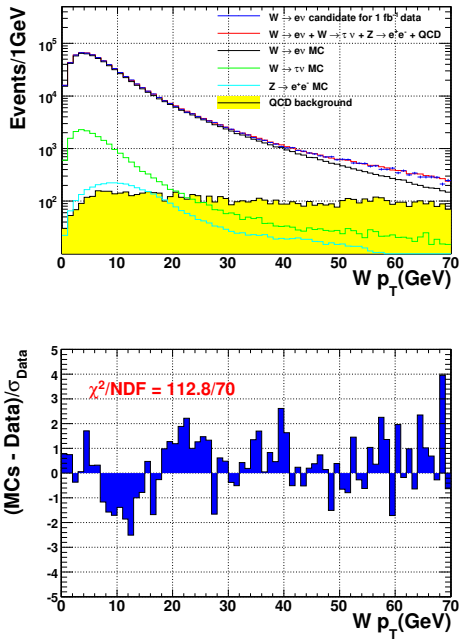

(b) The corrected p_T^W with an additional smearing

Figure 7.11: W boson p_T distribution (top) and the discrepancy between the resulting p_T distributions in simulation and data (bottom).

fore combining the two periods, we first see whether they give the same measured charge asymmetry. In Figure 7.12(a), the corrected asymmetries are shown for two different run-periods in bins of reconstructed rapidity of the W and as can be seen the agreement is reasonably good. Both asymmetry values are then combined in Figure 7.12(b).

CP invariance requires $A(y_W) = -A(-y_W)$. The full corrected data shown in Figure 7.12(b) have no significant evidence of CP asymmetry as shown in Figure 7.13. The level of agreement is characterized by χ^2/dof = 13.1/13. Therefore, the $\pm y_W$ data may be folded together to obtain a more precise measure of $A(|y_W|)$. To fold the asymmetry, the correlations between positive and negative W rapidity bins should be taken into account. Since most of the systematic uncertainties discussed in Section 7.2 are completely correlated between positive and negative y_W, it is fair and simple to assume 100% correlation of all systematic uncertainties in the folding procedure.

The statistical combination of the asymmetry at positive rapidity with the negative of the asymmetry at negative rapidity is performed using the Best Linear Unbiased Estimate (BLUE) method [40] accounting for all correlations for both positive and negative bins in W rapidity. Table 7.1 summarizes the statistical and systematic uncertainties on the W boson production charge asymmetry for rapidities $|y_W| < 3.0$.

The measured asymmetry A($|y_W|$), combining the positive and negative y_W bins, is shown in Figure 7.14. Also shown are the predictions of a NNLO QCD calculation using the MRST 2006 NNLO PDF sets [5] and a NLO QCD calculation using the CTEQ6.1M NLO PDF sets [4]. The results of χ^2 tests between the thirteen data points and the central asymmetry values for the CTEQ6M sets and the MRST2006 sets are 11.8 and 28.8, respectively. The W boson charge asymmetry for each $|y_W|$ with the total systematic uncertainty and the statistical uncertainty obtained in this 1 fb^{-1} measurement is summarized in Table 7.2. In addition the charge asymmetry as a function of electron rapidity is measured with this 1 fb^{-1} data as a cross-check and is shown in Appendix B.

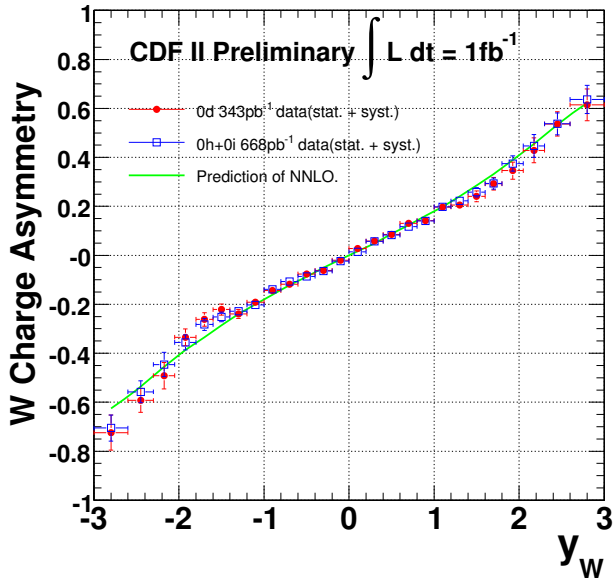

(a) The result for both run-periods

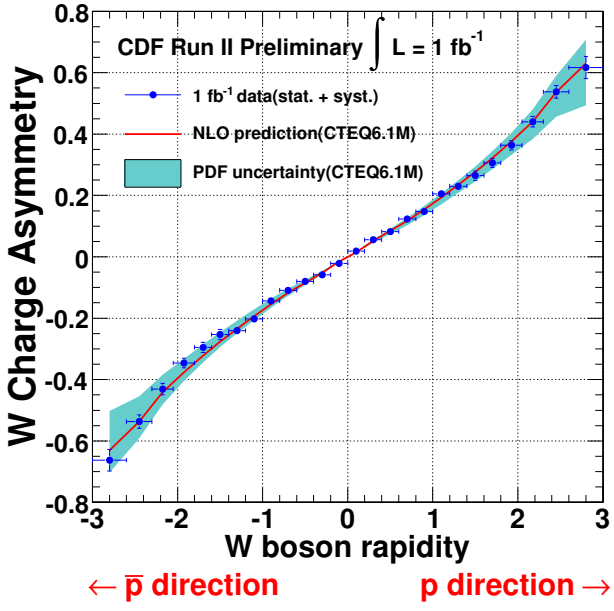

(b) The result for combined data

Figure 7.12: The corrected W production charge asymmetry.

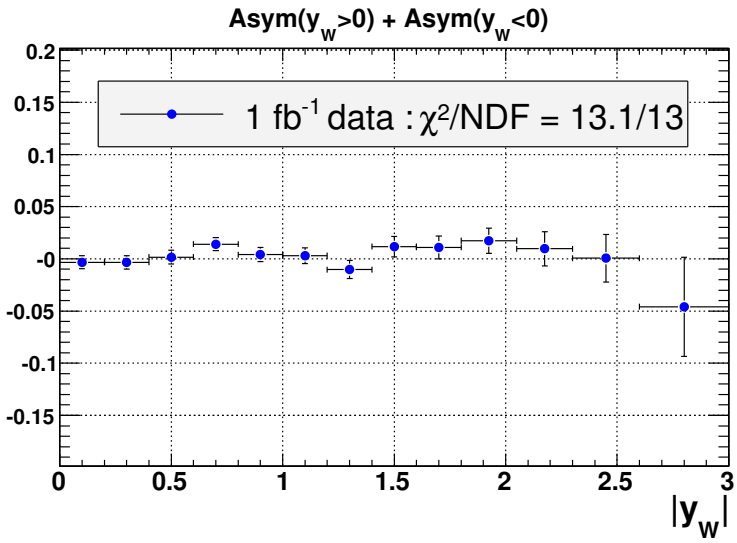

Figure 7.13: The sum of $A(y_W)$ and $A(-y_W)$. The error shown is only the statistical uncertainty.

$\lvert y_W \rvert$	$\Delta A(\lvert y_W \rvert)$ ($\times 10^{-2}$)							Stat.
	CFR	BKG	EM	Recoil	Trig	ID	PDF	(1fb^{-1})
0.0 - 0.2	0.02	0.04	0.01	0.11	0.03	0.02	0.03	0.31
0.2 - 0.4	0.01	0.09	0.04	0.22	0.08	0.07	0.08	0.32
0.4 - 0.6	0.02	0.11	0.06	0.22	0.13	0.17	0.15	0.33
0.6 - 0.8	0.03	0.15	0.07	0.34	0.14	0.30	0.22	0.32
0.8 - 1.0	0.03	0.20	0.07	0.42	0.11	0.47	0.24	0.34
1.0 - 1.2	0.04	0.18	0.08	0.33	0.09	0.69	0.27	0.38
1.2 - 1.4	0.05	0.18	0.15	0.67	0.06	0.78	0.28	0.43
1.4 - 1.6	0.04	0.14	0.14	1.10	0.04	0.85	0.28	0.50
1.6 - 1.8	0.08	0.12	0.26	0.92	0.03	0.89	0.29	0.55
1.8 - 2.05	0.22	0.13	0.31	0.82	0.06	0.80	0.34	0.62
2.05 - 2.3	0.44	0.21	0.53	0.59	0.17	0.85	0.42	0.83
2.3 - 2.6	0.45	0.19	0.62	0.40	0.27	0.86	0.50	1.10
2.6 - 3.0	0.14	0.10	0.60	0.43	0.28	0.65	0.53	2.30

Table 7.1: Systematic uncertainties for the W production charge asymmetry. The values shows the correlated uncertainties for both positive and negative rapidities.

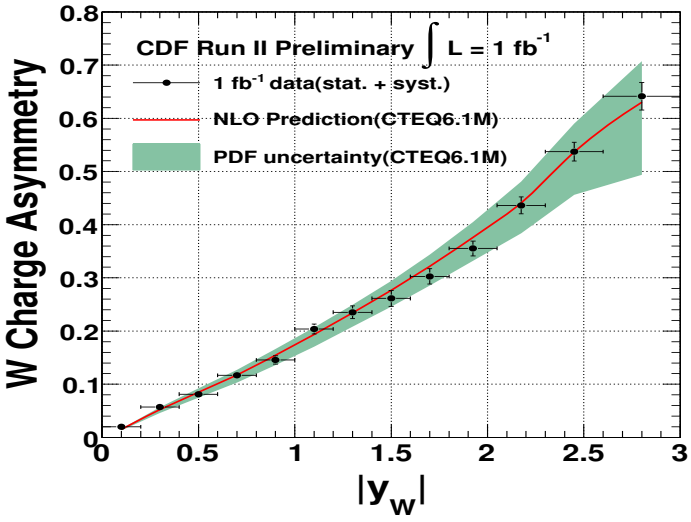

(a) Comparison with NLO predictions from CTEQ6.1 PDFs

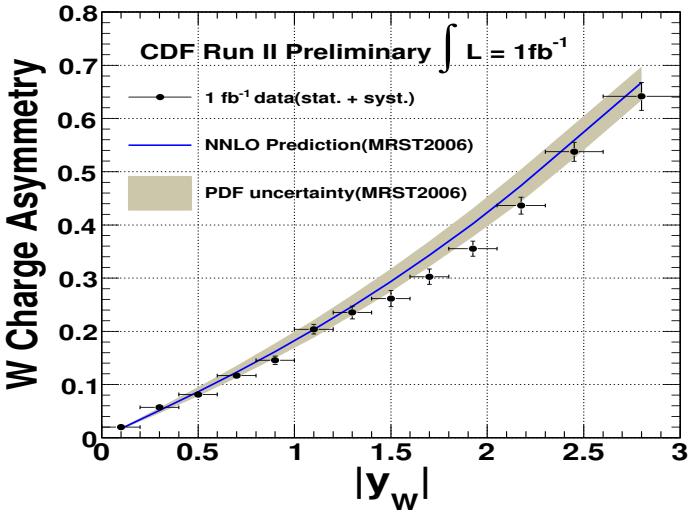

(b) Comparison with NNLO predictions from MRST2006 PDFs

Figure 7.14: The W production charge asymmetry and predictions from (a) CTEQ6.1 with the associated PDF uncertainty and (b) MRTST2006 and its associated PDF uncertainty.

$\lvert y_W \rvert$	$< \lvert yW \rvert >$	$A(y_W)$	σ_{sys}	$\sigma_{sys+stat}$
0.0 - 0.2	0.100	0.0199	$\pm$0.0013	$\pm$0.0034
0.2 - 0.4	0.299	0.0571	$\pm$0.0027	$\pm$0.0042
0.4 - 0.6	0.499	0.0813	$\pm$0.0037	$\pm$0.0049
0.6 - 0.8	0.699	0.1168	$\pm$0.0055	$\pm$0.0063
0.8 - 1.0	0.897	0.1456	$\pm$0.0072	$\pm$0.0079
1.0 - 1.2	1.096	0.2040	$\pm$0.0084	$\pm$0.0092
1.2 - 1.4	1.298	0.2354	$\pm$0.0109	$\pm$0.0118
1.4 - 1.6	1.495	0.2613	$\pm$0.0143	$\pm$0.0151
1.6 - 1.8	1.696	0.3027	$\pm$0.0135	$\pm$0.0144
1.8 - 2.05	1.915	0.3553	$\pm$0.0126	$\pm$0.0141
2.05 - 2.3	2.164	0.4363	$\pm$0.0134	$\pm$0.0158
2.3 - 2.6	2.422	0.5374	$\pm$0.0136	$\pm$0.0178
2.6 - 3.0	2.718	0.6415	$\pm$0.0116	$\pm$0.0260

Table 7.2: The W production charge asymmetry with total systematic and statistical uncertainties.

7.4 Effects of Input Parton Distribution Functions

The goal of this section is to test how the valence quark, sea quark and gluon distributions affect our W charge asymmetry measurement. To do this study Monte Carlo sample is generated by MC@NLO program with NLO QCD calculation and CTEQ6.1M PDFs to determine the quarks and gluon distributions involving the W boson production. The parton distributions in the range $10^{-4} < x < 1.0$ are shown in Figure 7.15.

As shown in Eq. 1.4 and in Figure 1.4, the momentum fraction, x, is directly related to the rapidity of the W boson, and so it might be expected that changes of PDFs in a limited x range will affect a narrow region of rapidity. However, input PDFs are used in many cases to distinguish between two solutions, and therefore, a change in the input PDFs in a particular x range can actually affect a broader ranges of rapidities than one might naively expect. Both types of effects can be seen in the studies below. The effects on our measurement are independently estimated for the valence quarks, sea quarks

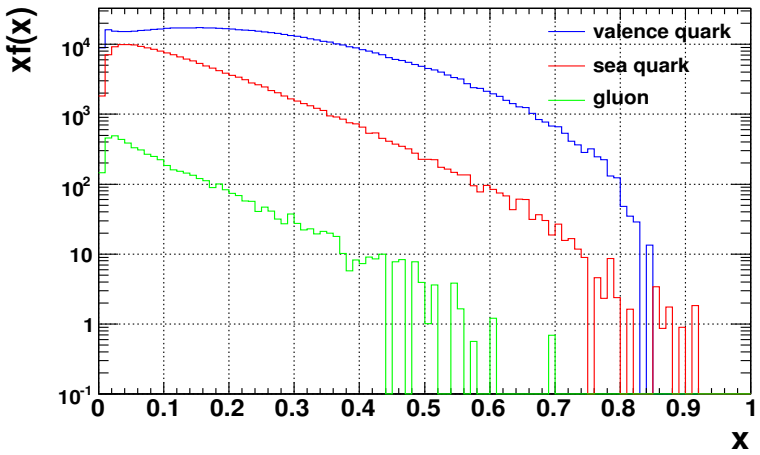

Figure 7.15: The parton distributions of valence quark, sea quark and gluon associated with the W production in $p\bar{p}$ collisions.

and the gluon distribution. The valence and sea quarks distribution are determined as $q_v(x) = q(x) - \bar{q}(x)$ and $q_s(x) = 2 \times \bar{q}(x)$ since the Monte Carlo sample has only quarks and anti-quarks distributions.

$$\begin{aligned} q_v(x) &= q_v(x) + 5\% \times q_v(x) \\ q_s(x) &= q_s(x) + 5\% \times q_s(x) \\ g(x) &= g(x) + 20\% \times g(x), \end{aligned} \tag{7.3}$$

where $g(x)$ is gluon distribution.

In the first study, the valence quark distributions within a fine x bin are increased by 5% (Eq. 7.3), where the distributions for both proton and antiproton are changed while keeping the $d(x)/u(x)$ and $\bar{d}(x)/\bar{u}(x)$ constant. Then the rapidity of W boson is reconstructed again using our analysis method. The result of measured W charge asymmetry corresponding reweighted PDFs is compared with the initial asymmetry and

the difference is examined. In different x ranges, the differences in the measured W charge asymmetry are shown in Figure 7.16 and Figure 7.17.

A similar study varying the weight of up and down sea quarks by +5$\%$ is shown in Figure 7.18 and Figure 7.19. For the gluon distribution, the effect on our measurement is negligible for all x range as shown in Figure 7.20 and Figure 7.21. Note that the effects of even these large changes in the quark and gluon distributions is small ($\lesssim 0.003$) compared with the statistical uncertainty ($\gtrsim 0.004$). This study allows one to estimate the effect on this W asymmetry measurement from the variation of input parton distribution functions. In Appendix C, we summarize and provide the values of the effects for valence quark, sea quark and gluon distributions.

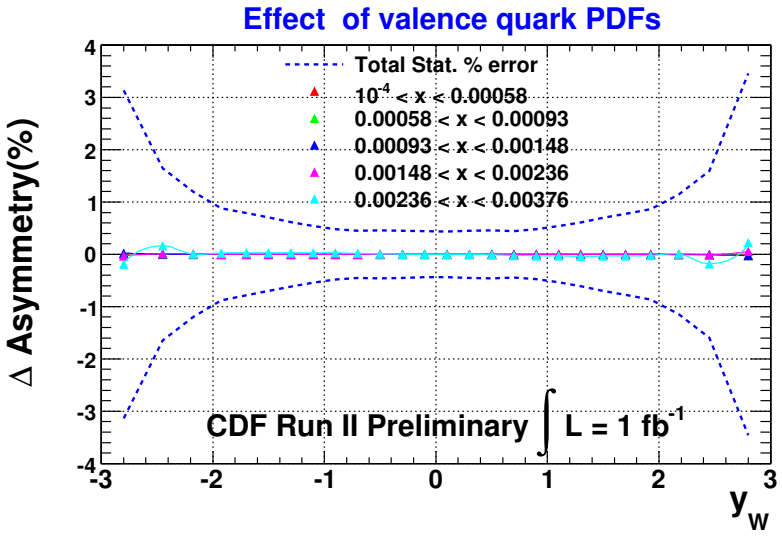

(a) $10^{-4} < x < 0.00376$

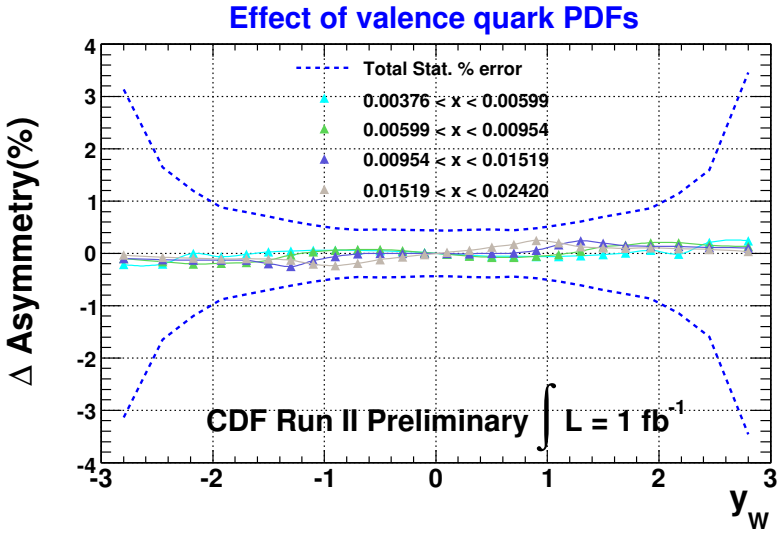

(b) $0.00376 < x < 0.02420$

Figure 7.16: The shift of the W charge asymmetry when the valence quark distribution is weighted by +5% at low x region.

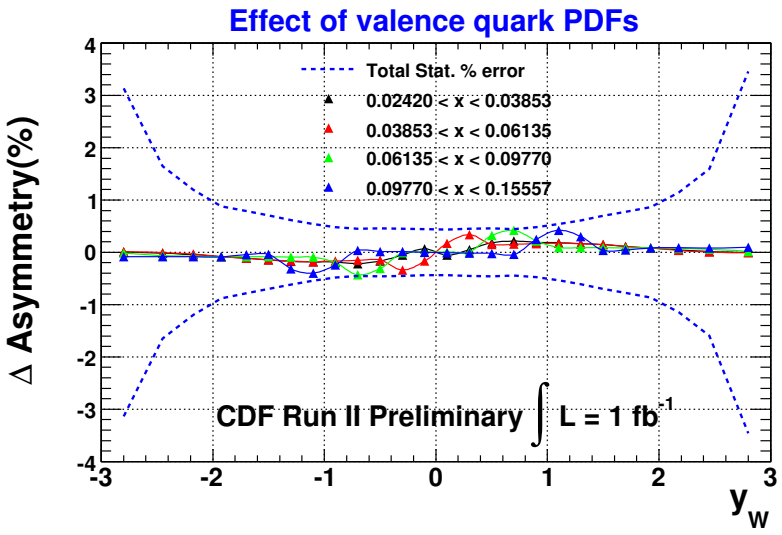

(a) $0.02420 < x < 0.15557$

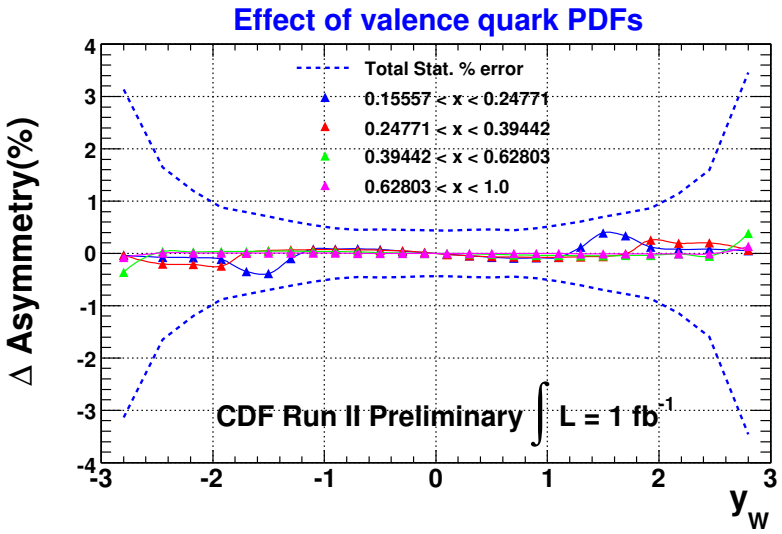

(b) $0.15557 < x < 1.0$

Figure 7.17: The shift of the W charge asymmetry when the valence quark distribution is weighted by +5% at high x region.

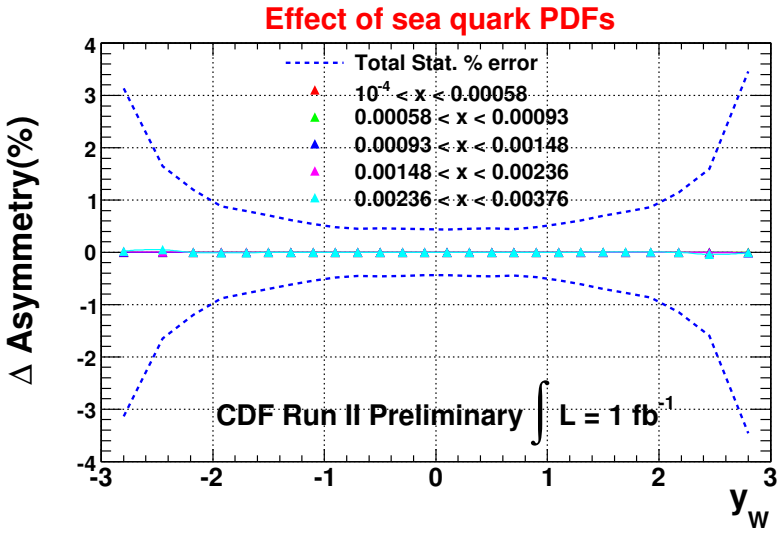

(a) $10^{-4} < x < 0.00376$

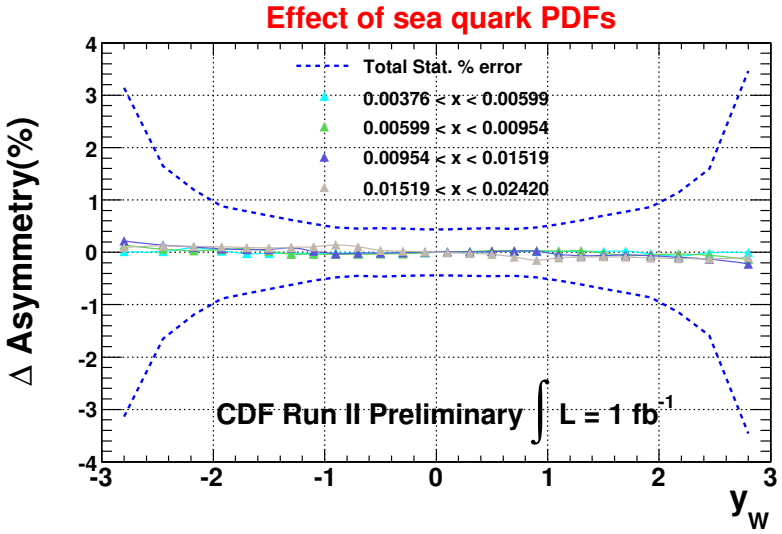

(b) $0.00376 < x < 0.02420$

Figure 7.18: The shift of the W charge asymmetry when the sea quark distribution is weighted by +5% at low x region.

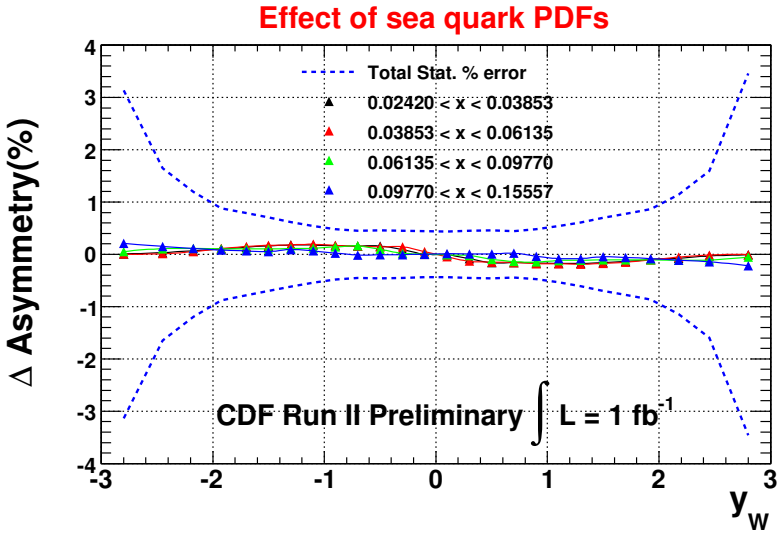

(a) $0.02420 < x < 0.15557$

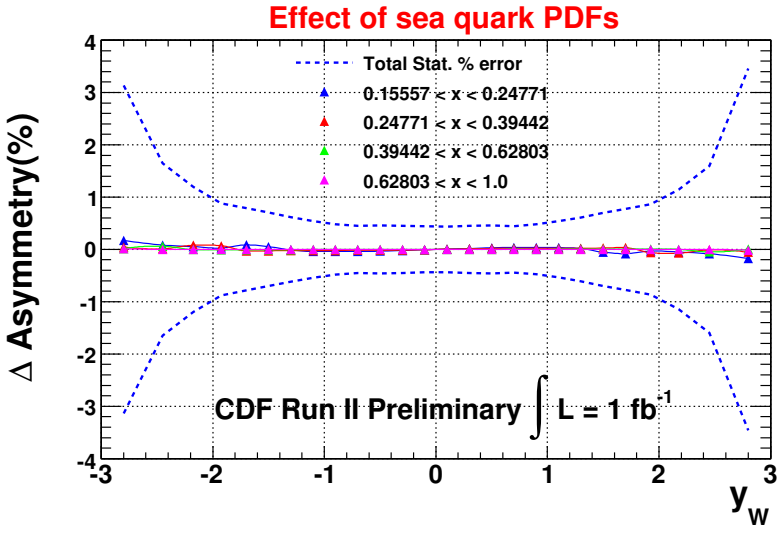

(b) $0.15557 < x < 1.0$

Figure 7.19: The shift of the W charge asymmetry when the sea quark distribution is weighted by +5% at high x region.

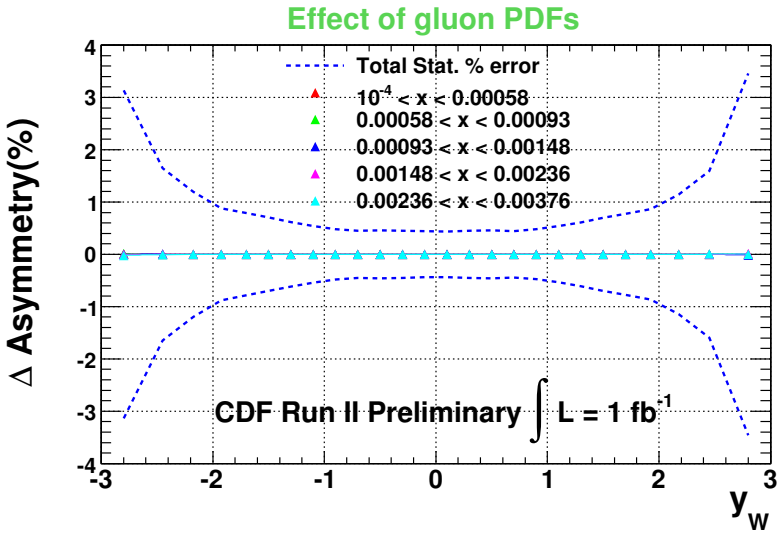

(a) $10^{-4} < x < 0.00376$

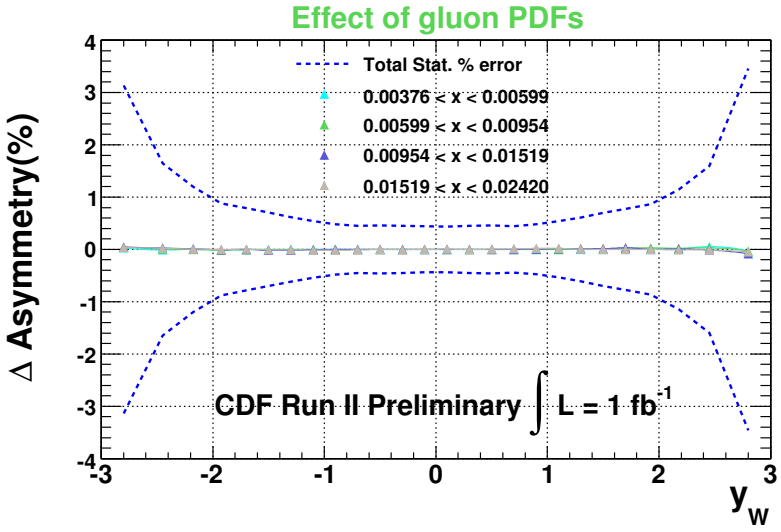

(b) $0.00376 < x < 0.02420$

Figure 7.20: The shift of the W charge asymmetry when the gluon distribution is weighted by +5% at low x region.

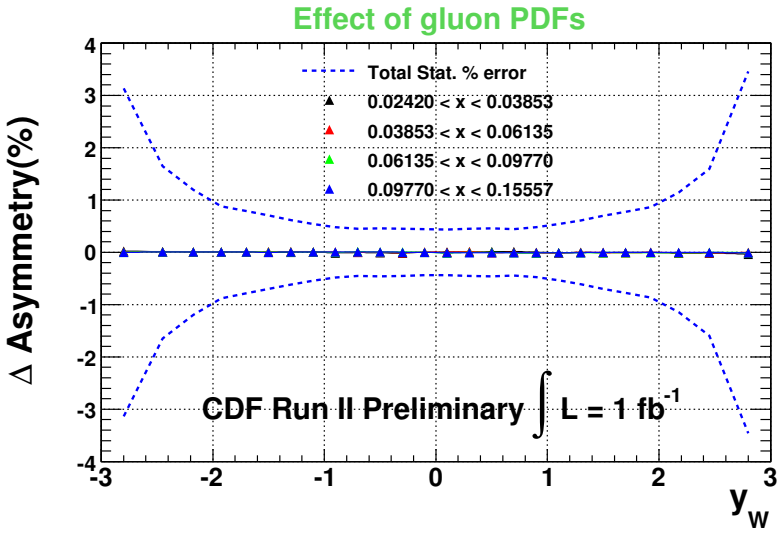

(a) $0.02420 < x < 0.15557$

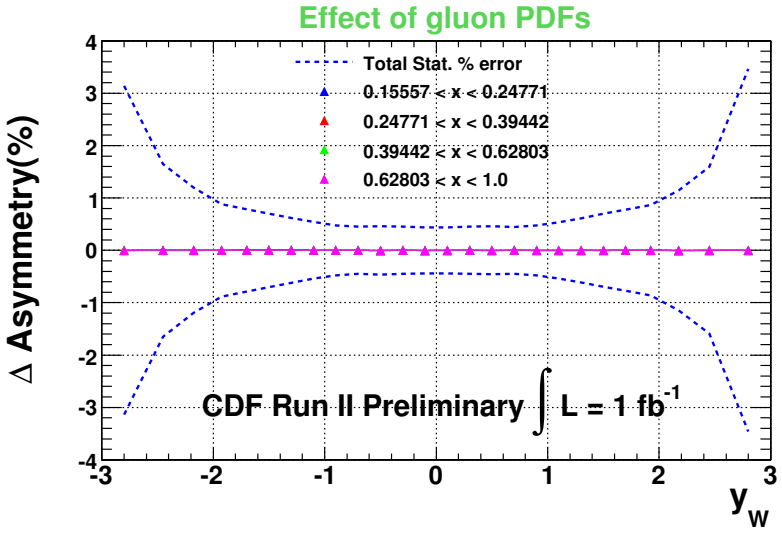

(b) $0.15557 < x < 1.0$

Figure 7.21: The shift of the W charge asymmetry when the gluon distribution is weighted by +5% at high x region.

Chapter 8

Summary and Conclusion

At the Fermilab Tevatron, where $p\bar{p}$ collisions occur at $\sqrt{s} = 1.96$ TeV, the W^+ and W^- boson rapidity distributions result in a charge asymmetry since u quarks carry, on average, a higher fraction of the proton's momentum than d quarks. The parton distribution functions (PDF) describing the internal structure of the proton can be constrained by measuring this charge asymmetry of the production of the W bosons.

Previous measurements of the W charge asymmetry at the Tevatron measured the pseudo-rapidity (η) distribution of leptons from decays of W bosons since the W decay involves a neutrino whose longitudinal momentum is experimentally undetermined. However, this lepton charge asymmetry is a convolution of the W production charge asymmetry and the $V - A$ asymmetry from W decay, and the two asymmetries tend to cancel in the forward region ($|\eta| \gtrsim 2.0$). As a result, it is more complicated to interpret the correlation between the proton PDFs and the lepton charge asymmetry. In this thesis, this complication is resolved in a direct measurement of the W production charge asymmetry as a function of the $W^{\pm}$ rapidity.

The analysis is based on the ability to efficiently identify the leptonic decay products of the W. The events are triggered using the decay lepton from the W in the central

region, and by using both the electron and missing transverse energy in the forward region. A W candidate is then reconstructed from tightly selected electron with a good quality track and from the corrected missing transverse energy. The data sample is taken from approximately $1\mathrm{fb}^{-1}$ of proton-antiproton collisions at $\sqrt{s} = 1.96\ \mathrm{TeV}$ produced at the Fermilab Tevatron and recorded with the Collider Detector Facility.

An analysis technique was developed to determine the neutrino longitudinal momentum, up to a two-fold ambiguity, by constraining the W mass. The ambiguity is resolved on a statistical basis from the known $V - A$ decay distribution and from the differential cross-sections, $d\sigma^{\pm}/dy_W$. The background from QCD events is estimated using the calorimeter energy distribution outside the electron cluster which is higher for a jet that is detected as an electron. Additionally, other electroweak processes are studied for possible contributions to the W candidates.

Using these techniques, the W production charge asymmetry is measured from the selected candidates and is compared to the global PDF fits by both the CTEQ and MRST collaborations. This measurement will significantly improve the precision on the proton d/u momentum ratio over previous lepton charge asymmetry measurements at the Tevatron.

Appendix A

Trigger Efficiencies

A.1 Central Electron trigger Efficiency

As the central electron trigger is the basis of a large number of anaylses, the trigger efficiency was performed by several groups within the CDF collaboration. A summary of the results is given here, with more complete details in [41]. The central electron trigger is based upon both calorimeter and tracking quantities, and so the measurement of the efficiency is split between these two systems. The tracking efficiency is measured using a W trigger with no tracking requirements, W_NOTRACK, while the calorimeter efficiencies are measured using data samples collected from muon triggers or prescaled auto-accept triggers. The tracking and calorimeter efficiencies are multiplied together for a total central electron trigger efficiency.

A.1.1 XFT Efficiency

At L1, the central electron trigger requires an XFT track of 8 $\mathrm{GeV/c}$. The trigger efficiency is measured by applying the central event selection, listed in Table 3.1, to the W_NOTRACK trigger sample. After selecting a W candidate event, the L1_XFT_PT8

trigger bit is checked, and the efficiency calculated with Equation A.1.

$$\epsilon(\mathrm{L1\_XFT\_PT8}) = \frac{\mathrm{W\_NOTRACK\ \&\ L1\_CEM8\_PT8}}{\mathrm{W\_NOTRACK}} \tag{A.1}$$

Except for a small dependence upon the η distribution of the electron as shown in Figure A.1, the efficiency is independent of kinematic variables, and the integrated L1_XFT_PT8 efficiency 96.3%.

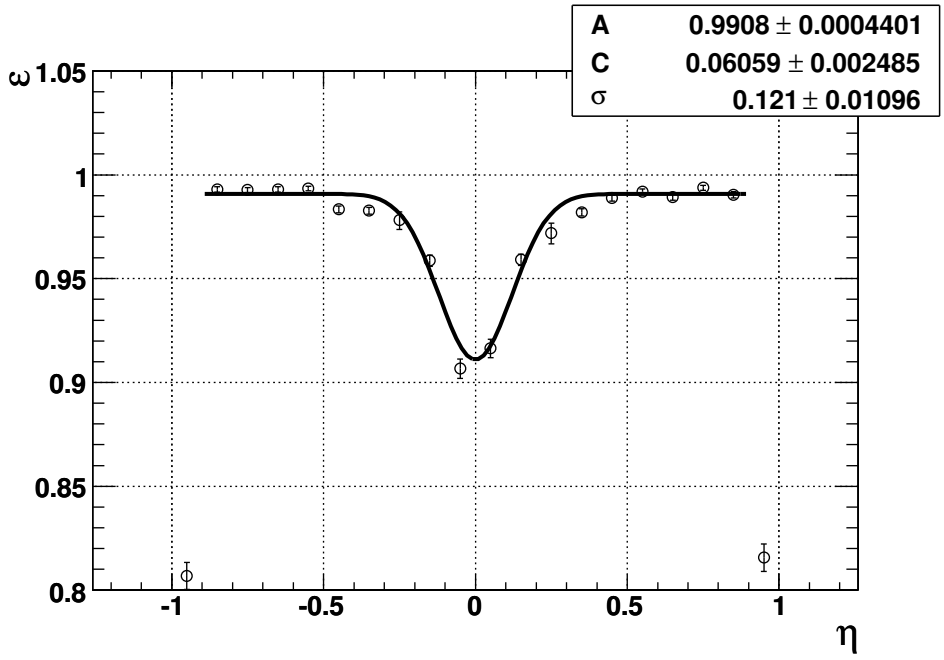

Figure A.1: L1 tracking trigger efficiency as a function of detector η.

No additional requirement is made on the tracking at L2, but the efficiency was checked to certify that no errors occurred within the trigger hardware. No such problems were found, and the L2_XFT_PT8 is 100%.

The L3 central electron trigger requires that a 3D track with p_T greater than 9 $\mathrm{GeV/c}$ be reconstructed in the COT. Selecting W candidates dataset triggered from the

W_NOTRACK trigger, the events are also required to have the passed the L1_CEM_PT8 and L2_CEM16_PT8 triggers to isolate the efficiency at L3 from effects upstream in the trigger. The formula for the L3 tracking efficiency is then given in Equation A.2.

$$\epsilon(\mathrm{L3\_PT9}) = \frac{\mathrm{W\_NOTRACK\ \&\ L1\_CEM8\_PT8\ \&\ L2\_CEM16\_PT8\ \&\ L3\_CEM18\_PT9}}{\mathrm{W\_NOTRACK\ \&\ L1\_CEM8\_PT8\ \&\ L2\_CEM16\_PT8}} \tag{A.2}$$

No dependence on any kinematic variable is found, and the integrated L3_PT9 trigger efficiency is measured to be 99.6%.

A.1.2 Calorimeter Trigger Efficiency

At L1, the central electron trigger requires a tower with EM $E_T > 8\mathrm{GeV}$, L1_CEM8. Unfortunately, there was no trigger used during the data taking process that used the L1_CEM8 without it being coupled to some other trigger requirement (e.g. track, $\not\!\!E_T$, etc.). The L1_EM8 trigger bit is decoupled from other trigger requirements though, and so by requiring minimal activity in the forward calorimeter, the trigger response in the central calorimeter is measured. The control sample was collected using muon triggerd events, and the activity in the calorimeter is considered. The energy in the calorimeter towers is combined into the trigger geometry (two physical towers per trigger tower). If an event has a trigger tower with energy greater than 8 GeV, the L1_EM8 trigger bit is checked. The efficiency is found to be 100% for towers with energy greater than 14 GeV, a threshold much lower than the central electron cut of 25 GeV.

The L2 calorimeter trigger requires EM $E_T > 16\mathrm{GeV}$, and its efficiency is measured with a prescaled, auto-accept L2 trigger, L2_PS50_L1_CEM8_PT8. This trigger has the identical path as the central electron trigger with the exception of L2, where no calorimeter requirements are applied. After selecting central W candidates, the effi-

ciency is measured from Equation A.3.

$$\epsilon(\mathrm{L2\_CEM16}) = \frac{\mathrm{L1\_CEM8\_PT8\ \&\ L2\_PS\ \&\ L2\_CEM16}}{\mathrm{L1\_CEM8\_PT8\ \&\ L2\_PS}} \tag{A.3}$$

The trigger is measured to be 100% efficient within statistical errors for all E_T above 25 GeV.

The L3 central electron trigger efficiency is measured using a sample of lower-E_T, inclusive electron trigger events, ELECTRON_CENTRAL_8. By requiring that the events in the sample have passed the L1 and L2 central electron trigger path, only the effect of the L3 trigger is measured. After selecting central W events, the efficiency is calculated from Equation A.4.

$$\epsilon(\mathrm{L3\_CEM18}) = \frac{\mathrm{EL\_CENT\_8\_NO\_L2\ \&\ L2\_CEM16\ \&\ L3\_CEM18}}{\mathrm{EL\_CENT\_8\_NO\_L2\ \&\ L2\_CEM16}} \tag{A.4}$$

Since the full calorimeter reconstruction is performed at L3, the only difference between offline and trigger quantities is the offline calibrations which are no larger than 10%. The efficiency is therefore expected to be near 100%, and the measured efficiency is found to reach 100% at 23 GeV as suspected.

All of the calorimeter trigger efficiencies are calculated to be 100% for an electron selection with E_T greater than 25 GeV.

A.2 Forward W Trigger Efficiency

The forward W trigger is based solely on calorimeter quantities, and the control samples collected from prescaled, lower E_T threshold triggers as shown in Table A.1.

level	MET_PEM	PLUG_ELECTRON_20
L1	L1_EM8_MET15	L1_EM8
L2	L2_PEM20_L1_EM8_MET15	L2_PEM20_PS10
L3	L3_PEM20_MET15	L3_PEM20

Table A.1: List of trigger paths considered to measure the forward W trigger efficiency.

A.2.1 L1_MET15_L3_MET15

The efficiency of the combined L1_MET15_L3_MET15 trigger is measured using $W \rightarrow e\nu$ candidates selected using the requirements described in Section 3.5. From Table A.1 we find that the PLUG_ELECTRON_20 and MET_PEM triggers differ only in the requirement of $\not\!\!E_T$ at L1 and L3 (and a prescale factor). Therefore, to measure the efficiency of the L1_MET15_L3_MET15 trigger we check how often $W \rightarrow e\nu$ events passing the PLUG_ELECTRON_20 trigger also pass the MET_PEM:

$$\epsilon(\mathrm{L1\_MET15\_L3\_MET15}) = \frac{\mathrm{PLUG\_ELECTRON\_20\ \&\&\ MET\_PEM}}{\mathrm{PLUG\_ELECTRON\_20}} \qquad \text{(A.5)}$$

Figure A.2 shows the efficiency of the L1_MET15_L3_MET15 trigger as a function of raw $\not\!\!E_T$ (offline $\not\!\!E_T$ calculated at $z = 0$ and used in the trigger), offline $\not\!\!E_T$ (calculated at z of the highest sum p_T vertex and used in analysis) and η_{det} of the electron. We fit the turn-on curve vs. $\not\!\!E_T$ with Eqn. A.6

$$\epsilon(x) = \frac{1}{1 + e^{-\beta(x-\alpha)}}. \qquad \text{(A.6)}$$

A.2.2 L2_PEM20

The efficiency of the L2_PEM20 trigger was measured using the $Z \rightarrow e^+e^-$ (CP) sample because it provides a higher statistics sample of unbiased electrons. The $Z \rightarrow e^+e^-$ (CP) events are collected with the central electron trigger, ELECTRON_CENTRAL_18, which belongs to the HIGH_PT_ELECTRON_1 data stream. We require a CEM and a PEM electron where the selection criteria are shown in Table 3.1, 3.2. We have measured the L2 PEM20 trigger efficiency using "No Prescale Bit" for prescale trigger.

$$\epsilon(\mathrm{L2\_PEM20}) = \frac{\mathrm{Z \rightarrow e^+e^-(CP)\ \&\&\ L2\_PEM20\_NoPS}}{\mathrm{Z \rightarrow e^+e^-(CP)}}. \tag{A.7}$$

Since the L2_PEM20 trigger efficiency decreases as it goes to high $|\eta|$, we measure E_T turn-on curve in different η ranges. These are shown in Figure A.3.

A.2.3 L3_PEM20

The $Z \rightarrow e^+e^-$ (CP) events are also used to evaluate the L3_PEM20 trigger efficiency. We define it as:

$$\epsilon(\mathrm{L3\_PEM20}) = \frac{\mathrm{Z \rightarrow e^+e^-(CP)\ \&\&\ L2\_PEM20\_NoPS\ \&\&\ L3\_PEM20}}{\mathrm{Z \rightarrow e^+e^-(CP)\ \&\&\ L2\_PEM20\_NoPS}}. \tag{A.8}$$

This L3_PEM20 trigger requires that an event has EM transverse energy greater than 20GeV and Had/Em less than 0.125. We can get Level3 trigger variables by accessing the L3SummaryObject. Figure A.4 shows the turn-on curve vs. raw and offline E_T and η.

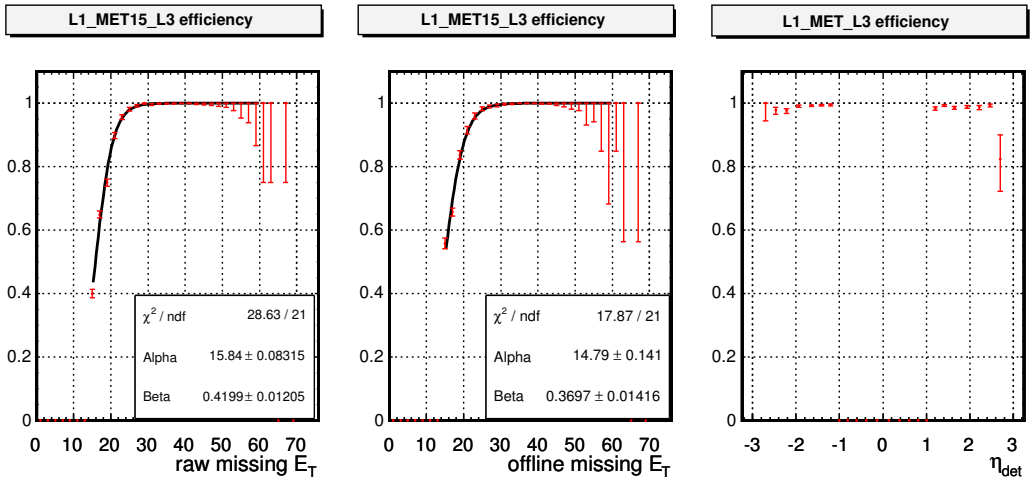

Figure A.2: Efficiency of the L1_MET15_L3_MET15 trigger as a function of raw or offline $\not\!\!E_T$ and η_{det} of the electron. The turn-on curve vs. $\not\!\!E_T$ is fitted with the function in equation A.6.

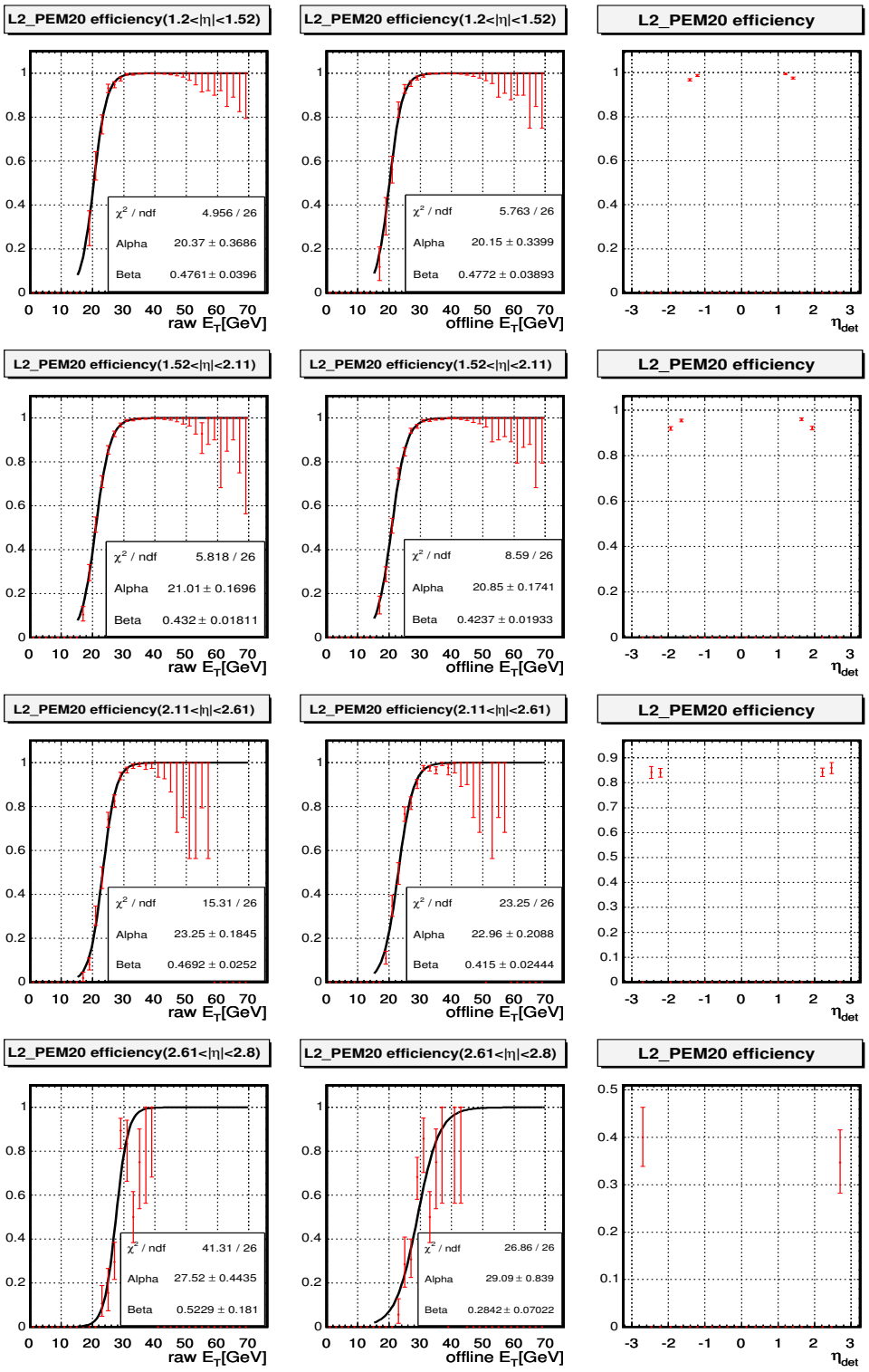

Figure A.3: The L2_PEM20 trigger efficiency as a function of raw and offline E_T and the η_{det} dependence.

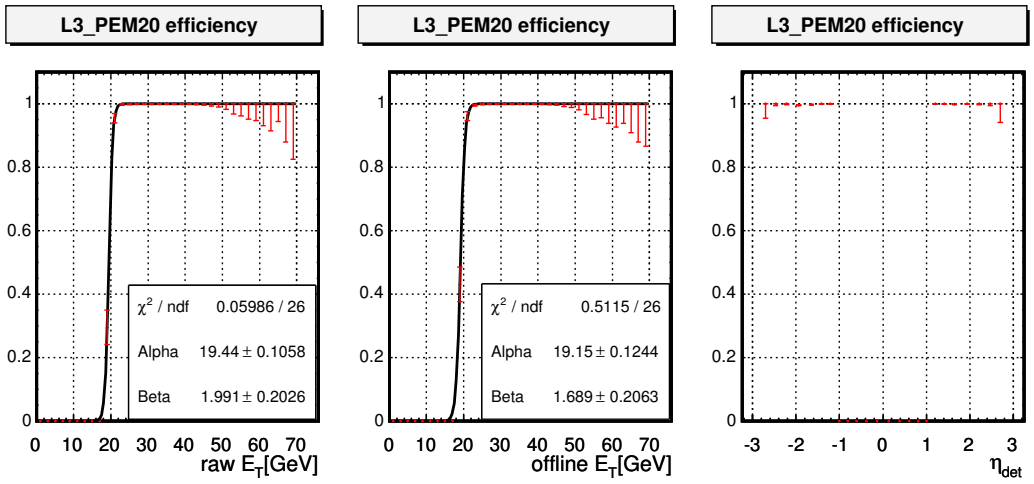

Figure A.4: Efficiency of the L3_PEM20 trigger as a function of raw and offline E_T and η_{det} of the electron,

Appendix B

Lepton charge asymmetry

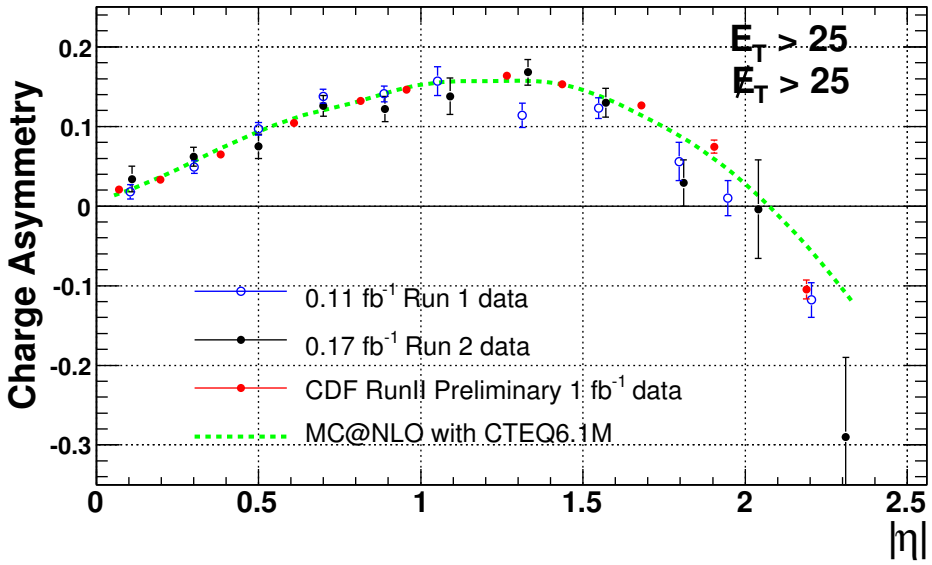

Figure B.1: The lepton charge asymmetry in the $W \rightarrow e\nu$ process with CDF Run II 1 fb^{-1} data including only statistical uncertainty. The measured lepton asymmetry is compared to the previous results, Run I (110 pb^{-1}) and Run II (170 pb^{-1}), and NLO prediction provided by CTEQ6.1M PDFs.

Appendix C

PDF effects on W charge asymmetry

yw	$x < 5.8 * 10^{-4}$	$x < 9.3 * 10^{-4}$	$x < 1.5 * 10^{-3}$	$x < 2.4 * 10^{-3}$	$x < 3.8 * 10^{-3}$	$x < 6.0 * 10^{-3}$	$x < 9.5 * 10^{3}$	$x < 1.5 * 10^{-2}$
-3 - -2.6	0.006	0.014	0.024	-0.03	-0.188	-0.21	-0.099	-0.097
-2.6 - -2.3	0	0.002	0.004	0.01	0.163	-0.202	-0.157	-0.12
-2.3 - -2.05	0	0	0.002	0.005	0.003	0	-0.201	-0.13
-2.05 - -1.8	0	0	0	0.002	0.024	-0.064	-0.191	-0.131
-1.8 - -1.6	0	0	0	0.002	0.03	-0.018	-0.173	-0.131
-1.6 - -1.4	0	0	0	0.001	0.031	0.028	-0.129	-0.193
-1.4 - -1.2	0	0	0	0.001	0.032	0.046	-0.031	-0.251
-1.2 - -1	0	0	0	0.001	0.031	0.057	0.027	-0.138
-1 - -0.8	0	0	0	0	0.027	0.06	0.059	-0.06
-0.8 - -0.6	0	0	0	0	0.02	0.058	0.072	-0.009
-0.6 - -0.4	0	0	0	0	0.008	0.051	0.072	-0.002
-0.4 - -0.2	0	0	0	0	0.001	0.036	0.052	0.001
-0.2 - 0	0	0	0	0	0	0.015	0.015	0.001
0 - 0.2	0	0	0	0	0	-0.014	-0.015	-0.003
0.2 - 0.4	0	0	0	0	-0.001	-0.037	-0.049	-0.004
0.4 - 0.6	0	0	0	0	-0.007	-0.052	-0.074	0
0.6 - 0.8	0	0	0	0	-0.02	-0.056	-0.075	0.006
0.8 - 1	0	0	0	0	-0.028	-0.061	-0.057	0.06
1 - 1.2	0	0	0	-0.001	-0.032	-0.057	-0.023	0.162
1.2 - 1.4	0	0	0	-0.001	-0.035	-0.043	0.041	0.241
1.4 - 1.6	0	0	0	-0.001	-0.034	-0.025	0.127	0.198
1.6 - 1.8	0	0	0	-0.001	-0.031	0.008	0.157	0.146
1.8 - 2.05	0	0	0	-0.003	-0.023	0.056	0.204	0.136
2.05 - 2.3	0	0	0	-0.007	0.008	-0.013	0.202	0.132
2.3 - 2.6	0	-0.002	-0.009	-0.008	-0.179	0.208	0.156	0.114
2.6 - 3	-0.004	-0.021	-0.022	0.057	0.221	0.24	0.136	0.108

yw	$x < 2.4 * 10^{-2}$	$x < 3.9 * 10^{-2}$	$x < 6.1 * 10^{-2}$	$x < 9.8 * 10^{-2}$	$x < 0.16$	$x < 0.25$	$x < 0.39$	$x < 0.63$	$x < 1.0$
-3 - -2.6	-0.03	0.007	0.01	-0.015	-0.084	-0.04	-0.027	-0.359	-0.079
-2.6 - -2.3	-0.074	-0.016	-0.004	-0.061	-0.085	-0.073	-0.203	0.035	0.007
-2.3 - -2.05	-0.088	-0.045	-0.033	-0.076	-0.086	-0.082	-0.209	0.03	0.008
-2.05 - -1.8	-0.105	-0.082	-0.082	-0.086	-0.086	-0.114	-0.243	0.037	0.005
-1.8 - -1.6	-0.102	-0.114	-0.116	-0.082	-0.045	-0.345	0.01	0.039	0.005
-1.6 - -1.4	-0.108	-0.145	-0.146	-0.085	-0.038	-0.387	0.055	0.045	0.005
-1.4 - -1.2	-0.129	-0.171	-0.163	-0.093	-0.319	-0.098	0.065	0.044	0.005
-1.2 - -1	-0.206	-0.184	-0.179	-0.093	-0.399	0.083	0.071	0.04	0.004
-1 - -0.8	-0.232	-0.186	-0.164	-0.2	-0.24	0.085	0.076	0.036	0.003
-0.8 - -0.6	-0.188	-0.215	-0.153	-0.43	0.034	0.087	0.07	0.028	0.001
-0.6 - -0.4	-0.117	-0.167	-0.147	-0.312	0.017	0.075	0.061	0.017	0
-0.4 - -0.2	-0.069	-0.053	-0.336	-0.011	0.011	0.046	0.048	0.006	0
-0.2 - 0	-0.025	0.066	-0.168	-0.002	0.002	0.015	0.019	0	0
0 - 0.2	0.02	-0.054	0.174	0.008	-0.005	-0.015	-0.021	0	0
0.2 - 0.4	0.058	0.052	0.336	0.01	-0.015	-0.047	-0.048	-0.006	0
0.4 - 0.6	0.118	0.183	0.153	0.32	-0.02	-0.076	-0.063	-0.016	0
0.6 - 0.8	0.173	0.215	0.154	0.417	-0.041	-0.092	-0.068	-0.03	-0.001
0.8 - 1	0.25	0.19	0.165	0.22	0.247	-0.083	-0.075	-0.036	-0.003
1 - 1.2	0.202	0.183	0.169	0.091	0.422	-0.073	-0.072	-0.041	-0.004
1.2 - 1.4	0.127	0.166	0.164	0.09	0.302	0.116	-0.065	-0.044	-0.005
1.4 - 1.6	0.106	0.146	0.147	0.088	0.038	0.393	-0.057	-0.046	-0.006
1.6 - 1.8	0.098	0.113	0.114	0.079	0.047	0.336	-0.006	-0.041	-0.006
1.8 - 2.05	0.104	0.081	0.079	0.086	0.082	0.12	0.254	-0.037	-0.007
2.05 - 2.3	0.091	0.047	0.033	0.077	0.087	0.078	0.193	-0.009	-0.005
2.3 - 2.6	0.077	0.016	0.004	0.06	0.081	0.079	0.199	-0.049	-0.008
2.6 - 3	0.034	-0.003	-0.006	0.016	0.094	0.048	0.061	0.384	0.137

Table C.1: The effects on W asymmetry are estimated when input PDFs for the valence quark change.

yw	$x < 5.8 * 10^{-4}$	$x < 9.3 * 10^{-4}$	$x < 1.5 * 10^{-3}$	$x < 2.4 * 10^{-3}$	$x < 3.8 * 10^{-3}$	$x < 6.0 * 10^{-3}$	$x < 9.5 * 10^{-3}$	$x < 1.5 * 10^{-2}$
-3 - -2.6	0	0.006	0.002	0.01	0.023	0.018	0.14	0.217
-2.6 - -2.3	0	0	0.002	0.004	0.049	0.014	0.061	0.137
-2.3 - -2.05	0	0	0.001	0.002	-0.002	0.081	0.03	0.098
-2.05 - -1.8	0	0	0	0.001	-0.004	0.027	0.052	0.067
-1.8 - -1.6	0	0	0	0	-0.006	-0.023	0.067	0.054
-1.6 - -1.4	0	0	0	0	-0.002	-0.02	0.021	0.053
-1.4 - -1.2	0	0	0	0	-0.003	-0.018	-0.035	0.085
-1.2 - -1	0	0	0	0	-0.002	-0.019	-0.035	0.023
-1 - -0.8	0	0	0	0	-0.002	-0.016	-0.035	-0.026
-0.8 - -0.6	0	0	0	0	-0.001	-0.014	-0.033	-0.015
-0.6 - -0.4	0	0	0	0	0	-0.012	-0.031	-0.013
-0.4 - -0.2	0	0	0	0	0	-0.008	-0.025	-0.006
-0.2 - 0	0	0	0	0	0	-0.004	-0.007	0
0 - 0.2	0	0	0	0	0	0.003	0.004	0.01
0.2 - 0.4	0	0	0	0	0	0.009	0.019	0.011
0.4 - 0.6	0	0	0	0	0	0.013	0.031	0.013
0.6 - 0.8	0	0	0	0	0.001	0.015	0.033	0.023
0.8 - 1	0	0	0	0	0.002	0.016	0.032	0.022
1 - 1.2	0	0	0	0	0.001	0.016	0.025	-0.039
1.2 - 1.4	0	0	0	0	0.003	0.016	0.029	-0.065
1.4 - 1.6	0	0	0	0	0.003	0.019	-0.015	-0.058
1.6 - 1.8	0	0	0	-0.001	0.004	0.025	-0.061	-0.049
1.8 - 2.05	0	0	0	0	0.003	-0.028	-0.047	-0.067
2.05 - 2.3	0	0	0	-0.001	-0.001	-0.071	-0.031	-0.095
2.3 - 2.6	0	0	0	-0.005	-0.039	-0.01	-0.059	-0.132
2.6 - 3	-0.004	0	-0.01	-0.016	-0.009	-0.007	-0.136	-0.222

yw	$x < 2.4 * 10^{-2}$	$x < 3.9 * 10^{-2}$	$x < 6.1 * 10^{-2}$	$x < 9.8 * 10^{-2}$	$x < 0.16$	$x < 0.25$	$x < 0.39$	$x < 0.63$	$x < 1.0$	
-3 - -2.6	0.091	0.009	0.003	0.052	0.212	0.176	0.048	0.012	0.01	
-2.6 - -2.3	0.122	0.032	0.011	0.107	0.15	0.083	0.011	0.06	0	
-2.3 - -2.05	0.113	0.068	0.051	0.113	0.111	0.053	0.079	-0.004	0	
-2.05 - -1.8	0.103	0.102	0.108	0.108	0.082	0.025	0.069	-0.009	0	
-1.8 - -1.6	0.092	0.137	0.149	0.101	0.064	0.086	-0.03	-0.009	0	
-1.6 - -1.4	0.085	0.16	0.172	0.104	0.05	0.05	-0.028	-0.006	0	
-1.4 - -1.2	0.091	0.176	0.181	0.11	0.091	-0.011	-0.024	-0.006	0	
-1.2 - -1	0.106	0.177	0.191	0.118	0.063	-0.04	-0.025	-0.003	0	
-1 - -0.8	0.14	0.162	0.17	0.141	0.024	-0.039	-0.021	-0.004	0	
-0.8 - -0.6	0.107	0.159	0.158	0.161	-0.013	-0.038	-0.018	-0.002	0	
-0.6 - -0.4	0.038	0.157	0.144	0.093	-0.007	-0.034	-0.017	-0.001	0	
-0.4 - -0.2	0.022	0.087	0.142	0.018	-0.005	-0.022	-0.012	0	0	
-0.2 - 0	0.008	0.001	0.051	0.007	0.001	-0.006	-0.006	0	0	
0 - 0.2	-0.006	-0.008	-0.048	-0.011	0.011	0.003	0.006	0	0	
0.2 - 0.4	-0.021	-0.08	-0.131	-0.02	0.007	0.017	0.013	0	0	
0.4 - 0.6	-0.037	-0.161	-0.15	-0.095	0.009	0.031	0.018	0	0	
0.6 - 0.8	-0.09	-0.159	-0.156	-0.139	0.018	0.038	0.018	0.003	0	
0.8 - 1	-0.15	-0.167	-0.177	-0.146	-0.034	0.036	0.022	0.002	0	
1 - 1.2	-0.104	-0.175	-0.181	-0.118	-0.082	0.033	0.022	0.003	0	
1.2 - 1.4	-0.091	-0.174	-0.189	-0.115	-0.08	0.018	0.022	0.005	0	
1.4 - 1.6	-0.084	-0.159	-0.17	-0.104	-0.047	-0.053	0.026	0.006	0	
1.6 - 1.8	-0.091	-0.137	-0.15	-0.103	-0.061	-0.082	0.034	0.007	0	
1.8 - 2.05	-0.104	-0.099	-0.105	-0.108	-0.082	-0.03	-0.063	0.01	0	
2.05 - 2.3	-0.114	-0.072	-0.052	-0.115	-0.11	-0.05	-0.071	0	0	
2.3 - 2.6	-0.123	-0.033	-0.011	-0.108	-0.141	-0.082	-0.011	-0.048	0	
2.6 - 3	-0.096	-0.009	-0.005	-0.053	-0.222	-0.172	-0.056	0.008	-0.013	

Table C.2: The effects on W asymmetry are estimated when input PDFs for the sea quark change.

yw	$x < 5.8 * 10^{-4}$	$x < 9.3 * 10^{-4}$	$x < 1.5 * 10^{-3}$	$x < 2.4 * 10^{-3}$	$x < 3.8 * 10^{-3}$	$x < 6.0 * 10^{-3}$	$x < 9.5 * 10^{3}$	$x < 1.5 * 10^{-2}$
-3 - -2.6	0	0.013	0.001	0.001	-0.02	0.028	0.047	0.046
-2.6 - -2.3	0	0.001	0.003	0	-0.006	-0.01	0.008	0.025
-2.3 - -2.05	0	0	0	0	-0.003	0.005	-0.004	0.012
-2.05 - -1.8	0	0	0	0.001	0	-0.01	-0.014	-0.005
-1.8 - -1.6	0	0	0	0	0	-0.003	-0.004	0
-1.6 - -1.4	0	0	0	0	0	-0.001	-0.004	-0.016
-1.4 - -1.2	0	0	0	0	0	0	-0.001	-0.017
-1.2 - -1	0	0	0	0	0	0.001	0	-0.005
-1 - -0.8	0	0	0	0	0	0	0.002	-0.002
-0.8 - -0.6	0	0	0	0	0	0.001	0.001	0
-0.6 - -0.4	0	0	0	0	0	0.001	0	0
-0.4 - -0.2	0	0	0	0	0	0	0	0
-0.2 - 0	0	0	0	0	0	0	0	0
0 - 0.2	0	0	0	0	0	0	-0.001	-0.002
0.2 - 0.4	0	0	0	0	0	-0.001	-0.001	-0.002
0.4 - 0.6	0	0	0	0	0	-0.002	-0.002	0
0.6 - 0.8	0	0	0	0	0	-0.001	0	0.001
0.8 - 1	0	0	0	0	0	0	-0.001	0.007
1 - 1.2	0	0	0	0	0	-0.002	0.002	0.013
1.2 - 1.4	0	0	0	0	0	-0.002	0.004	0.014
1.4 - 1.6	0	0	0	0	-0.001	-0.001	0.009	0.012
1.6 - 1.8	0	0	0	0	-0.001	0	0.025	0.03
1.8 - 2.05	0	0	0	0	-0.001	0.006	0.027	0
2.05 - 2.3	0	0	-0.001	0	-0.002	0.011	0.022	0.006
2.3 - 2.6	0	-0.001	-0.001	-0.003	0.003	0.051	0.028	-0.009
2.6 - 3	0	-0.001	-0.014	0.015	0.002	-0.052	-0.03	-0.081

yw	$x < 2.4 * 10^{-2}$	$x < 3.9 * 10^{-2}$	$x < 6.1 * 10^{-2}$	$x < 9.8 * 10^{-2}$	$x < 0.16$	$x < 0.25$	$x < 0.39$	$x < 0.63$	$x < 1.0$
-3 - -2.6	0.038	0.024	0.005	0.002	0	0.003	0.003	0	-0.003
-2.6 - -2.3	0.02	0.015	0.005	0.006	0.005	0.001	0.002	-0.005	0
-2.3 - -2.05	0.008	0.008	0.004	0.01	0.006	0.003	0	-0.004	-0.001
-2.05 - -1.8	-0.002	0.01	0.006	0.004	0.005	0.003	0.001	0.003	0
-1.8 - -1.6	0.003	0.006	0.006	0.007	0.004	0.007	0.001	0	0
-1.6 - -1.4	-0.005	0.001	0.011	0.009	0.002	0.005	0.006	0	0
-1.4 - -1.2	-0.008	0.002	0.012	0.006	0.005	0.008	0	0	0
-1.2 - -1	-0.016	0.005	0.009	0.01	0.009	0.004	0	0	0
-1 - -0.8	-0.017	-0.012	0.003	0	0.009	0.004	0.001	0	0
-0.8 - -0.6	-0.008	-0.003	-0.002	0.01	0.01	0.004	-0.001	0	0
-0.6 - -0.4	-0.001	-0.009	-0.002	0.008	0.004	-0.006	-0.002	0	0
-0.4 - -0.2	-0.004	-0.013	-0.007	0.01	0.002	0.002	0	0	0
-0.2 - 0	-0.002	0	0.003	0	0.002	-0.003	-0.002	0	0
0 - 0.2	0.003	0.003	0.002	-0.013	-0.007	-0.002	0	0	0
0.2 - 0.4	-0.001	0.006	0.012	0	-0.006	0	0	0	0
0.4 - 0.6	0.004	0.01	-0.005	-0.001	-0.008	-0.003	0.003	0.001	0
0.6 - 0.8	0.011	0.014	-0.003	-0.011	-0.007	0	0	0	0
0.8 - 1	0.019	0.002	-0.011	-0.012	-0.008	0	-0.002	0	0
1 - 1.2	0.021	-0.007	-0.014	-0.007	-0.005	-0.008	0	0	0
1.2 - 1.4	0.006	-0.001	-0.001	-0.011	-0.005	-0.002	0	0	0
1.4 - 1.6	0.002	-0.006	-0.003	-0.004	0	0.003	-0.003	0	0
1.6 - 1.8	0	0	-0.01	-0.005	-0.002	0	0.001	0.001	0
1.8 - 2.05	0	-0.002	-0.002	-0.007	0	0	0	-0.002	0
2.05 - 2.3	-0.011	-0.015	-0.005	-0.007	-0.004	-0.002	-0.003	0	0
2.3 - 2.6	-0.01	-0.012	-0.008	-0.004	-0.003	-0.001	0	0.006	0
2.6 - 3	-0.048	-0.04	-0.001	-0.005	-0.007	0	-0.003	0	0.004

Table C.3: The effects on W asymmetry are estimated when input PDFs for the gluon change.

Bibliography

[1] Murray Gell-Mann and Yuval Ne'eman, "The Eightfold Way", 1964 by Perseus Publishing.

[2] Panofsky, W.K.H. "Low q-squared electrodynamics, eleastic and inelastic electron (and muon) scattering." Fourteenth International Conference on High-Energy Physics, Proceedings. (Geneva: European Organization for Nuclear Research, 1968.), SLAC-PUB-0406, April 1968.

[3] D.P. Barber *et al.*, *Discovery of Three-Jet Events and a Test of Quantum Chromodynamics at PETRA Phys. Rev. Lett.* **43** (830) 1979.

[4] J. Pumplin, D.R. Stump, J. Huston, H.L. Lai, P. Nadolsky and W.K. Tung, J. High Energy Phys. **0207**, 012 (2002).

[5] A.D. Martin, W.J. Stirling, R.S. Thorne and G. Watt, University of Durham preprint IPPP/07/46 (2007), [arXiv:0706.0459].

[6] A.D. Martin, W.J. Stirling, and R.G. Roberts, *Parton distribution of the proton Phys. Rev.* **D 50** (1994) 6734.

[7] F. Abe *et al.*, [CDF Collaboration], *Measurement of the Lepton Charge Asymmetry in W-Boson Decays Production in $p\bar{p}$ Collisions Phys. Rev. Lett.* **81** (5754) 1998.

[8] D. Acosta *et al.*, [CDF Collaboration], *Measurement of the forward-backward charge asymmetry from $W \rightarrow e\nu$ production in $p\bar{p}$ collisions at $\sqrt{s}$ = 1.96* TeV *Phys. Rev.* **D 71** (051104) 2005.

[9] V. M. Abazov *et al.* [D0 Collaboration], *Measurement of the muon charge asymmetry from W boson decays* arXiv:0709.4254 [hep-ex].

[10] L.W. Whitlow *et al.*, *Phys. Rev.* **B 282** (1992) 475.

[11] J. Gomez *et al.*, *Phys. Rev.* **D 49** (1994) 4348.

[12] J.J. Aubert *et al.*, *Nucl. Phys.* **B 293** (1987) 740.

[13] L.P. Kaptari and A.Yu. Umnikov, *Phys. Rev.* **B 259** (1991) 151.

[14] W. Melnitchouk, A.W. Schreiber and A.W Tomas, *Phys. Rev.* **D 49** (1994) 1183; *Phys. Rev.* **B 335** (1994) 11.

[15] Accelerator Concepts Rookie Books, (2003). http://www-bdnew.fnal.gov/operations/rookie_books/rbooks.html.

[16] D. Acosta *et al.*, Nucl. Instrum. Methods, *A494*, 57 (2002)

[17] W. Ashmanskas, *et al.*, Nucl. Instrum. Methods, *A518*, 532 (2004).

[18] T. Affolder *et al.*, Nucl. Instrum. Methods, *A526*, 249 (2004).

[19] J. D. Jackson, "Classical Electrodynamics", John Wiley & Sons, 1999, pg 715.

[20] T. Sjostrand, P. Eden, C. Friberg, L. Lonnblad, G. Miu, S. Mrenna and E. Norbin, Comput. Phys. Commum. **135**, 238 (2001) [zrXiv:hep-ph/0010017].

[21] H.L. Lai *et al.*[CTEQ Collaboration], Eur. Phys. J. C**12**, 375 (2000) [arXiv:hep-ph/9903282].

[22] C. Anastasiou *et al.*, Phys. Rev. **D69**, 094008 (2004)

[23] T. Affolder *et al.*[CDF Collaboration], Phys. Rev. Lett. **84**, 845 (2000) [arXiv:hep-ex/0001021].

[24] Chris Hays, Peter Tamburello, Ashutosh Kotwal, Peter Wittich, and Rick Snider, "The COT Pattern Recognition Algorithm and Offline Code", CDF internal note, 6992, 2004.

[25] J. Thom, D. Glenzinski, M. Herndon, C.-J. Lin, A. Yagil, "Determination of the Run II COT Tracking Efficiency using the W-No-Track Sample", CDF internal note, 6866, 2004.

[26] B. R. Ko, S. H. Oh, C. Wang, "SVX II Stand-alone Tracking", CDF internal note, 6440, 2003.

[27] R. G. Wagner, "Electron Identification for Run II: Understanding and Using Lshr", CDF internal note, 6249, 2004.

[28] A. Bhatti *et al.*"Jet Energy Corrections for Run II", CDF internal note, 6565, 2003.

[29] J. Lee, G. De Lentdecker, K. McFarland, "An Estimation of Jet Background in the Dielectron Events", CDF internal note, 7997, 2006

[30] T. Aaltonen *et al.* [CDF Collaboration], Phys. Rev. Lett. **99**, 151801 (2007).

[31] G. Abbiendi *et al.* [OPAL Collaboration], Eur. Phys. J. C **45**, 307 (2006).

[32] P. Achard *et al.* [L3 Collaboration], Eur. Phys. J. C **45**, 569 (2006).

[33] S. Schael *et al.* [ALEPH Collaboration], Eur. Phys. J. C **47** (2006) 309.

[34] P. Abreu *et al.* [DELPHI Collaboration], Phys. Lett. B **511**, 159 (2001).

[35] V. M. Abazov *et al.* [D0 Collaboration], Phys. Rev. D **66**, 012001 (2002).

[36] A. A. Affolder *et al.* [CDF Collaboration],

[37] W.-M. Yao *et al.*, Journal of Physics G **33**, 1 (2006).

[38] S. Frixione and B.R. Webber, *Matching NLO QCD computations and parton shower simulations, J. High Energy Phys.* **0206** (2002) 029. [hep-ph/0204244].

[39] T. Spreitzer, C. Mills, J. Incandela, "Electron Identification in Offline Release 6.1.2", CDF internal note, 7950, 2005.

[40] L. Lyons, D. Gibaut, and P. Clifford, Nucl. Instrum. Methods Phys. Res. A **270**, 110 (1988).

[41] J. Nielsen, L. Tompkins, D. Hoffman, Y.K. Kim, G. Veramendi, "Trigger Efficiencies for High E_T Electrons", CDF internal note, 6234, 2004